

The Pennsylvania State University
The Graduate School
Department of Materials Science and Engineering

**EFFECTS OF NANOSCALE COATINGS
ON RELIABILITY OF MEMS OHMIC CONTACT SWITCHES**

A Dissertation in
Materials Science and Engineering

by

Amber Leigh Tremper

© 2013 Amber Leigh Tremper

Submitted in Partial Fulfillment
of the Requirements
for the Degree of

Doctor of Philosophy

May 2013

The dissertation of Amber Leigh Tremper was reviewed and approved* by the following:

Suzanne E. Mohny
Professor of Materials Science and Engineering and Electrical Engineering
Dissertation Advisor
Chair of Committee

Christopher L. Muhlstein
Associate Professor of Materials Science and Engineering, Georgia Tech
Dissertation Advisor

Paul Howell
Professor Emeritus of Metallurgy, Department of Materials Science and
Engineering

Seong Kim
Associate Professor of Chemical Engineering and Materials Science and
Engineering

Albert E. Segall
Professor of Engineering Science and Mechanics

Joan M. Redwing
Professor of Materials Science and Engineering, Chemical Engineering &
Electrical Engineering
Chair of the Intercollege Graduate Degree Program in Materials Science
and Engineering

*Signatures are on file in the Graduate School

ABSTRACT

This thesis examines how the electrical and mechanical behavior of Au thin films is altered by the presence of ultra-thin metallic coatings. To examine the mechanical behavior, nanoindentation, nano-scratch, and atomic force microscopy (AFM) testing was performed. The electrical behavior was evaluated through Kelvin probe contact resistance measurements.

This thesis shows that ultra-thin, hard, ductile coatings on a softer, ductile underlying layer (such as Ru or Pt on Au) had a significant effect on mechanical behavior of the system, and can be tailored to control the deformation resistance of the thin film system. Despite Ru and Pt having a higher hardness and plane strain modulus than Au, the Ru and Pt coatings decreased both the hardness and plane strain modulus of the layered system when the indentation depth was on the order of the coating thickness. Alternately, when the indentation depth was several times the coating thickness, the ductile, plastically hard, elastically stiff layer significantly hardened the contact response. These results correlate well with membrane stress theoretical predictions, and demonstrate that membrane theory can be applied even when the ratio of indentation depth, h , to coating thickness, t , is very large ($h/t < 10$). The transition from film-substrate models to membrane models occurs when the indent penetration depth to coating thickness ratio is less than ~ 0.5 .

When the electrical behavior of the Ru-coated Au films was examined, it was found that all the measured resistances of the Au-only film and Ru-coated systems were several orders of magnitude larger than those predicted by Holm's law, but were still in good

agreement with previously reported values in the literature. Previous studies attributed the high contact resistances to a variety of causes, including the buildup of an insulating contamination layer. This thesis determined the cause of the deviations to be large sheet resistance contributions to the total measured resistance. Further, studies on aged samples (with thicker contamination layers) conclusively showed that, while contamination increases the contact resistance, it also increases the dependence on force. This thesis also details that the relative contribution of contact resistance to the total measured resistance can be maximized by decreasing the probe spacing and tip radius.

AFM testing of the layered systems showed that the coated samples had larger predicted plane strain moduli than the Au sample, in contrast to the nanoindentation testing. Thus, when the contact depth was kept sufficiently small, the contact stiffness increased as predicted by substrate models. When the contact depth was on the order of the coating thickness, the contact stiffness actually decreased. Additionally, the force-separation plots showed that the Ru and Pt surfaces either accumulated large amounts of contamination or were less susceptible to being wiped clean than the Au film. Further, scratch testing of the Au film and Ru and Pt coatings show that the hard surface coatings reduce material removal and contact wear.

Ultra-thin Ru and Pt surface coatings on Au films are shown to be improved material systems for ohmic contact switches. The wear is reduced for coated materials, while the resistance and power consumption through the coating are not significantly affected.

TABLE OF CONTENTS

LIST OF FIGURES	vii
LIST OF TABLES	x
ACKNOWLEDGEMENTS	xi
Chapter 1 Introduction	1
1.1. Motivation	1
1.1.1. Background	2
1.1.2. Materials	4
1.1.3. Testing Methodologies	7
1.2. Indentation Theory	8
1.2.1. General Theory – Oliver-Pharr Approach	9
1.2.2. Residual Stress Effects	12
1.2.3. Surface Roughness Effects	16
1.2.4. Thin Film Effects	20
1.2.4.1. Substrate Model	20
1.2.4.2. Membrane Model	25
1.2.5. Adhesion Effects	28
1.3. Contact Resistance Theory	30
1.3.1. Ballistic Transport	30
1.3.2. Geometric Effects	31
1.3.3. Thermal Effects	34
1.4. Investigation of Ultra-thin Coatings for Ohmic Contact Switches	35
Chapter 2 Methods	37
2.1. Fabrication and Characterization of Thin Films	39
2.2. Nanoindentation Testing	47
2.2.1. Experimental Methods	48
2.2.2. Analytical Methods	50
2.2.2.1. Area function correction	53
2.2.2.2. Compliance correction	54
2.2.2.3. Pile-up correction	56
2.3. Electrical Contact Resistance Measurements	57
2.3.1. Experimental Methods	58
2.3.2. Analytical Methods	62
2.4. Adhesion and Scratch Testing	64
Chapter 3 Softening under Membrane Contact Stress due to Ultra-thin Ru Coatings on Au films	67

3.1. Introduction	67
3.2. Experimental Methods.....	69
3.3. Results and Discussion	76
3.3.1. Au Film Behavior	76
3.3.2. Coating Thickness Effects on Deformation	78
3.3.3. Tailoring of Mechanical Response through Residual Stress	87
3.3.4. Corroboration of Results from Pt Coatings	91
3.4. Conclusions	94
Chapter 4 Reconciling Deformation, Contamination, and Geometry Contributions to the Resistance of Ohmic Contact Switches	96
4.1. Introduction	96
4.2. Methods	98
4.3. Results	101
4.4. Conclusions	109
Chapter 5 Impact of Ultra-thin Coatings on Stiction and Friction.....	111
5.1. Methods	113
5.2. Results	115
5.2.1. Stiction Behavior	115
5.2.2. Wear Behavior	122
5.3. Conclusions	124
Chapter 6 Conclusions	125
6.1. Summary of Findings	125
6.2. Future Work.....	129
References	131

LIST OF FIGURES

Figure 1.1: Schematic of surface roughness effects during nanoindentation testing.....	18
Figure 1.2: Randomly place four probe configuration.....	32
Figure 2.1: Phase diagram for a) Au-Ru binary systems (reprinted from [54]) and b) Au-Pt binary systems (reprinted from [54])......	38
Figure 2.2: Schematic of a) Au film, b) Ru coated films, and c) Pt coated films. Schematics are not to scale.	39
Figure 2.3: TEM image of Au film grain structure showing small (5-30 nm) grains.....	41
Figure 2.4: TEM image of Ru coated Au film cross-section.....	42
Figure 2.5: TEM image of a) Ru film grain structure and b) Pt film grain structure. Both had ultra-fine grain sizes between 5-30 nm.	45
Figure 2.6: SAD image of a) 5 nm Ru coating and b) 10 nm Pt coating on amorphous silicon nitride TEM windows.....	46
Figure 2.7: AES scan of 5 nm Ru coating for a) full spectrum and b) detailed scan of expected Au and Ru peaks, with expected peaks shown as black vertical lines.....	47
Figure 2.8: Load control command waveforms for the 75, 300, and 600 μN maximum force indents.	49
Figure 2.9: Schematic of parsing algorithm, where minima is found first, and then maxima (shown as black stars in image) are found along 8 directions.	57
Figure 2.10: Image of testing apparatus.....	58
Figure 2.11: Current command from -1 to 1 mA with 100 μA delta.....	61
Figure 2.12: Schematic of electrical contact resistance measurement technique, showing how the electrical behavior was monitored throughout an indentation test.....	62

Figure 3.1: AFM image of a.) Au-only film showing ~100 nm features on surface and b.) Au film with 5 nm Ru coating with slightly larger surface roughness.....	70
Figure 3.2: TEM image of 100 nm Au deposited on rocksalt showing small (5-30 nm) grains. Inset shows the associated selected area diffraction of the Au film.....	72
Figure 3.3: Selected area diffraction patterns of a.) 5 nm Ru coating and b.) 10 nm Pt coating on 20 nm thick amorphous Si ₃ N ₄ windows. The Ru and Pt coatings, although thin, have crystalline diffraction patterns corresponding to HCP and FCC structures, respectively. The broad rings in the 5 nm Ru coating are likely due to very fine grain structure.	73
Figure 3.4: TEM image of Ru coated Au film cross-section.	74
Figure 3.5: Plane strain elastic modulus vs. pile-up corrected contact depth. Data shown is for a 2mTorr, 350 nm thick Au-only film and 5, 10, and 20 nm thick Ru coatings sputtered at 2 mTorr on a 350 nm thick Au film sputtered at 2 mTorr. Lines are only shown to highlight trends and are not intended for interpolation.	78
Figure 3.6: Hardness vs. pile-up corrected contact depth. Data shown is for a 2mTorr, 350 nm thick Au-only film and 5, 10, and 20 nm thick Ru coatings sputtered at 2 mTorr on a 350 nm thick Au film sputtered at 2 mTorr. Lines are only shown to highlight trends and are not intended for interpolation.	80
Figure 3.7: Pile-up height vs. pile-up corrected contact depth. Data shown is for a 2mTorr, 350 nm thick Au-only film and 5, 10, and 20 nm thick Ru coatings sputtered at 2 mTorr on a 350 nm thick Au film sputtered at 2 mTorr. Lines are only shown to highlight trends and are not intended for interpolation.	83
Figure 3.8: Hardness vs. pile-up corrected contact depth. Data is for 10 nm thick Ru coatings sputtered at 2 and 5 mTorr on a 350 nm thick Au film sputtered 2 mTorr. Lines are only shown to highlight trends and are not intended for interpolation.	89
Figure 3.9: Plane strain elastic modulus vs. pile-up corrected contact depth. Data is for 10 nm thick Ru coatings sputtered at 2 and 5 mTorr on a 350 nm thick Au film sputtered 2 mTorr. Lines are only shown to highlight trends and are not intended for interpolation.	91
Figure 3.10: Plane strain modulus vs. pile-up corrected contact depth for 10, 50, and 100 nm thick Ru and Pt coatings deposited at 2 mTorr on a 350 nm thick Au film sputtered at 2 mTorr.	93

Figure 3.11: Hardness vs. pile-up corrected contact depth for 10, 50, and 100 nm thick Ru and Pt coatings deposited at 2 mTorr on a 350 nm thick Au film sputtered at 2 mTorr.....	93
Figure 4.1: Schematic of experimental test setup.	100
Figure 4.2: Measured and modeled resistances versus force.	102
Figure 4.3: Total resistance and constriction resistance versus force when probes are placed 55 μm away from the center of the contact (2 μm away from the edge of the contact at 0.5 N).	108
Figure 4.4: Relative contributions to the total contact resistance as a function of force for a modeled nano-scale contact (such as a conductive AFM tip). Points are added help identify the lines, and do not represent experimental points.....	109
Figure 5.1: Adhesive force obtained through scanning mode for a) Au-only film, b) Ru coating, and c) Pt coating. The colorbar for the Au-only sample is different to better show the contrast in the original image.	117
Figure 5.2: Representative force-displacement plot for a Pt/Ir AFM tip in contact with Au-only film.	118
Figure 5.3: Scratch test in-situ scans of a) Au-only films, b) 10 nm Ru coating, and c) 10 nm Pt coating. Average cross-section profiles of each material system are shown in d).	123

LIST OF TABLES

Table 2.1: Film deposition summary.....	44
Table 5.1: Scratch characteristics.....	123

ACKNOWLEDGEMENTS

Research does not occur in a vacuum; instead we stand on the shoulders of giants. It is important to recognize those who have contributed to this work. I would like to thank my advisors, Dr. Christopher Muhlstein and Dr. Suzanne Mohny. Your insight and guidance have been invaluable to the success of this work. I would also like to thank members of the Muhlstein and Mohny research groups, in particular, James Collins for help with LabView programming, and Kalissa Andre and Joyce Lin for TEM characterization. I would like to extend my thanks to the staff of the Penn State Materials Characterization Lab. Dr. Dave Shelleman provided help with the Instron, and Eric Sagmuller provided electronic components and training on machining equipment necessary to fabricate the custom contact resistance setup. Tim Tighe provided valuable training and insight on the AFM, even coming in on evenings and weekends to ensure my thesis could avoid work stoppages. Both Melisa Yashinski and Andrea Muller were valuable sounding boards about research techniques and analytical methods.

I would be remiss if I didn't mention the people who provided emotional support during this doctoral work. To my family, and in particular, my parents Dean and Denise Romasco, thank you for being a listening ear, a supporting shoulder, and a friendly voice. Your encouragement and support gave me the confidence to pursue this goal and the strength to persevere to the end. To my husband, Tom Tremper, words cannot express

what your love and support has meant to me. If a thesis is a labor of love, then this work is as much yours as it is mine.

Chapter 1

Introduction

Radio frequency (RF) microelectromechanical system (MEMS) ohmic contact switches have gained popularity for some applications that previously used p-i-n or field-effect transistor (FET) diode switches¹. Specifically, ohmic contact switches are being looked at for radar, satellite communication, and wireless communication systems [1]. However, the current material systems do not meet desired life limits for the device. Failure is often tied to the Au contact electrodes that fail through stiction (where the switch fails closed due to insufficient restoring force), microwelding, cold welding, and increased resistance. This thesis will evaluate alternate materials using a layered Au/Ru and Au/Pt system. Additionally, this thesis will examine how contact resistances are measured, and explain the high measured resistances in the literature. Finally, it will examine the surface stability in an adhesive study.

1.1. Motivation

RF MEMS ohmic contact switches provide significant improvements over their p-i-n counterparts, such as smaller insertion losses, lower power consumption, and higher isolation than p-i-n FET devices [1, 2]. However, ohmic contact switches have certain

¹ A p-i-n diode switch is a doped semiconductor switch. It consists of a p- and n-doped region surrounding an intrinsic semiconductor. When a forward bias is applied, electrons flow from the p-region to the n-region, passing an electrical signal.

limitations like slower switching speed than p-i-n FET switches, the need for hermetic packaging, and low power handling. Enhanced reliability of the devices is also desired. The best reported lifetimes of ohmic contact switches are 10^6 - 10^{11} cycles [1-4]. Details of how these cycles were obtained are not always readily available, and there was not always a clear indication of imminent device failure [3, 4]. Nevertheless, there are potential material science solutions to some of the problems facing ohmic contact switches. Concerns about hermetic packaging and limited power handling might be addressed and reliability improved by altering the material system used in ohmic contact switches.

1.1.1. Background

Ohmic contact switches typically operate by electrostatically or piezoelectrically actuating a flexure beam with a metallic patch towards another metallic patch on the substrate. When the two metallic patches (typically $100 - 10,000 \mu\text{m}^2$) make contact, the circuit is closed. The closed position switches the device on, allowing radio frequency (RF) signals to be transferred across it. The actuation forces are very small, less than 1 mN [1, 3-5]. These small forces typically are insufficient to dislodge any insulating oxides (as form on Al and Cu), and thus require noble metals for acceptable contact resistances. Additionally, low insertion losses are desired for ohmic contact switches. One source of insertion losses is the contact resistance between the two contact patches. A material's contact resistance is directly related to its hardness, as seen in Equation (1.1) below:

$$\begin{aligned}
 R_c &= R_{\text{constriction}} + R_{\text{contamination}} = \frac{\rho}{2a} + \frac{\rho_{\text{c,contamination}}}{\pi a^2} \\
 &= \rho \sqrt{\frac{\pi \xi H}{4P}} + \frac{\rho_{\text{c,contamination}}}{\pi a^2}
 \end{aligned} \tag{1.1}$$

where R_c is the contact resistance, $R_{\text{constriction}}$ is the constriction resistance, $R_{\text{contamination}}$ is the resistance contribution from a film contamination, ρ is the resistivity of the contact material, a is the contact radius, $\rho_{\text{c,contamination}}$ is the specific contact resistance of the contamination film, H is the hardness, P is the applied contact force, and ξ is a constant based on the degree of elasticity in the contact. Bulk Au has both low ρ and H and can have low R_{film} due to lack of oxidation, leading to low R_c and low insertion losses. Because Au should have low contact resistances and does not form an oxide, it has become the most frequently used contact material in ohmic contact switches.

Despite its advantages, Au also has several limitations. While the softness of Au is an advantage in the contact resistance, it causes wear problems. Softer metals are more susceptible to adherence, where metallic bonds form cold welds between the surfaces. Cold welds cause the switch to fail in the closed position. If the restoring force of the switch is sufficiently large to break the cold welds, the process increases the surface roughness, which increases the resistivity [6]. Additionally, Au has a very low melting point in comparison to most other noble metals such as Ir, Os, Pd, Pt, Ru, and Rh. Hot welds, or microwelding, can occur due to the Joule heating that occurs in the small contacts. While the Joule heating can anneal the material, decreasing the hardness and increasing the contact area [4, 7], it can also cause the two surfaces to fuse together [3, 4, 6, 8]. Arcing, another form of material transfer, can take material from the cathode to the

anode, causing filament formation and switch failure [1, 3, 6]. Finally, several studies have noted an increasing contact resistance with increasing cycles, but have not examined the cause of this increase [1, 2, 9]. Insulating layers that build up on the contact surfaces due to contamination have also been shown to cause degradation of the contact, and are a suspected failure mechanism [4, 10]. Adhesion, microwelding, arcing, and sudden increases in contact resistance are all failure causes that prevent the ohmic contact switches from reaching their desired lifetime.

1.1.2. Materials

To improve the reliability of ohmic contact switches, alternate material systems to the traditionally used Au have been evaluated. The most popular approach is to form Au alloys to improve the hardness of the material without greatly sacrificing Au's low resistivity. Au-Pt/Pd/Ru alloys have been examined by Lee et al., Chen et al., and Coutu et al. [9-11], while Bannuru et al. studied Au-V and Au-V₂O₅ alloys [12]. While Coutu et al. have observed the evolution of contact resistance under cyclic loading [11, 12], Bannuru et al. have not [13]. Some of the alloys created by Coutu et al. have shown increased lifetimes, but the mechanism behind this lifetime extension has not been examined [11, 12]. Chen et al. noted that Au-Pt/Pd/Ru alloys with greater than 70% Au had lower pull-off forces during cyclic testing [12]. Yang et al. examined Au-Ni alloys that showed significantly increased lifetimes under hot switching [14]. However, the measured resistance is larger for the alloyed materials, due to Matthiessen's rule. Matthiessen's rule states that the resistance should increase with increasing alloy content

due to increased scattering by the alloyed atoms [15]. No microstructural studies were performed that might have determined the cause of an increase in R_c at the end of the test. Microstructural studies could show whether the grain structure was changing or the adhesion layer (used to adhere the metallic film to the substrate) was diffusing into the metallic film. Grain coarsening would decrease the resistivity of the material by decreasing scattering events, while twinning and diffusion of the adhesion layer would increase the resistivity. Analysis of the microstructure would also confirm whether the alloyed material was a solid solution, as predicted by Coutu et al., or whether additional phases had formed. Polyphase materials can have significantly different resistivities than solid-solution alloys. These factors can all affect the contact resistance, and a study that neglects them cannot adequately discuss the causes of device failure.

Mulloni et al. examined Cr/Au layered systems. A 5/150 nm Cr/Au layered system was compared with 5/120/3/30 nm Cr/Au/Cr/Au and 5/110/2.5/10/2.5/30 nm Cr/Au/Cr/Au/Cr/Au layers [16]. The hardness did increase with the additional Cr layers, but the sheet resistance was significantly increased by both annealing and oxygen plasma cleaning that cause oxidation of the Cr layers [16]. Broué et al. examined other pure metals Ru and Rh, along with asymmetric contacts where the first electrode was Au and the other was Ru or Ni [7]. The asymmetric Au-Ru contact had a lower resistance than the Ru-Ru contact (15 Ω for Ru-Ru vs 5 Ω for Au-Ru) [7]. The temperature in the contact was also lower, limiting the softening in the contact [7]. The Ru-Ru contact had negligible adhesion under 30 mA, but the adhesion increased after above 30 mA [7]. The adhesion was lower than an Au-Au contact. Both asymmetric Au-Ru and Au-Ni contacts had negligible adhesion at all currents [7]. Fortini et al. simulated asperity contact

formation and breaking, and found that the Au contact separation was ductile in nature, while the Ru separation was much more brittle [17]. This brittle separation can cause increased roughness of the contact, or even remove the contact film from the substrate, both of which should increase the contact resistance.

While some of the problems of ohmic contact switches are related to problems with Au, others may be due to contamination layers that can form on the surface of the contact. The presence of adventitious carbonaceous layers is well acknowledged, even at the macroscopic contact size [3, 4, 8, 18-21]. While a certain amount of carbon at the surface may help to prevent adhesion [8, 22], it is also believed that the growth of this insulating contamination film may be the cause of increased contact resistance at failure. Various groups have examined limiting the amount of contamination at the surface to determine its effect on contact resistance [10, 19, 21-23]. Jensen et al. have actually hypothesized that for higher voltages at smaller currents, the contamination is burned off, lowering the contact resistance [10]. However, no surface characterization technique such as X-ray photoelectron spectroscopy (XPS) or Auger electron spectroscopy (AES) have been used to confirm the removal of the contamination layer [10]. Alternatively, the change in contact resistance could be due to other causes that would occur with localized heating, such as grain coarsening. Inadequate information is available to distinguish between these possibilities. Yamashita has examined π conjugated hydrophobic self-assembled monolayers (SAMs) on Au [24]. Au coated AFM tips with the SAMs had lower contact resistances (25 Ω) compared to AFM tips with no SAMs (85 Ω) [25]. Yamashita et al. suggest that the lowered contact resistance is due to reduced

contamination at the contact interface [25]. They also noted that the SAMs coating had similar adhesion levels as uncoated Au cantilevers [25].

1.1.3. Testing Methodologies

There are two commonly used techniques to evaluate contact resistance: ball on flat and a cantilever. The ball on flat is essentially an indentation test. A conductive tip is actuated towards a thin film sample. A smaller version of this test using conductive AFM can be performed to evaluate nanoelectromechanical systems (NEMS). In this type of test, the force, displacement, and electrical behavior can be continuously monitored. The dependence of resistance on contact radius is easily examined through this test type, and the applicability of Holm's law to the material system can be investigated. However, this test is susceptible to damage to the tip, since the tip is often reused since it is expensive and time consuming to fabricate. Cantilever tests can either be full scale devices or makeshift switches where the electrodes are actuated towards each other with an outside mechanism, such as a nanoindenter. The loading conditions (both electrical and mechanical) most closely match actual device conditions. In actual devices, the contact force is only inferred by the pull-down force from the actuation method. While the contact forces can be measured with the makeshift switches, the contact area can be harder to determine. Tan et al. has simulated the contact for fixed-free and fixed-fixed electrostatically actuated cantilevers, and has noted that the contact area evolves from partial contact to full contact with increasing force to buckling, where the pull-down electrodes actually make contact and cause the cantilever end with the contact pad to

“swing away” from the bottom electrode [5]. Because the projected contact area is unclear, cantilever tests can leave ambiguity about the actual contact area.

Other methods are used to evaluate properties that are important to RF ohmic contact switches. Specifically, nanoindentation is frequently used to evaluate the hardness to predict contact area for a certain cantilever contact force. Four probe resistivity measurements are also performed to estimate the contact resistance. Atomic force microscopy (AFM) is commonly used to evaluate surface roughness, and either x-ray photoelectron spectroscopy (XPS) or Auger electron spectroscopy (AES) are used to evaluate chemical species at the surface. Scanning electron microscopy (SEM) is frequently used to examine the surface of the contact electrodes after testing, to examine degradation mechanisms.

1.2. Indentation Theory

Indentation testing has long been used to measure the compressive behavior of various materials. More recently, instrumented indentation has been developed to monitor both plastic and elastic deformation of materials. The technique was refined by Oliver-Pharr, after whom the analytical technique is named. The Oliver-Pharr technique will be discussed in Section 1.2.1. A variety of factors can affect indentation tests, and they will be discussed in Sections 1.2.2, 1.2.3, and 1.2.4.

1.2.1. General Theory – Oliver-Pharr Approach

Instrumented indentation allows the elastic and plastic behavior of a material to be evaluated by monitoring force and displacement throughout a test. Additionally, it allows for the calculation of the projected contact area for indents at the nanoscale, where the indents cannot be optically measured. To actually measure the contact area, either atomic force microscopy (AFM) or scanning electron microscopy (SEM) must be used. In order to overcome these shortcomings at the nanoscale, the Oliver and Pharr method utilizes instrumented indentation where force, P , and displacement, h , are recorded as a function of time, t .

The Oliver-Pharr method provides means for inferring the projected contact area to calculate both hardness, H , and reduced contact modulus, E^* , which is defined as:

$$\frac{1}{E^*} = \frac{1-\nu_i^2}{E_i} + \frac{1-\nu_s^2}{E_s} \quad (1.2)$$

where ν and E are the Poisson's ratio and Young's elastic modulus, and the subscripts i and s refer to the indenter tip and sample, respectively. The Oliver-Pharr method also uses a Meyer's hardness approach, where the hardness is represented as the maximum force, P_t , over a projected contact area, A_c , or

$$H = \frac{P_t}{A_c}. \quad (1.3)$$

The contact area is inferred by using a known tip geometry as a function of plastic (or contact) indentation depth, h_p . The contact area is usually represented by a polynomial function

$$A_c = C_0 h_p^2 + C_1 h_p + C_2 h_p^{1/2} + C_3 h_p^{1/4} + \dots + C_n h_p^{1/2^{n-1}} \quad (1.4)$$

where C_i are constants reflecting the tip geometry as a function of indentation depth.

The plastic contact depth, h_p , is itself a function of the maximum indentation depth, h_t , and the elastic indentation depth (the indentation depth that is related to purely elastic deformation), h_e , such that

$$h_p = h_t - \frac{h_e}{2}. \quad (1.5)$$

The maximum depth, h_t , is measured from the raw data, but h_e must be calculated. The majority of the unloading curve is an elastic response to apply the Hertzian solution. The Hertzian solution describes the elastic response under the indenter tip such that

$$P = \frac{4}{3} E^* R^{1/2} h_e^{3/2} \quad (1.6)$$

where R is the indenter tip radius and h_e is the elastic depth (the indentation depth that is related to purely elastic deformation). For the Oliver-Pharr method, the elastic depth is calculated by taking the ratio of Equation (1.6) and its derivative

$$\frac{dP}{dh} = \frac{1}{2} E^* R^{1/2} h_e^{1/2} \quad (1.7)$$

so that

$$h_e = \frac{3P_t}{2S} \quad (1.8)$$

where S is the unloading stiffness at the maximum force and is calculated by fitting the unloading curve to the Equation (1.9) and evaluating the derivative at the maximum depth, as shown in Equations (1.9) and (1.10).

$$P = \alpha(h - h_r)^m \quad (1.9)$$

$$S = \frac{dP}{dh}(h = h_t) = \alpha m(h_t - h_r)^{m-1} \quad (1.10)$$

In the above Equations, α , h_r , and m are fitting parameters. Thus, by combining Equations (1.5) and (1.8), the contact depth is given by

$$h_p = h_t - \frac{3P_t}{4S}. \quad (1.11)$$

To calculate the reduced contact modulus, E^* , the Oliver-Pharr method uses the calculated stiffness, and the contact area derived from the contact depth, so that

$$E^* = \frac{S\sqrt{\pi}}{2\sqrt{A_c}} \quad (1.12)$$

where S is calculated from Equation (1.10) and A_c is calculated from Equations (1.4) and (1.5).

The Oliver-Pharr method has certain assumptions that limit its applicability to different material systems. It assumes that the material is homogenous, amorphous, isotropic and does not strain harden. It also assumes that the contact is perfectly flat, meaning there are no surface or tip asperities that would violate the Hertzian solution assumption that two perfectly round surfaces are contacting each other. These conditions are often violated, especially in the case of thin metallic films. The crystalline structure, frequent texturing of crystallographic orientation of thin films, and constraint by the substrate all violate the homogeneous, amorphous, isotropic requirements. The Oliver-Pharr method also assumes that the material does not strain harden and material does not

pile-up around the indenter tip, which is an inaccurate assumption for many metallic systems. Finally, the analytical techniques assume that the material does not decohere from the substrate or crack. These issues are discussed below, along with several different modeling or analytical solutions that are available for some of the issues discussed above.

1.2.2. Residual Stress Effects

During processing of thin films, residual stresses can often develop. These stresses can create tensile or compressive stresses at the surface of the material, which can affect nanoindentation test results. Additionally, if the hardness and the reduced modulus are well known, then the residual stress of the material can be calculated.

Tsui et al. used aluminum alloy 8009 to perform indentation experiments with a Berkovich tip on uniaxially and biaxially strained bars. The bars were placed in bending, where the indented surface was either put into tension or compression. Using the Oliver-Pharr method, it was found that the hardness and reduced modulus increased in a compressive stress field and decreased in a tensile stress field [26]. While this result was expected for the hardness, which shows a stress state dependence even in macroscaled in Rockwell tests, it was unexpected for the modulus. When the stiffness and contact area were examined (the two parameters used to calculate hardness and moduli values), it was found that the stiffness was invariant with stress state, while the contact area increased with increasing tensile stresses [26]. By examining high magnification optical images of the indentation area, it was found that the Oliver-Pharr calculated contact area, A_{O-P} , was

significantly underestimated from the actual contact area, A_{actual} , for all but the largest tensile stress states due to piled-up material. The contact area was found to be invariant with stress state when measured optically [26]. Thus, when the correct contact area, A_{actual} , was used, both the hardness and modulus were invariant with stress state [26]. Bolshakov et al. used FEM to confirm the experimental results found by Tsui et al. Again, the Oliver-Pharr method underestimated the contact area, but when the actual contact area was measured and used in Equations (1.3) and (1.12), constant hardness and moduli values were found despite the stress state [27].

Kese et al. repeated the experiment by Tsui et al. on a glass sample. Like the experiments by Tsui et al., Kese et al. found that once pile-up was included, the contact area and hardness were invariant with stress state [28]. However, Kese et al. found that the stiffness varied significantly with stress state. For more compressive stress states, the stiffness was higher, causing the reduced modulus to be higher for more compressive stress states [28].

It is unclear whether the results obtained Kese et al. or Tsui et al. are more applicable to a wider range of materials. While the effect of residual stresses on the hardness is intuitive to understand, the effect on the apparent elastic modulus is much more convoluted due its reliance on both the contact area and stiffness. While the true modulus should not change significantly with respect to a large range of stress states, it not clear whether this will bear out during the Oliver-Pharr analysis. There is literature to support both Kese et al. and Tsui et al., and the influence of residual stress on the indentation modulus may vary amongst different material systems.

Theoretically, the indentation data can be used to determine the residual stress in a material. Swadener et al. examined two different approaches to determining the residual stress. The first method used the Hertzian contact solution coupled with the assumption that the mean contact pressure should be an additive function of both the yield stress and residual stress [29]. This method required previous knowledge of both the yield stress and reduced modulus. The second approach again assumed that the mean contact pressure was a function of the residual contact stress and the flow stress, such that

$$\sigma_R = \psi\sigma_f - p_m, \quad (1.13)$$

where σ_R was the residual stress, σ_f was the flow stress, p_m was the mean contact pressure, and ψ was the constraint factor, which was material dependent [29]. The drawback to this approach was that indentation tests must be performed at a known stress state to determine the constraint factor. Suresh and Giannakopolous suggested a third method to determine residual equibiaxial elastic stresses in a material through indentation testing. They proposed that the residual stress state could be derived if the contact area at a specific force was known for the material system without residual stress. The ratio of the contact area under a residual stress to a stress free state was a function of the residual stress. Two different equations were necessary to describe the effect: one for tensile stress states, and one for compressive stress states, as given in the equations below, respectively:

$$\frac{A}{A_0} = \left(1 + \frac{\sigma_R}{p_m}\right)^{-1} \quad (1.14)$$

$$\frac{A}{A_0} = \left[1 - \frac{\sigma_R \cdot \sin(90^\circ - \alpha)}{p_m} \right]^{-1} \quad (1.15)$$

where A was the contact area with residual stress, A_0 was the contact area without residual stress, and α was the effective cone angle for the indenter tip [30]. Thus, if a stress-free state could be obtained, the residual stress in any subsequent experiment could be derived.

The above discussion and theories assume the material was monolithic, and there was no external plastic constraint. However, this is not the case with thin film materials. Suresh and Giannakopoulos purport that the residual stress state for thin film for $P_t/(A_c \cdot E \cdot \tan \alpha) \leq 0.1$ should be described by

$$\sigma_R = \frac{P_t}{2.8A_c}. \quad (1.16)$$

If instead $P_t/(A_c \cdot E \cdot \tan \alpha) > 0.1$, then the following two equations should be solved simultaneously to obtain both σ_u (ultimate strength) and σ_R [30]:

$$\frac{\sigma_u - \sigma_R}{0.29E} = 1 - 0.1419 \frac{h_r}{h_t} - 0.9568 \left(\frac{h_r}{h_t} \right)^2 \quad (1.17)$$

$$\frac{P_t}{h_t^2} = \frac{1.273}{(\tan \alpha)^2} (\sigma_u + \sigma_R) \left[1 + \ln \left(\frac{E \cdot \tan \alpha}{3\sigma_R} \right) \right]. \quad (1.18)$$

All of these solutions required that the reduced modulus be well known a priori to an indentation test, or assumed that the reduced modulus derived from the indentation test accurately reflected that of the material. Therefore, while the ability to determine the stress state of a material is informative, its uses are limited. Most often, there are better means of determining the residual stress state of a material system.

However, it is important to note that the stress state of the material can have a pronounced effect on some of the parameters calculated from indentation data. Most importantly, all researchers have noted that the contact area, A_c , calculated from the Oliver-Pharr method is underestimated in all but the most tensile stress states. If this incorrect contact area is used, abnormally large hardness and reduced moduli will be calculated. If instead the actual measured contact area is used, the hardness becomes insensitive to stress state. The elastic modulus has been shown to be both stress state independent and dependent. Some researchers found the stiffness to be invariant with stress state, while other found it to increase with increasing compressive stresses. If the second case were true, the reduced moduli values would increase even further. Therefore, in the case of a compressive stress state, one would expect the hardness to be the same as in a stress free state, while the reduced modulus would either be the same as or larger than the stress free state.

1.2.3. Surface Roughness Effects

Surface roughness has long been known to be a significant issue in even microscaled indentation tests because it violates the Hertzian contact solution of two smooth round bodies in contact. Surface roughness causes asperities in the contact, which effectively change the contact area during indentation. Because the Oliver-Pharr method infers the contact area instead of providing a direct measurement during the test, surface roughness can overestimate the contact area. Kim et al. provided a rough means of

correcting for this problem by changing the contact depth reference depth. By assuming that 95 percent of the asperity heights were given by

$$\delta_{upper} - \delta_{lower} = \mu \pm 1.96\sigma \quad (1.19)$$

$$\delta_{mean} = \frac{1}{2}(\delta_{upper} + \delta_{lower}) \quad (1.20)$$

where δ_{upper} was the upper height bound of the asperities, δ_{lower} was the lower height bound of the asperities, δ_{mean} was the mean height of the asperities, μ was the mean height value of the asperities, and σ was the asperity height standard deviation, as shown in Figure 1.1. The surface roughness can be related to σ in the following manner [31],

$$\sigma = \sqrt{\frac{\pi}{2}} R_a \quad (1.21)$$

where R_a was the surface roughness given by:

$$R_a = \frac{1}{M} \sum_{i=0}^{M-1} |z_i - \mu| \quad (1.22)$$

where M was the number of data points in the line scan, i was the data point number, z was the height of the data point, and μ was the average height of the line scan. Then, the mean asperity height (as the mean point of the surface asperities), should be given by

$$d_{mean} = 2.46 R_a . \quad (1.23)$$

Since most indentation systems set the zero height as the point at which a prescribed force is exceeded, these systems will label the height as starting from the top of the asperity tips. By subtracting d_{mean} from the contact depth, h_c , before the contact area is calculated, the effect of the asperities is minimized. Kim et al. used this method on nickel and tungsten samples that were polished to different finishes. Before the depth correction,

the moduli were found to decrease with increasing surface roughness. After the correction, the moduli values were independent of surface roughness. However, Kim et al. did not discuss the possibly significant role that residual stresses due to the different polishing procedures may have had on the elastic modulus. Additionally, Kim et al. had only shown this method to be effective for microscaled indents, but it has not been confirmed with nanoscaled indentation tests. Furthermore, this method did not account for how the asperities may be deforming and affecting the general indentation test or for cases when the indenter tip was between the asperities. Nonetheless, Kim et al. have shown their method to remove the hardness and elastic modulus dependency on surface roughness for microscaled indents when the surface roughness was induced by different polishing procedures.

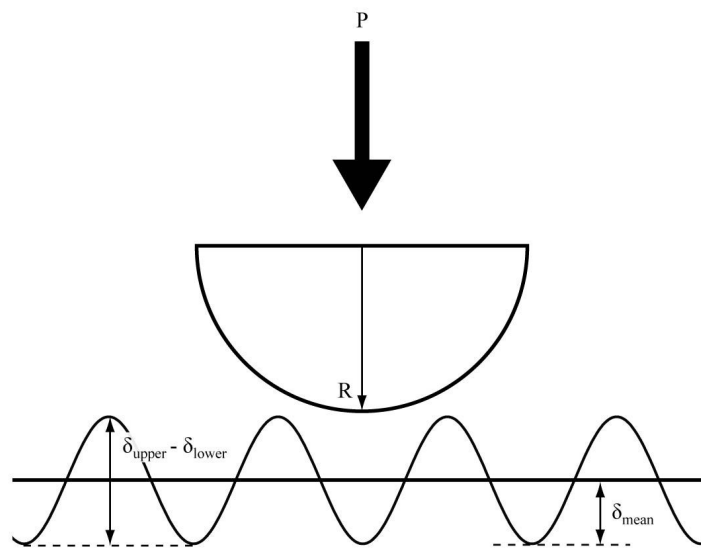


Figure 1.1: Schematic of surface roughness effects during nanoindentation testing.

Other studies have not confirmed low elastic moduli during indentation tests on rough samples, but have instead found that scatter increases with increasing surface roughness. Walter et al. used finite element modeling (FEM) to evaluate the effect of surface roughness of a CrN film on an Si wafer and found that as the surface roughness increased, so did the scatter in the contact area and elastic modulus [32]. They found that for an $R_a=11.1$ nm, the scatter was over 50 percent of the mean value of the modulus [32]. In comparison, for $R_a=2.6$, the scatter was only 28 percent of the mean [32]. Additionally, Walter et al. noticed that the modulus showed no trend with increasing surface roughness, unlike Lee et al. [32]. Bobji et al. noticed an increase in the hardness data scatter due to an increase in surface roughness and a decrease in maximum force when indentation tests were simulated with differing surface roughness [33]. Since different studies have found differing effects due to increasing surface roughness, it is unclear what the actual material response to increasing surface roughness is. Therefore, one should hesitate before trying to extrapolate trends from microscale indentation tests down to the nanoscale.

If the solution proposed by Kim et al. can be extended to nanoscale indentation tests, it may provide an explanation for the low elastic moduli in previous platinum indentation tests [12, 34-36]. However, none of the authors discuss the surface roughness of the sample, so it is impossible to tell if that is the cause of the low moduli values. Additionally, it is unclear if the study by Kim et al. is actually describing a surface roughness or residual stress effect. The increase in hardness and modulus scatter, although important, cannot describe the low modulus values observed by previous platinum indentation tests. Ultimately, while the surface roughness may be the source of

the low moduli values reported in previous platinum indentation studies, it is unlikely a source of anything more than increase scatter in the data.

1.2.4. Thin Film Effects

Thin films present further complications to indentation analyses. When the indent is deep enough to extend the elastic and/or plastic fields into the substrate, then the influence of the substrate must be considered, especially when there is a large mismatch between the hardness and/or elastic moduli of the film and substrate. It is generally accepted that indentations that do not extend further than 10 percent of the film thickness have stress fields within the film only. Therefore, their derived moduli and hardness values should represent the properties of the film and not those of the film-on-substrate. This “10 percent” rule is not based on modeling constraints, but is rather derived from empirical evidence [37]. When indentation depths are more than 10 percent of the film thickness, the deformation response must be described by substrate or membrane models. The substrate and membrane models are distinguished by the film thickness to the contact depth and radius ratios, which will be discussed in Sections 1.2.4.1 and 1.2.4.2 below. Details about each regime will also be given.

1.2.4.1. Substrate Model

Several models have been developed to describe the combined film/substrate response. Additionally, there is often a desire to evaluate film properties independently of the substrate response. To do so, several methods have been derived to isolate the film and substrate effects. Some methods use weighting functions, dictating that the properties

are a mathematical combination of both the film and substrate properties. Another tries to adjust the stiffness used in the Oliver-Pharr method to that of the film only (and not that of the film-on-substrate).

In reference [38], Doerner and Nix assumed that the thin film itself had no gradient in the reduced modulus or hardness. They then used the raw data analyzed with the traditional Oliver-Pharr methodology and fit it to a function of the form

$$\frac{dh}{dP} = \frac{1}{2} \left(\frac{\pi}{A_c} \right)^{1/2} \left\{ \frac{1-\nu_f^2}{E_f} [1 - \exp(\alpha t/h_c)] + \frac{1-\nu_s^2}{E_s} \exp(\alpha t/h_c) + \frac{1-\nu_i^2}{E_i} \right\} \quad (1.24)$$

where the subscripts f , s , and i refer to the film, substrate, and indenter values, respectively. The value dh/dP was the compliance, t was the film thickness, α was an empirical fit parameter, h_p was the plastic indentation depth, and A_c was the projected contact area. Since the compliance was related to the reduced modulus via Equation (1.12), the reduced modulus was represented as

$$\frac{1}{E^*} = \frac{1-\nu_f^2}{E_f} [1 - \exp(\alpha t/h_c)] + \frac{1-\nu_s^2}{E_s} [\exp(\alpha t/h_c)] + \frac{1-\nu_i^2}{E_i} \quad (1.25)$$

where again, f , s , and i represent film, substrate, and indenter, and E^* was the reduced contact modulus. By using this approach, Doerner and Nix found good correlation of Equation (1.24) with their tests of tungsten films on silicon substrates.

King proposes a similar weighted contribution from the tip, film and substrate, so that

$$\frac{S}{S_0} = \frac{\frac{1 - \nu_s^2}{E_s} + \frac{1 - \nu_i^2}{E_i}}{\frac{1 - \nu_f^2}{E_f} \left(1 - e^{-\frac{\alpha t}{a}}\right) + \frac{1 - \nu_s^2}{E_s} e^{-\frac{\alpha t}{a}} + \frac{1 - \nu_i^2}{E_i}} \quad (1.26)$$

where the subscripts “f”, “s”, and “i” refer to the film, substrate, and tip properties, a is the contact radius, t is the film thickness, α is a parameter based on tip geometry and a/t ratios, and S_0 is a normalizing parameter given by

$$S_0 = \beta E^* \sqrt{A_c} \quad (1.27)$$

where the β term is a geometric correction factor, and is equal to 1.129 for a circular punch. By solving Equation (1.26) for $(1-\nu_f^2)/E_f$, the film independent properties can be determined [39]. The parameter α is not available for a/t ratios larger than 4. King and Sullivan also examine the effect of an additional layer on the stress field. They note that when the Young’s modulus of the film is twice that of the substrate, the maximum von Mises stress increases by 40% from the non-layered case and occurs at the film/substrate interface [40].

Another similar weighted approach has been put forth in reference [41]. Gao et al. also proposed a weighting function, but it was derived from a first-order modulus perturbation method. The basis of the model was cylindrical punch theory, which stated

$$h_0 = \frac{P^*(1-\nu)}{4a^* \mu} \quad (1.28)$$

where h_0 was the indentation depth, P was the load, a was the contact radius, and μ and ν were the shear modulus and Poisson ratio, respectively. Using the fact that the work done by the indentation force must equal the loss of strain energy,

$$\frac{1}{2} P \delta h_0 = \int_{V_f} \delta c_{ijkl} u_{ij}^0 u_{kl}^0 dV \quad (1.29)$$

where δh_0 was the change in displacement, c_{ijkl} was the change in elastic modulus from a homogeneous to non-homogeneous film/substrate system, and u_{ij}^0 is the displacement solution for a homogeneous body. By integrating the above equation and substituting it into an equation for elastic moduli,

$$\left(\frac{1-\nu}{\mu} \right)_{eff} = \frac{1-\nu_s - (\nu_f - \nu_s) I_1 \left(\frac{h}{a} \right)}{\mu_s + (\mu_f + \mu_s) I_0 \left(\frac{h}{a} \right)} \quad (1.30)$$

where

$$\begin{aligned} I_1(\xi) &= \frac{2}{\pi} \arctan(\xi) + \frac{\xi}{\pi} \ln \frac{1+\xi^2}{\xi^2} \\ I_0(\xi) &= \frac{2}{\pi} \arctan(\xi) + \frac{1}{2\pi(1-\nu)} \left[(1-2\nu)\xi \ln \frac{1+\xi^2}{\xi^2} - \frac{\xi}{1+\xi^2} \right] \\ \xi &= \frac{h_p}{a} \end{aligned} \quad (1.31)$$

where h_p was the plastic indentation depth and a was the contact radius [41].

The Gao et al. approach had several advantages over the Doerner-Nix model. First, no empirical fitting of the data was required to deconvolute the film and substrate properties. Also, the Gao et al. model could be used for multiple film layers [41]. However, the biggest setback to both the Doerner-Nix and Gao et al. models was that they assumed homogeneous layers where there was no hardness or elastic modulus gradient in the film. This case is unlikely in thin film materials, where processing

methods often induce residual stresses into the films that cause the elastic modulus and hardness to vary with depth.

Another, different approach was used by Han et al. While the Gao et al. and Doerner-Nix models used weighting functions, the model proposed by Han, Saha, and Nix in reference [42] corrected for the how the contact stiffness varies with indentation depth. The method used the fact that stiffness in elastic and elastic-plastic indentation related to contact area in the same way to properly model the hardness of the film. Through the use of the Fredholm integral equation and with known film and substrate Poisson's ratio and film and substrate shear moduli ratio, the contact area ratio between the substrate and film was determined. The film contact area as then used to find the elastic indentation depth. The stiffness was then calculated by taking the slope between three adjacent indentation depths and corresponding loads. This stiffness value was the stiffness of the film and was used to calculate the hardness of the film. The model was demonstrated by Han et al. for experimental data from a 1 micron thick aluminum film on sapphire glass substrate with good results [42].

While this method provided for means of calculating the film hardness from indentation depths of up to 80% of the film thickness, the method had significant drawbacks. The model required that the shear moduli ratio between the substrate and film be known a priori which required additional testing. Additionally, if the Poisson's ratio for both the film and substrate was known, and the ratio between the shear modulus of the film and the shear modulus of the substrate was known, then the rest of the elastic moduli were determined fairly quickly if the substrate shear modulus was known. The prior knowledge of the substrate shear modulus is often the case since most substrate

materials, such as silicon, are well known mechanically. Further, substrate models are limited to situations that are dominated by Hertzian contact stresses. When the film thickness to contact depth or contact radius is sufficiently small, Hertzian contact stresses are no longer applicable. Instead, the deformation in the thin film should be modeled as a membrane on an elastic half space. The details for those modeling scenarios are detailed below in Section 1.2.4.2.

1.2.4.2. *Membrane Model*

When the contact depth and contact radius become a significant fraction of the film thickness, Hertzian contact stresses no longer apply. Instead, the film behaves as a membrane on an elastically deforming half-space. According to Vanimisetti and Narasimhan, the transition to membrane stresses occurs when $h/t \approx 0.025-0.05$ and $a/t \approx 0.2-0.3$, but the transition is best predicted by the a/t ratio [43]. Another strong indicator of membrane stresses is when the power law exponent, m , for the force-displacement relationship $P=ah^m$ is significantly smaller than the Oliver-Pharr predicted 1.5 [43].

For membrane loading, Vanimisetti and Narasimhan predict that the force, P , should be a complicated function, such that

$$P = E_f R_i^2 f \left(\frac{h}{R_i}, \frac{t_f}{R_i}, \frac{E_s}{E_f}, \frac{\sigma_{\text{yield}, s}}{E_s}, \frac{\sigma^R}{E_f}, \text{others} \right) \quad (1.32)$$

where E is the Young's modulus, subscripts f and s refer to the film and substrate, respectively, R_i is the tip radius, h is the contact depth, t_f is the film thickness, $\sigma_{\text{yield}, s}$ is the yield stress of the substrate, and σ^R is the residual stress in the film [43]. By including the "others" term, Vanimisetti and Narasimhan acknowledge that there could be additional factors that could influence the deformation response. Because the deformation

response is extremely complicated, Vanimisetti and Narasimhan used finite element analysis (FEA) to explore the behavior of a thin ceramic membrane on a substrate, where the ceramic is defined as a linear elastic solid, and the substrate is modeled with J_2 flow theory of plasticity. The model is meant to simulate an oxide layer on a metallic substrate. In their study, they found that as a/t increased, the tensile radial and circumferential stresses at the membrane/substrate interface became larger [43]. Additionally, compressive biaxial stresses in the film created tensile stresses in the substrate and caused early onset yielding, effectively decreased the measured hardness [43].

Ramsey, Chandler, and Page utilize thin plate elastic models to predict the role a membrane on the contact deformation. For small deformations where the displacement is less than the thickness of the membrane, the force-displacement relationship is given by

$$h_{max} = \frac{P}{8\sqrt{Dk}}$$

$$D = \frac{E_f t_f^3}{12(1 - \nu_f^2)} \quad (1.33)$$

$$k = \frac{0.383}{t_f} \left(\frac{E_s}{1 - \nu_s^2} \right)^{\frac{4}{3}} \left(\frac{1 - \nu_f^2}{E_f} \right)^{\frac{1}{3}}$$

where again, E and ν are the Young's modulus and Poisson's ratio, respectively, subscripts f and s refer to the film (membrane) and substrate properties, respectively, and t_f is the film (membrane) thickness [44]. They also detail a solution for large plate deflection (where the indentation depth is greater than the film thickness), but acknowledge that the solution is a simplification based on the elastic behavior of the

substrate and membrane, and that the substrate yield stress is a better predictor of deformation behavior [44].

Some experimental work has also been done on elastically stiff membranes on more compliant substrates. McGurk and Page evaluate a range of hard thick coatings ($>1 \mu\text{m}$) on metallic substrates. For large loads (that generate indentation depths significantly greater than the coating thickness), they see an increase in hardness [45]. However, at small loads (generating indentation depths less than 2 times the coating thickness), the hardness actually decreases [45]. McGurk and Page also noted that when the coating fractures, the hardness can be predicted by

$$\frac{\Delta H}{H_s} = \frac{E_f t_f^3}{h^3 H_s} \quad (1.34)$$

where ΔH is the change in hardness due to the presence of the film, H_s is the substrate hardness, E_f is the Young's modulus of the film, t_f is the film thickness, and h is the contact depth [45]. They do note that when the coating does not fracture, the above relationship is not obeyed.

While models do exist for membrane stresses in indentation testing, the models either have significant limitations or are prohibitively complex. Additionally, although there are experimental studies of membrane deformation, they do not examine the case of an ultra-thin coating that may be plastically deforming as well. Further, experimental studies do not examine the effect that the membrane will have on the Oliver-Pharr calculated plane strain modulus.

1.2.5. Adhesion Effects

When the contact forces are small, adhesive forces can be a significant contribution. To account for the adhesive forces, the Johnson-Kendall-Roberts (JKR) and the Derjaguin-Müller-Toporov (DMT) models were developed. While the Hertzian contact model does not account for adhesion, the JKR and DMT models do. The JKR model assumes the adhesion force, F_{adhesion} , is represented as

$$F_{\text{adhesion, JKR}} = 2\pi RW \quad (1.35)$$

where R is the tip radius and W is the adhesion work per unit area [46]. Alternately, the DMT model represents the adhesion force as

$$F_{\text{adhesion, JKR}} = \frac{3}{2}\pi RW \quad (1.36)$$

where R and W are the same as for the JKR method [46]. For both models, the adhesion work, W , is the negative of the Gibb's free energy change per unit area ($-\Delta G$), which can be calculated from the surface energy, γ , of the two contact materials in a medium (such as air, water, or alcohol). The equation for the adhesion work is

$$W = \gamma_{1m} + \gamma_{2m} - \gamma_{12} \quad (1.37)$$

where 1 and 2 refer to the different contact materials and m refers to the medium the contact is made in [46, 47]. The JKR method assumes that the only attractive forces occur within the contact area, while the DMT method includes additional long-range surface forces [47]. Because they assume different attractive forces, the JKR method is best suited towards high surface energy, large radius contacts (such as nanoindentation of polymer materials), while the DMT is best suited to low surface energy, small radius contacts (like AFM examinations of metallic materials) [47].

For nanoindentation of thin metallic films, the adhesion force should be a small fraction of the maximum indentation force, but should be a much larger fraction for AFM examinations, where much smaller maximum forces are used. Further, because RF MEMS ohmic contact have restoring forces that can be as low as $30 \mu\text{N}$, limiting adhesive forces is important to device viability.

Researchers have found dispirit adhesion response for Au/Au contacts. Broué et al. found that there was significant adhesion in Au/Au contacts regardless of the current sourced through the contact [7]. However, Patton and Zabinski found that there is no adhesion between an Au tip and Au film until the contact undergoes rapid switching at zero or low currents [3]. Patton and Zabinski also examined aging of the contact, and found that after initial adhesion is established, aging the contact decreased the adhesive forces, likely due to increasing contamination at the surface that increased the separation of the Au surfaces and reduced van der Waals forces [3]. Broué et al. also examined Ru/Ru contacts, and found that they exhibit no adhesion until 30 mA [7]. When they examined asymmetric Au/Ru contacts, the adhesion forces were very small over a large range of currents [7].

Three types of separation are noted for contacts: ductile, brittle, and delamination. Ductile contacts exhibit necking at the contact region before separation. Brittle contacts separate along the original interface or along grain boundaries in the contact. Delamination occurs for thin film contacts when one of the contact films delaminate from its substrate. Fortini et al. utilized molecular dynamics (MD) modeling to explore separation for Au/Au and Ru/Ru contacts, and found that at room temperature, the Au contacts exhibited ductile failure, while the Ru contacts were more brittle in nature,

although the Ru contacts had more ductility at 600 K [17]. Gilbert, Mall, and Leedy note that contacts that undergo brittle separation have the longer lifetimes in RF MEMS ohmic contact switches than those with ductile separation [48].

1.3. Contact Resistance Theory

Contact resistance is an often studied part of power consumption in RF MEMS ohmic contact switches. The contact resistance arises from increased current density through the smaller volume contact, which leads to higher resistances. For traditional bulk materials, Holm's law describes the contact resistance, R_c , as

$$R_c = \frac{\rho_1 + \rho_2}{4a} \quad (1.38)$$

where ρ_1 is the resistivity of the first contact, ρ_2 is the resistivity of the second contact, and a is the contact radius. Holm's law assumes that both contacts are monolithic materials, and that diffusive current conduction occurs at a single contact spot. It also neglects any thermal effects that may be occurring in the sample. In the following sections, the effects of ballistic conduction, thin films, and thermal effects on the contact resistance will be examined.

1.3.1. Ballistic Transport

The mean free path of electrons is the average distance an electron travels before being scattered. Scattering events increase the resistance of the material. Holm's law assumes diffusive transport, where the contact radius is larger than the mean free path for

the material. When the contact radius is smaller than the electron mean free path, additional scattering occurs and increases the contact resistance. To model the ballistic transport through the contact, various researchers have used the Sharvin resistance equation

$$R_{\text{ballistic}} = \frac{4\rho K}{3\pi a} \quad (1.39)$$

$$K = \frac{l}{a}$$

where $R_{\text{ballistic}}$ is the ballistic transport resistance, ρ is the resistivity, a is the contact radius, l is the mean free path, and K is the Knudsen parameter [2, 49]. To model a combination of larger asperities that support diffusive transport and smaller asperities that have ballistic transport, researchers have suggested a weighted function,

$$R = R_{\text{ballistic}} + \Gamma(K)R_{\text{Holm}} \quad (1.40)$$

$$R = \frac{4\rho K}{3\pi a} + \Gamma(K)\frac{\rho}{2a}$$

where $\Gamma(K)$ is a weighting parameter based on the Knudsen parameter [49]. However, neither pure ballistic transport, as given by Equation (1.39), or a weighted diffusive and ballistic transport, as given by Equation (1.40), are able to successfully describe the measured resistances in RF MEMS ohmic contact switches.

1.3.2. Geometric Effects

Geometric factors need to be considered when calculating potential drops in the sample and the contact resistance. The resistance through the sample and tip can be modeled as a series resistance to the contact resistance. In bulk materials, there are

hemispheres of equipotential, so that measured voltage, V , for a Kelvin probe (4-wire) configuration is

$$V = \frac{\rho I}{2\pi} \left(\frac{1}{s_1} - \frac{1}{s_2} - \frac{1}{s_3} + \frac{1}{s_4} \right) \quad (1.41)$$

where ρ is the resistivity, I is the current, and s_i are given in Figure 1.2 [50]. However, there are cylinders of equipotential within a thin film, so that the voltage is instead given by

$$V = \frac{\rho I}{2\pi t} \ln \left(\frac{s_2 s_3}{s_1 s_4} \right) \quad (1.42)$$

where t is the film thickness [50]. The resistance in a thin film sample will be significantly higher than the resistance in a monolithic material.

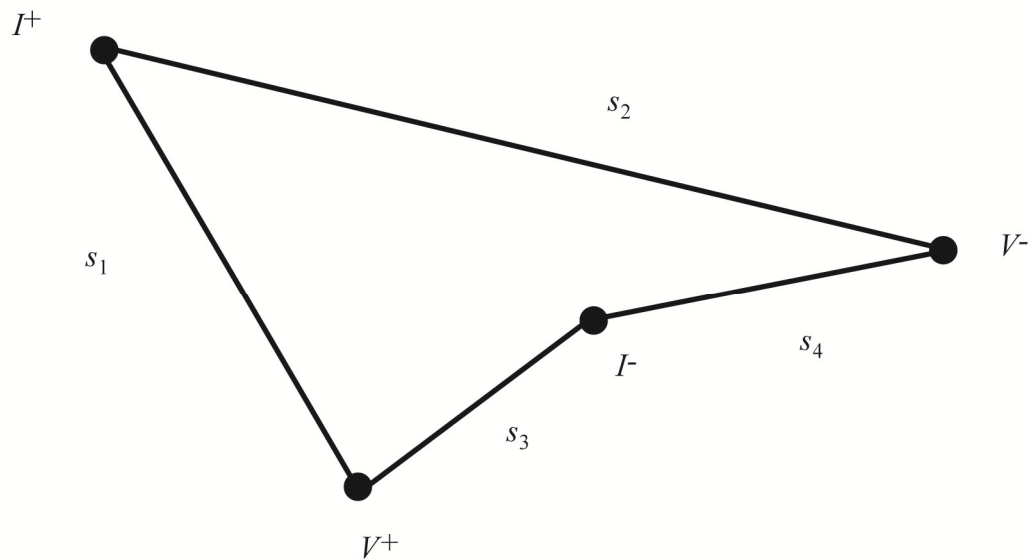


Figure 1.2: Randomly place four probe configuration.

Just as geometric factors affect the resistance in a thin film material, contact resistance is also affected by geometric constraints. Timsit found that the contact

resistance is affected by the contact radius to film thickness ratio (a/t), and developed a multiplying correction factor \overline{R}_c [51]. Zhang et al. have extended work by Timsit to a larger range of a/t ratios. The corrected contact resistance for a cylindrical contact is given by

$$R_c = \overline{R}_c \frac{\rho}{2a} \quad (1.43)$$

where \overline{R}_c is dependent on the ratios of the resistivities of the contact materials and the a/t ratio. When $\rho_1 = \rho_2$,

$$\overline{R}_c \approx \begin{cases} 1.0404 - 2.2328 \frac{a}{t} + 5.069 \left(\frac{a}{t}\right)^2 - 7.5890 \left(\frac{a}{t}\right)^3 + 6.5898 \left(\frac{a}{t}\right)^4 \\ \quad - 2.9466 \left(\frac{a}{t}\right)^5 + 0.5226 \left(\frac{a}{t}\right)^6, & \frac{a}{t} \leq 1.6 \\ 0.4571 - 0.1588 \ln \left(\frac{a}{t}\right) + 0.1742 \left[\ln \left(\frac{a}{t}\right)\right]^2 - 0.0253 \left[\ln \left(\frac{a}{t}\right)\right]^3 \\ \quad + 0.0015 \left[\ln \left(\frac{a}{t}\right)\right]^4, & 1.6 < \frac{a}{t} \leq 100 \end{cases} \quad (1.44)$$

where a is the contact radius and t is the film thickness [52]. When the resistivity of the two contact materials is different, \overline{R}_c is a more complicated function, and is given by

$$\overline{R}_c = \overline{R}_{c0} \left(\frac{a}{t}\right) + \frac{\Delta \left(\frac{a}{t}\right)}{2} \frac{2\rho_1}{\rho_1 + \beta \left(\frac{a}{t}\right) \rho_2} \quad (1.45)$$

where ρ_1 is the resistivity of a thin cylindrical (simulating a tip), and ρ_2 is the resistivity of a thin film (simulating the sample), and the other terms are calculated parameters given by [52]

$$\begin{aligned}
\overline{R_{c0}} &\approx \begin{cases} 1 - 2.2968 \frac{a}{t} + 4.9412 \left(\frac{a}{t}\right)^2 - 6.1773 \left(\frac{a}{t}\right)^3 + 3.811 \left(\frac{a}{t}\right)^4 \\ \quad - 0.8836 \left(\frac{a}{t}\right)^5, & 0.001 \leq \frac{a}{t} \leq 1 \\ 0.295 + 0.037 \left(\frac{t}{a}\right) + 0.0595 \left(\frac{t}{a}\right)^2, & 1 < \frac{a}{t} < 10 \end{cases} \\
\Delta &\approx \begin{cases} 0.0808 + 0.0073 \frac{a}{t} + 0.0184 \left(\frac{a}{t}\right)^2, & 0.001 \leq \frac{a}{t} \leq 1 \\ 0.0409 \left[\ln\left(\frac{a}{t}\right)\right]^4 - 0.1015 \left[\ln\left(\frac{a}{t}\right)\right]^3 + 0.265 \left[\ln\left(\frac{a}{t}\right)\right]^2 \\ \quad - 0.0405 \ln\left(\frac{a}{t}\right), & 1 < \frac{a}{t} < 10 \end{cases} \\
\beta &= 0.0016 \left(\frac{a}{t}\right)^2 + 0.0949 \frac{a}{t} + 0.6983, \quad 0.001 \leq \frac{a}{t} < 10
\end{aligned} \tag{1.46}$$

These complicated correction factors increase the predicted contact resistance, up to a factor of 1.5 when $a/t=100$ for the special case of $\rho_1=\rho_2$ [52]. For large a/t ratios, significant errors can be introduced if thin film contact resistance effects are not considered.

1.3.3. Thermal Effects

The large current densities that can be present in electrical contacts can cause significant heating of the contact material. The Wiedemann-Franz law estimates the contact temperature, T_c , as

$$T_c = \sqrt{\frac{V^2}{4L} + T_i^2} \tag{1.47}$$

where V is the voltage drop across the contact, L is Lorentz constant ($2.45 \times 10^{-8} \text{ V}^2/\text{K}^2$), and T_i is the ambient temperature [50]. The Wiedemann-Franz law holds for a large

number of materials at room temperature and warmer. A 10 mV voltage across the contact only increases the temperature 6°C above room temperature and can be safely neglected. If the voltage drop across the contact is larger, softening or annealing of the contact materials can occur [53]. This softening increases the contact radius, decreasing the contact resistance. Further, heat dissipation can be restricted in thin film materials, which can decrease the softening temperature of the contact materials [53].

1.4. Investigation of Ultra-thin Coatings for Ohmic Contact Switches

To explore the applicability of ultra-thin Ru and Pt coatings to Au films for RF MEMS ohmic contact switches, both the mechanical and electrical behavior will be evaluated. The testing methodology will be described in Chapter 2. Nanoindentation testing on the ultra-thin coating will be compared with the Au-only behavior in Chapter 3. Additionally, fundamental understanding of the deformation of hard, ductile thin coatings on a soft, compliant substrate will be furthered through this study. The nanoindentation results in Chapter 3 show that ultra-thin coatings can actually increase the contact area. In Chapter 3 we explore whether the increased contact area for the ultra-thin coatings can actually reduce the contact resistance. Through this study, we found that the conduction through the transmission line between the source and drain is actually a much larger source of resistance than the contact resistance. Ultra-thin coatings allow most of the conduction to occur in the low resistivity Au film, keeping the power consumption of the device low despite the higher resistivity coating. Stiction and friction studies are detailed in Chapter 5 to show that the ultra-thin coatings have improved wear

resistance, which should increase the reliability of the systems. Finally, conclusions on the entirety of the work are detailed in Chapter 6.

Chapter 2

Methods

A series of Au thin films were coated with sputter deposited ultra-thin Ru and Pt coatings to evaluate the improvement in ohmic contact switches. The Ru coating was chosen due to its limited solubility with Au (Figure 2.1). Alternately, the Pt coating was chosen because it has the same crystal structure as Au, and also has large amounts of solid solubility with Au (Figure 2.1). The films were characterized with a variety of techniques to determine the chemistry and structure of the fabricated films, as described in Section 2.1. The coated films were mechanically evaluated using a nanoindenter, and analyzed using the Oliver-Pharr method, as described in Section 2.2. The coated films were also analyzed under coupled electrical and mechanical loading, to determine their behavior in ohmic contact switches (Section 2.3). Both single and cyclic tests are evaluated. Finally, surface adhesion is examined for both new and aged coated systems, and compared to the Au film behavior (Section 2.4).

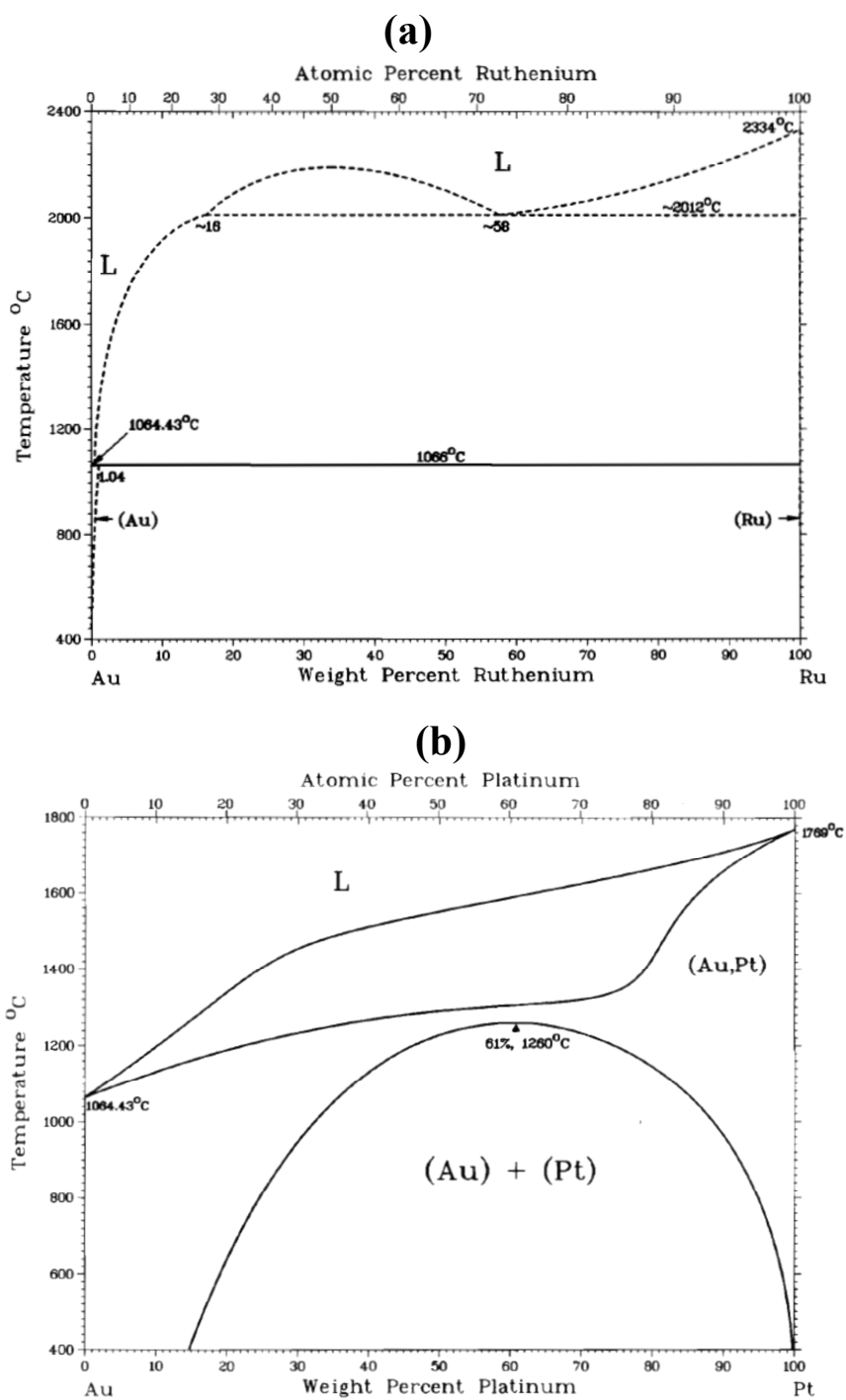


Figure 2.1: Phase diagram for a) Au-Ru binary systems (reprinted from [54]) and b) Au-Pt binary systems (reprinted from [54]).

2.1. Fabrication and Characterization of Thin Films

To evaluate the effect of an ultra-thin conductive coating on a thin Au film in ohmic contact switches, a series of blanket films were fabricated. Two Au film thicknesses, 350 and 450 nm, were sputter deposited from a 99.99% pure Au target on a (100) oriented Si wafer with an intact oxide layer. In some cases a native oxide was present, and others had a thermally grown oxide layer. In order to promote adhesion between the Au film and the Si substrate, a 20 nm Cr layer was sputter deposited first from a 99.95% pure Cr target (Figure 2.2).

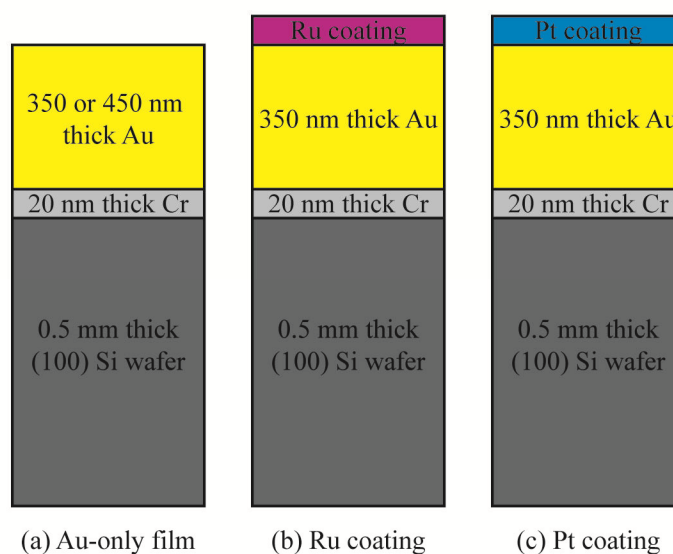


Figure 2.2: Schematic of a) Au film, b) Ru coated films, and c) Pt coated films. Schematics are not to scale.

The Au film was deposited at 2 mTorr. Other sputtering pressures were evaluated, but were found to generate a surface roughness too large for small scale (<15 nm) indentation testing. Scanning probe microscopy (SPM) with a Bruker Icon Atomic Force

Microscope in ScanAsyst mode was used to evaluate surface roughness. A 512 pixels/line, 0.501 Hz scan of a 2 μm x 2 μm section of the surface 2 mTorr sputter deposited Au layers had a surface roughness, R_q , of 1.86 nm. The surface roughness is given by

$$R_q = \sqrt{\frac{\sum Z_i^2}{N}} \quad (2.1)$$

where Z_i is the height of each measured point, and N is the total number of points.

While the 2 mTorr sputtering pressure created films with low surface roughness, it did generate large residual stresses. Wafer curvature measurements performed with Tencor FLX2330 revealed a small compressive residual stress (~ 80 MPa) in the Au film. The low sputtering pressure also generated extremely small grain structure. To evaluate the grain structure, 100 nm of Au was deposited on a rocksalt substrate. The rocksalt was then dissolved in deionized (DI) water, and then placed on a nickel transmission electron microscope (TEM) grid. The TEM image in Figure 2.3 showed polycrystalline, untextured grains approximately 5-30 nm in size.

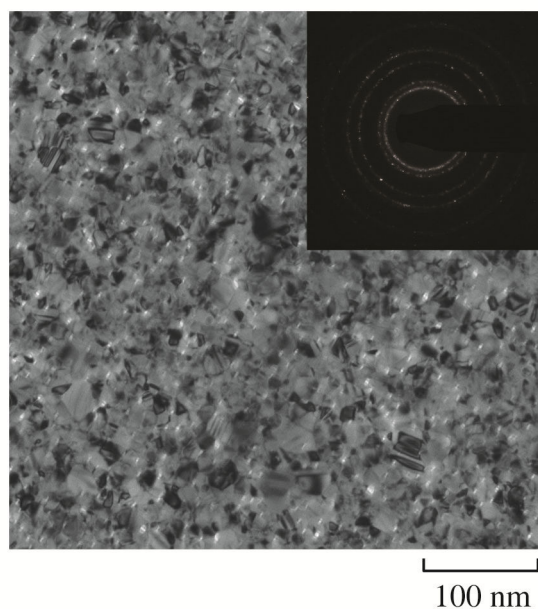


Figure 2.3: TEM image of Au film grain structure showing small (5-30 nm) grains.

Cross-sections of the Au film coated with 5 nm of Ru show deposited on an Si substrate have a different grain structure than the films released from the rocksalt substrate, as shown in Figure 2.4. While the grains are slightly larger in the cross-section, they are still less than 100 nm. Additionally, the grains have a high dislocation density and are heavily twinned. The small grain structure and defect population give rise to a relatively large resistivity for thin film Au. Four probe resistivity measurements on the Au film measured the resistivity as $69 \Omega \cdot \text{nm}$. The four probe resistivity measurements were performed with a Signatone 4 point probe station with 4 collinear tungsten carbide probes evenly spaced 1.27 mm apart and pushed into the surface of the film with 85 g. The electrical measurements were made with a Keithley 2400 SourceMeter, with 10 mA of current source, and the lowest voltage measurement range (200 mV) selected. The measurements were repeated in 5 different areas of the film to ensure that there were no edge effects. The resistivity of the material, ρ , was calculated as

$$\rho = \frac{\pi t V}{\ln(2) I} \quad (2.2)$$

where V is the measured voltage, I is the sourced current, and t is the film thickness.

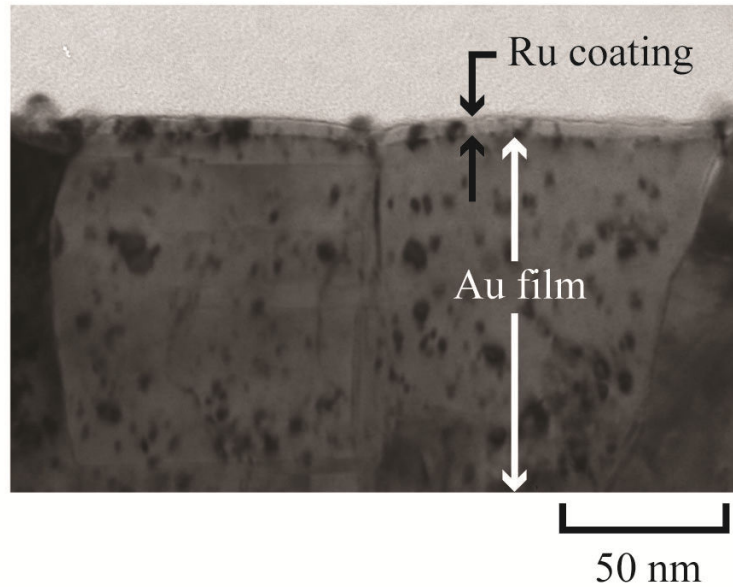


Figure 2.4: TEM image of Ru coated Au film cross-section.

To evaluate the mechanical and electrical response of a layered system, Ru and Pt were deposited on sectioned pieces of the 350 nm Au film (Figure 2.2). To minimize any confusion between the Au layer and the Ru or Pt layers, the Au will be referred to as the Au film throughout this dissertation. Additionally, the Ru and Pt layers will be referred to as the coating. Five different Ru coating thicknesses were deposited from a 99.95% pure Ru target: 5, 10, 20, 50, and 100 nm. The Ru coatings were deposited at 2 mTorr. To evaluate the role of residual stress on both the mechanical and electrical behavior, the 10 nm thick Ru coating was also deposited at 5 mTorr (in addition to 2 mTorr). Since lower

sputtering operating pressures have more energetic bombardment of the sample surface, a lower sputtering pressure will lead to a more compressive residual stress in the coating [55]. The Ru layer was chosen due to its extremely low solid solution solubility with Au to ensure a bilayer system with little reactivity at the interface [54]. To determine if the response is different when there is large scale solid solution solubility with the Au layer, three different Pt coatings were also deposited on sectioned pieces of the Au film from a 99.99% pure Pt target [54]. Prior to deposition of the Ru and Pt coatings, the Au films were cleaned in two 20 min baths in acetone, then two 20 min baths of either methanol or isopropyl alcohol. The samples were then dried with dry N₂, and then loaded in the vacuum chamber of the deposition system. Due to concerns about residual organic contamination at the Au/Ru or Au/Pt interface, one sample had a 20 nm Cr adhesion layer deposited at 5 mTorr, a 350 nm Au layer deposited at 2 mTorr, and a 10 nm Ru layer deposited at 2 mTorr without breaking vacuum between any of the steps. This sample will be referred to as the 10 nm Ru coating without venting. A summary of all the Au films and Ru or Pt coatings are given in Table 2.1.

Table 2.1: Film deposition summary

Layer 1			Layer 2			Comments
Material	Thickness (nm)	Sputtering Pressure (mTorr)	Material	Thickness (nm)	Sputtering Pressure (mTorr)	
Au	350	2	N/A	N/A	N/A	
Au	450	2	N/A	N/A	N/A	
Au	350	2	Ru	5	2	
Au	350	2	Ru	10	2	
Au	350	2	Ru	20	2	
Au	350	2	Ru	50	2	
Au	350	2	Ru	100	2	
Au	350	2	Pt	10	2	
Au	350	2	Pt	50	2	
Au	350	2	Pt	100	2	
Au	350	2	Ru	10	5	
Au	350	2	Ru	10	2	No vent between Au and Ru layer
Ru	100	2	N/A	N/A	N/A	
Pt	100	2	N/A	N/A	N/A	

Like the Au film, the Ru coated samples were very smooth. The surface roughness of the 5 nm Ru coating increased slightly more than the Au only film. Using the same scanning parameters as for the Au film, the R_q of the 5 nm Ru coating was 3.51 nm. Also like the Au sample, 100 nm of Ru and Pt were deposited on freshly cleaved rocksalt substrates. Then, the freed Ru and Pt films were placed on TEM grids. Like the Au film, both the Ru and Pt films were nanocrystalline aggregated with grain sizes 5-30 nm (Figure 2.5).

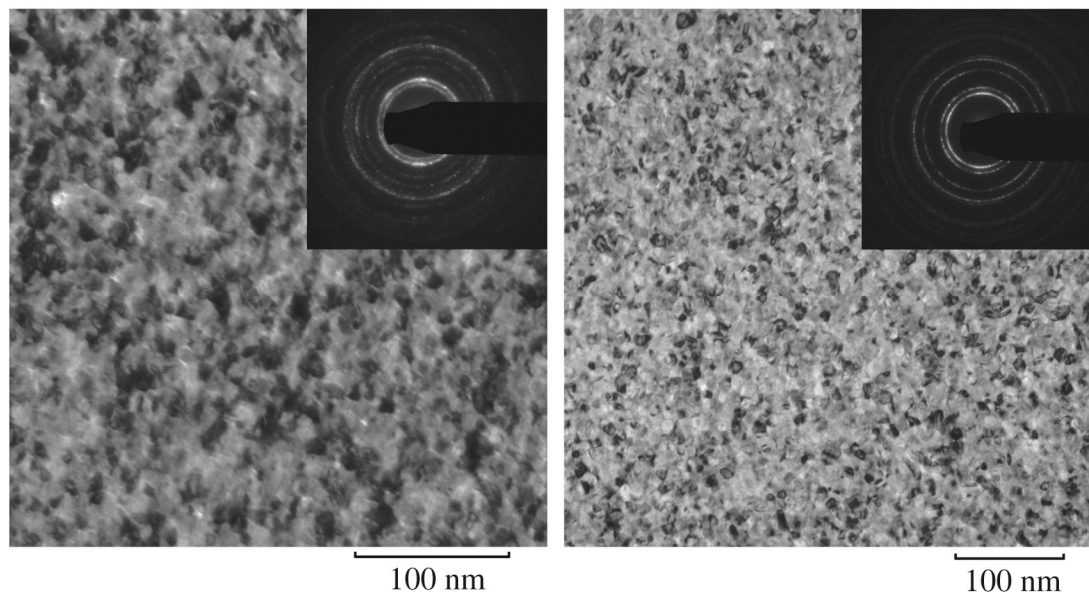


Figure 2.5: TEM image of a) Ru film grain structure and b) Pt film grain structure. Both had ultra-fine grain sizes between 5-30 nm.

To determine if the ultra-thin coatings (<20 nm) were still crystalline, 5 nm of Ru and 10 nm of Pt were deposited on TEM grids with 20 nm thick silicon nitride amorphous windows (from TEMwindows.com). Selected area diffraction (SAD) patterns of the Ru sample had very diffuse rings (Figure 2.6a). The diffracted rings corresponded to the strongest diffracted hexagonal close packed (HCP) rings. The diffuse nature of the rings is most likely due to extremely small grains; it was difficult to image the grain structure in bright field mode. The Pt sample also had a diffracted ring pattern, but these rings were much more distinct due to larger grain sizes because of the thicker nature of the film (Figure 2.6b). The Pt diffracted rings correspond to those expected for face centered cubic (FCC) materials. Further, grains found in bright field imaging were 5-20 nm, similar to those seen in the rocksalt depositions. Thus, polycrystalline Ru and Pt layers can be obtained, even for very thin layers.

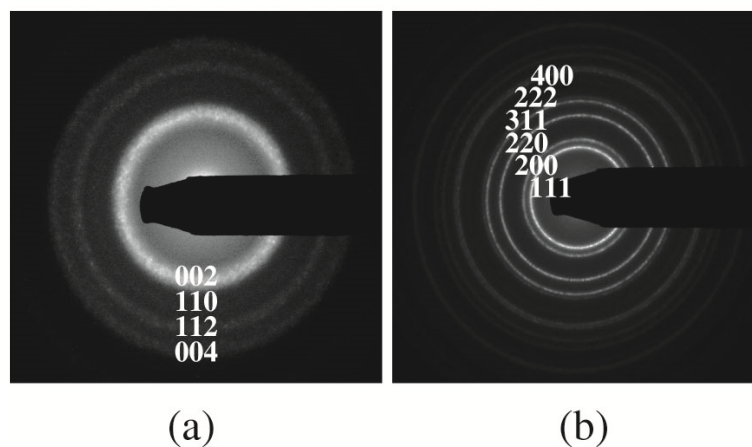


Figure 2.6: SAD image of a) 5 nm Ru coating and b) 10 nm Pt coating on amorphous silicon nitride TEM windows.

We also examined whether the coatings were continuous on the surface of the Au film. To do so, we used Auger electron spectroscopy (AES) with a Physical Electronics 670. Both the 5 and 10 nm Ru coatings were examined. A scan from 50 to 2750 eV showed no evidence of an Au peak, and only Ru, C, and O peaks were present (Figure 2.7). To verify the lack of an Au peak, a detailed scan from 1900 to 2400 eV was performed (Figure 2.7b). There should be an Au peak at 2022 eV, and a Ru peak at 2256 eV. Several scans showed only the Ru peak, and no Au peak. This absence is significant, because the selectivity of the 2022 eV Au peak is much higher than that of the 2256 eV Ru peak [56]. Therefore, if there was Au film that was uncoated by the Ru layer, the Au peak at 2022 eV should appear. Its absence is a strong indicator that even the 5 nm Ru coating is continuous on the Au surface. Additionally, TEM cross-sections of the 5 nm Ru coating also show a continuous layer of Ru, as seen in Figure 2.4. The Ru layer appears to be conformal to the underlying Au layer, again suggesting that the Ru layer is continuous.

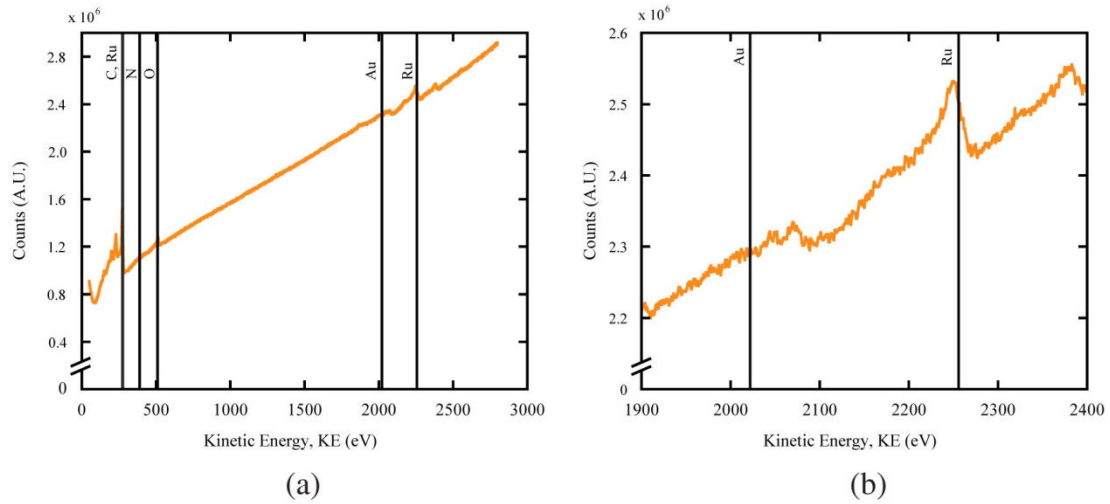


Figure 2.7: AES scan of 5 nm Ru coating for a) full spectrum and b) detailed scan of expected Au and Ru peaks, with expected peaks shown as black vertical lines.

Four probe resistivity tests were also performed on Ru and Pt films that were deposited directly onto a Si substrate. The Ru and Pt film were 100 nm thick. The Ru film had a resistivity of $7.75 \mu\Omega\cdot\text{cm}$, and the Pt film had a resistivity of $8.19 \mu\Omega\cdot\text{cm}$. These were close to the noted resistivity of the Au film.

2.2. Nanoindentation Testing

Nanoindentation tests were performed to evaluate whether the contact area and mechanical deformation would be significantly affected by the presence of a harder surface layer (Ru or Pt). The experimental methods are detailed in Section 2.2.1, and the methods to analyze the experimental data are given in Section 2.2.2.

2.2.1. Experimental Methods

Force-controlled indentation tests were performed using diamond, conospherical indenter tip with a nominal radius of 500 nm. The force on the indenter tip was increased at a constant loading rate, held at the maximum force for 10 s, and then unloaded at the same rate as during loading. For these indents, maximum forces of 75, 300, and 600 μN were used, and loading/unloading rates of 100 $\mu\text{N/s}$ were used for each peak load condition. These trapezoidal loading functions are shown in Figure 2.8. The maximum forces were chosen to correlate to indentation depths that were on the order of the Ru and Pt coating thickness, and 10 and 20% of the Au film thickness. Ten indents were performed for each combination of maximum force and loading rate. The indents were placed on a 20 μm square grid, to ensure that the spacing between indents was greater than ten times the lateral extent of the largest indent (thereby preventing interaction between individual measurements).

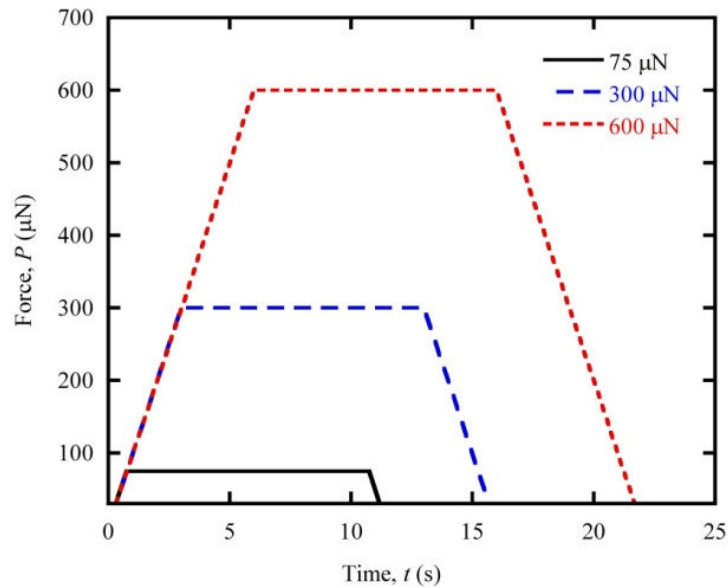


Figure 2.8: Load control command waveforms for the 75, 300, and 600 μN maximum force indents.

During the indentation tests, a preload of 1.0 μN was used to determine the location of the surface. Once on the surface, the indenter was held for 60 s at 1.0 μN . The last 30 s of this hold time were used to calculate the instrument's displacement drift rate.

Displacement drift rates in all tests were found to be between ± 0.1 nm/s. Immediately prior to the drift measurement and immediately following the indentation test, an *in-situ* image of the topography indentation surface area was obtained using the indenter tip as a probe. The image size was set as 1 by 1, 2 by 2 and 3 by 3 μm for the 75, 300 and 600 μN maximum indentation force conditions, respectively (all images were 256 by 256 pixels). These images were used to verify that the indentation areas for all indents were free of debris or other gross defects prior to the indentation test and to quantify the amount of piled-up around the indenter tip during the indentation test.

2.2.2. Analytical Methods

The Oliver-Pharr theory was reviewed in Section 1.2.1. In this section, its implementation is discussed. To analyze the instrumented indentation data, user-created Matlab® (The MathWorks, Massachusetts) scripts were created. First, the raw data was read in from files created by the Hysitron Triboscan software (Triboscan®, Hysitron Inc.). The raw displacements were already drift corrected by the Triboscan software so that:

$$h' = h - \dot{h}_{drift} t \quad (2.3)$$

where h' was the drift corrected displacement, h was the raw displacement, \dot{h}_{drift} was the drift rate, and t was the time. The raw displacements are also compliance corrected, so that

$$h'' = h' - C_m P \quad (2.4)$$

where h'' was the drift and machine compliance corrected displacement, h' was the drift corrected displacement, C_m was the machine compliance, and P was the force. The procedure to determine the machine compliance is discussed in Section 2.2.2.2. The Triboscan software set $t=0$ as the start of the test and $h=0$ when 2 consecutive data points have forces above the user-determined preload. For all the indentation tests in this study, the preload was set to 1.0 μN .

The data was then parsed by time to find the loading, hold, and unloading portions of each indentation test. Once the unloading period was identified, the data was searched for the maximum force, P_t . The maximum indentation depth, h_t , was taken as the displacement at the maximum force. After the data is parsed, the unloading curve is then fit using Matlab's® *nlinfit* script to the form

$$P = \alpha(h - h_r)^m \quad (2.5)$$

where P is the force, h is the displacement, and α , h_r , and m are fitting parameters. To fit the equation, the top 5 and bottom 20 percent of the data is removed to eliminate artifacts due to tip stiction and friction issues that can occur at those points in the indentation tests. The residual depth parameter, h_r , was found from fitting the equation (as opposed to using the displacement when $P=0$ on unloading). The stiffness of the material, S , given by equation

$$S = \left. \frac{dP}{dh} \right|_{h=h_t} = \alpha m (h - h_r)^{m-1} \quad (2.6)$$

which was found by taking the displacement derivative of Equation (2.5) and evaluating it at maximum displacement, $h=h_t$.

From the stiffness, maximum force, and maximum depth, the contact depth, h_p , was calculated from equation

$$h_p = h_t - \frac{3P_t}{4S} \quad (2.7)$$

where P_t is the maximum force. The maximum depth used was from parsing the data (as opposed to extrapolation from Equation (2.5)). The contact depth represents the length of the indenter tip that is in contact with the sample material. However, because the material “piled-up” around the indenter tip, the contact depth from the Oliver-Pharr method did not accurately represent the tip-sample contact. This was corrected by calculating the pile-up height, h_{pu} , and adding this value to the contact depth. The methodology for

calculating the pile-up height is discussed further in Section 2.2.2.3. The contact depth (with pile-up included) was then used to calculate the projected contact area. The contact area as a function of contact depth was calibrated on a known reference standard. Further details of the contact area calibration are given in Section 2.2.2.1.

All data fitting was accomplished using *nlinfit* tool in Matlab®, except for the linear fit for the machine compliance calibration. The linear fit was found from a least squares program written in Matlab code based on the method described in reference [57].

Finally, the contact modulus and hardness can be determined with knowledge of the contact area, the contact stiffness, and the maximum force. The hardness, H , is given as

$$H = \frac{P_t}{A_c} \quad (2.8)$$

The contact modulus, E^* , (a function of both the tip and sample properties) is given by

$$E^* = \frac{S\sqrt{\pi}}{2\beta\sqrt{A_c}} \quad (2.9)$$

When calculating the contact modulus, the shape parameter, β , was set as 1 for a conospherical tip. From the contact modulus, the plane strain (or reduced) modulus can be calculated for the sample, as below,

$$\frac{1}{E^*} = \frac{1 - \nu_i^2}{E_i} + \frac{1 - \nu_s^2}{E_s} \quad (2.10)$$

where E and ν refer to the Young's modulus and Poisson's ratio, respectively, and the subscripts "i" and "s" refer to the tip and sample, respectively. Equation (2.10) can be rearranged to solve for the plane strain modulus of the material, E_{ps} , so that

$$E_{ps} = \left(\frac{1}{E^*} - \frac{1 - \nu_i^2}{E_i} \right)^{-1} \quad (2.11)$$

It is important to note that E_{ps} is a function of both the substrate and film properties when the indentation depth is more than 10% of the film thickness. The substrate and film properties can be isolated by using the King model, which uses weighted contributions from the tip, film and substrate, so that

$$\frac{S}{S_0} = \frac{\frac{1 - \nu_s^2}{E_s} + \frac{1 - \nu_i^2}{E_i}}{\frac{1 - \nu_f^2}{E_f} \left(1 - e^{-\frac{\alpha t}{a}} \right) + \frac{1 - \nu_s^2}{E_s} e^{-\frac{\alpha t}{a}} + \frac{1 - \nu_i^2}{E_i}} \quad (2.12)$$

where the subscripts “f”, “s”, and “i” refer to the film, substrate, and tip properties, a is the contact radius, t is the film thickness, α is a parameter based on tip geometry and a/t ratios, and S_0 is a normalizing parameter given by

$$S_0 = \beta E^* \sqrt{A_c} \quad (2.13)$$

where the β term is a geometric correction factor, and is equal to 1.129 for a circular punch. By solving Equation (2.12) for $(1 - \nu_f^2)/E_f$, the film independent properties can be determined. The parameter α is not available for a/t ratios larger than 4, which limits the applicability for the Ru and Pt coatings.

2.2.2.1. Area function correction

The contact area A_c as a function of the plastic (or contact), h_p , was calibrated through a series of indents with maximum target displacements ranging from 10 to 300

nm in 10 nm increments and at 5, 7, and 15 nm on Corning C1737F glass, where the reduced elastic modulus of 74.5 GPa was a well-known parameter [58]. Ten indents were performed at each maximum target displacement, where a displacement-controlled mode was used to move the indenter tip to the maximum displacement at a constant loading rate of 10 nm/s, hold it at the maximum displacement for 10 s, and then unload it at the same constant rate as during loading. The indents were placed on a 17 μm square grid, to ensure that the spacing between indents was greater than ten times the lateral extent of the largest indent. The additional indents performed at the shallow indentation depths were to ensure good fitting of the parameters even to extremely small depths. This will accommodate the shallow testing performed on the Au film and Ru and Pt coatings. Since the reduced modulus of Corning C1737F glass was well-known, the relationship in Equation (2.9) was inverted to solve for the contact area. The contact area was then be related to the plastic (or contact) indentation depth, h_p , which was defined as the vertical height of the indenter tip that was in contact with the sample at the start of unloading. The relationship between contact area and contact depth was fitted to the form:

$$A_c = C_0 h_p^2 + C_1 h_p + C_2 h_p^{1/2} + C_3 h_p^{1/4} + C_4 h_p^{1/8} + C_5 h_p^{1/16} \quad (2.14)$$

where C_i were the area function coefficients. Matlab's $\text{\textcircled{R}}$ *nlinfit* was used to fit the above equation.

2.2.2.2. Compliance correction

The raw data were also corrected for machine compliance, C_m , which was determined from the same tests on C1737F used to determine the area function. The

machine compliance was set as the y-axis intercept of the linear fit to the plot of $1/S$ versus $1/h_p^{1/2}$:

$$\frac{1}{S} = \frac{b}{\sqrt{h_p}} + C_m \quad (2.15)$$

where b was a fitting parameter. The y-axis intercept was found using a least squares method (as in [57]) to fit a linear line of the contact depth versus stiffness. Only contact depths greater than 50 nm were used to prevent larger scatter in the data at lower indentation depths from acting like a lever on the linear fit. Once the y-intercept was obtained, the raw displacement was then adjusted for the new compliance by changing the displacement with the following relationship

$$h' = h - C_m P \quad (2.16)$$

where h' was the corrected displacement, h was the raw displacement and P was the raw force. The area function calibration was performed again with the new displacement values. This data was again calibrated for machine compliance. This process was repeated iteratively until the changes in the machine compliance from iteration to iteration were less than 0.01 nm/mN, which is less than 0.5% of the total machine compliance of 2.47 nm/mN. The total machine compliance was taken as the summation of the iterated machine compliances, and the area function was taken as the values obtained when the raw displacement data is corrected by the total machine compliance.

2.2.2.3. *Pile-up correction*

The Oliver-Pharr method is very useful for describing systems where the material around the indenter tip “sinks-in”. However, it cannot accurately determine the contact area when the material around the indenter tip “piles-up” due to plastic flow [59]. In order to obtain accurate material properties, the pile-up height must be included in the plastic indentation depth, especially for deeper indents. To determine the pile-up height, h_{pu} , the *in-situ* image obtained immediately after an indentation test was used. First, the image was flattened using the *plane correction* tool in Scanning Probe Image Processor (SPIP) software (Image Metrology A/S, Denmark) where a 3rd order polynomial fit was used over the entire image, and the bearing height was set as zero. A Matlab computer program was written to find the minimum point on the image, and then search for maxima by parsing outwards from the minimum point along eight evenly spaced radii using Matlab’s *min* and *max* functions. A schematic of the parsing process is shown in Figure 2.9. These maxima along with the maxima from each of the indent images for the same test conditions were averaged to determine the pile-up height. Average pile-up heights for each indentation condition that were smaller than the surface roughness (as determined from the average of the pre-indentation tests *in-situ* images) nm were discarded. This ensured that all pile-up heights captured were indicative of pile-up and not of the material's surface roughness. While the blunt tip has poor lateral resolution, the height information was found to be accurate [60].

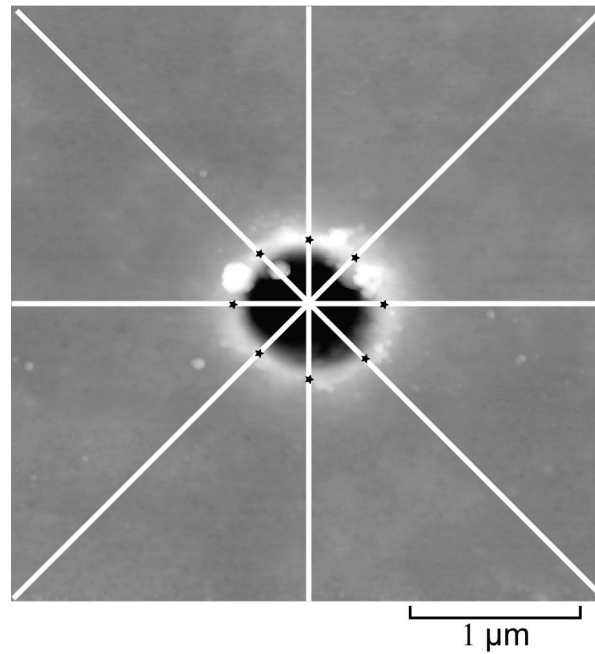


Figure 2.9: Schematic of parsing algorithm, where minima is found first, and then maxima (shown as black stars in image) are found along 8 directions.

2.3. Electrical Contact Resistance Measurements

Ohmic contact switch loading was simulated experimentally using a custom built electrically coupled indenter. The equipment was custom built from an Instron 5848 MicroTester and various Keithley electronic characterization components. The details of the experimental methods, including the equipment assembly and testing methodology, are given in Section 2.3.1. The analytical methods for evaluating the resistance as a function of force and contact area are described in Section 2.3.2.

2.3.1. Experimental Methods

To perform the electrical contact resistance measurements, an Instron 5848 MicroTester was used as a load frame for the electrical contact resistance measurements. The MicroTester has a position resolution of 20 nm, and is actuated using a brushless servomotor. The position is measured with a linear encoder on the piston actuator assembly. To measure force, a commercially available Honeywell Mid 31 load cell with a 1000 g maximum force scale was used. The load cell had a resolution of 1 mN. A tip assembly was attached to the Honeywell load cell, as shown in Figure 2.10. Between the tip and the load cell, a Macor insulating adapter was used to filter out any electrical signals from the load cell or the Instron load frame. A 0.5” radius hemispherical stainless steel tip polished up to 0.3 μm with alumina grit was attached to the Macor adapter. In some of the tests, a 200 nm thick Au film was deposited on the stainless steel tip to simulate symmetrical contacts.

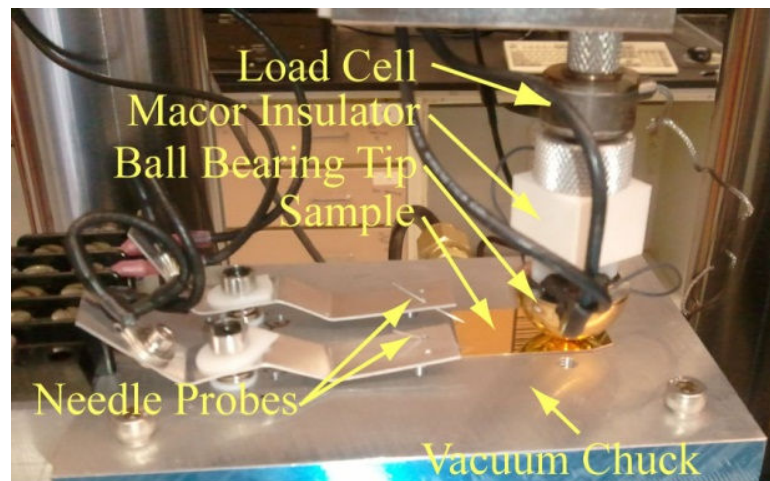


Figure 2.10: Image of testing apparatus.

To make electrical connections, two copper pads were glued with a two-part epoxy (Fast-set Double/Bubble®, Hardman®, South Bend, In.) to the outside edge of the tip. Aluminum wire bonds were then made from the copper pads to a region approximately 2-3 mm away from the center (contact point) of the tip. Current was sourced through one of the copper pads and its associated wire bonds, while voltage was measured through the second copper pad and its wire bonds. Prior to adhesion to the tip, an aluminum stranded wire was soldered to each copper pad. By soldering the wire prior to placement, the tip was free from contamination from the solder flux. For strain relief, the stranded aluminum wires were attached to longer wires with ring terminals on the flat side of the hemispherical tip using nylon washers and fasteners to electrically isolate the connection. These longer wires were twisted around each other to reduce electromagnetic forces from induction coupling that could cause errors in the resistance measurement. Again, to reduce strain in the wires which can affect low voltage measurements, the wires were secured to a bracket located above load cell. From there, the wires were connected to a terminal block, where one side was the wire from the tip, and the wire on the other side went to the electrical sourcing and measuring equipment.

The sample was held in place via a self-built aluminum alloy custom vacuum chuck. The vacuum chuck was mounted on a 2-axis stage with 10 μm resolution in X and Y. Tungsten needle probes, with a 2 μm tip radius, made electrical contact to the sample. The current was sourced through the one probe, while the voltage was measured through the other. The probe placement was not controlled, but the probes were placed approximately 3-4 mm away from the edge of the samples, and approximately 30-40 mm

away from each other. The tungsten probes were mounted in a hole through an aluminum microscope stage clip, which provided sufficient spring force for a reliable, repeatable electrical contact. The microscope stage clips were electrically isolated from the vacuum stage. Aluminum stranded wires were attached to the opposite end of the stage clips, which were routed through a terminal block. On the opposite side of the terminal, wires connected to the electrical sourcing and measuring equipment.

To source current, a Keithley 2400 SourceMeter was used. The sourced current was also measured with the Keithley 2400 SourceMeter to ensure accuracy. The current was sourced from -10 mA to 10 mA in 21 steps. A 100 μ A delta was applied to the stepped ladder, as shown in Figure 2.11. By applying the modified stepped ladder, differential conduction measurements were performed where effects from thermal drift were minimized (See Section 2.3.2 for more information on differential conduction methods). The 10 mA range was used, with 500 nA resolution, and 0.045%+2 μ A (so when sourcing 10 mA, the accuracy is 6.5 μ A). The voltage was measured using a Keithley 2182a Nanovoltmeter. Either the 10 or 100 mV measurement ranges were used. The 10 mV measurement range had a 1 nV resolution with 0.002%+40 nV accuracy (so for a 10 mV measurement, the accuracy is 240 nV). The 100 mV measurement range had a 10 nV resolution with 0.001%+300 nV (so for a 100 mV measurement, the accuracy is 1.3 μ V). Internal calibrations for the 2182a were performed whenever the temperature shifted by more than 1°C. Both the 2400 SourceMeter and the 2182a Nanovoltmeter had the filtering turned off, and 0.05 power line conversions to increase measurement speed. A study performed on 1 Ω resistor showed that the accuracy was not affected by the measurement speed.

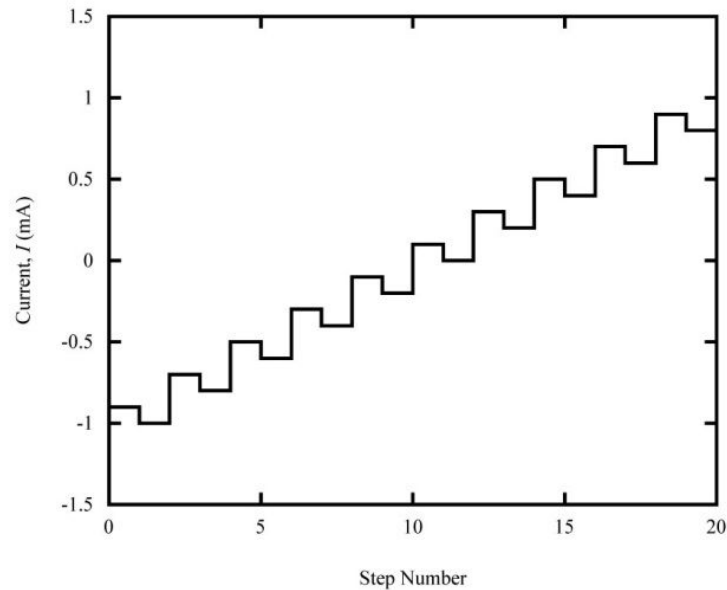


Figure 2.11: Current command from -1 to 1 mA with 100 μ A delta.

For the tests, the tip was first placed in contact with the sample. A preload force of 0.05 N was used to sense the surface. Once in contact, the tip was forced into the sample at 0.002 N/s to a maximum relative force of 0.5 N (so 0.5 N greater than the preload). The maximum force was held for 10 s before the tip was removed from the sample at a rate of 0.002 N/s. Every 0.05 N, current was swept in 21 steps from -10 mA to 10 mA with a 100 μ A delta while voltage was measured (Figure 2.12). LabView programs were generated to control communication between the Instron and the two Keithley systems. The loading rate was chosen to minimize the change in force (and thus displacement and contact radius) over the course of the each current sweep. During the test, 19 current sweeps were performed. Ten tests were performed on each sample, with indents spaced 0.5 mm apart to ensure no interaction between indents.

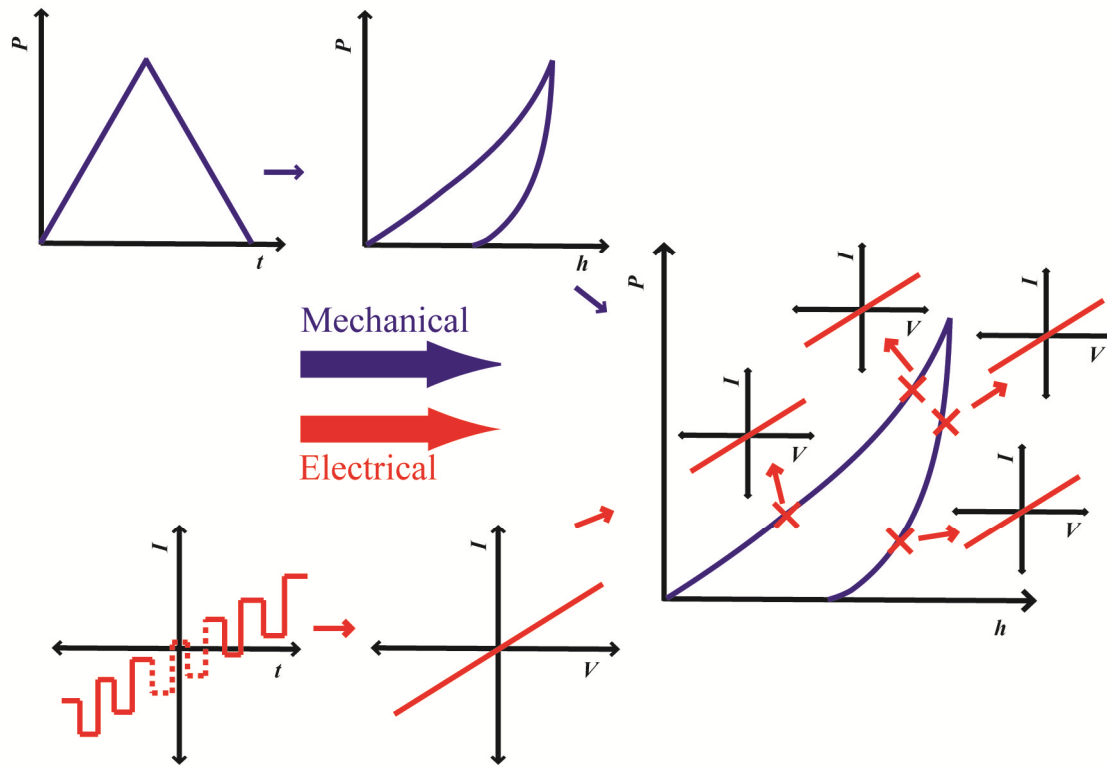


Figure 2.12: Schematic of electrical contact resistance measurement technique, showing how the electrical behavior was monitored throughout an indentation test.

2.3.2. Analytical Methods

To calculate the resistance, two different methods were used. The first calculated the resistance, R , as the slope of the voltage, V , versus current, I , plot, since Ohm's law states that

$$V = IR. \quad (2.17)$$

The modified step ladder current sourcing also allows the differential resistance, dR , to be calculated. Per the Keithley white paper [61],

$$dV_i = \frac{V_i - 2V_{i+1} + V_{i+2}}{4} \cdot (-1)^{i-1} \quad (2.18)$$

$$dR_i = \frac{dV_i}{dI} \quad (2.19)$$

where dV_i is the differential voltage for each inspection window (starting with $i=1$), V_i , V_{i+1} , and V_{i+2} are the voltage measurements at the respective i^{th} step, and dI is the differential current (in this case the applied delta current). The differential resistances can then be averaged for each current sweep to provide one differential resistance value for each force step. The differential resistance technique allows for the cancellation of thermal drift effects in the measurements, providing a more accurate resistance measurement. However, we have noted that there is less than 0.1% difference between fitting a least squares linear line to the data and calculating the differential resistance. In this research, we will present the least squares fit as the measured resistance value.

Each resistance value was correlated to the force it was gathered at using a parsing script developed in Matlab. The process of calculating a contact radius for each force was more complex. The indentation depths could not be used due to the large machine compliance in the system. The machine compliance was not evaluated due to the layered nature of the sample, and in some cases, the tip. Instead, the Hertzian contact elastic solutions were used to link the force, P , to the contact area, a , so that

$$a = \left(\frac{3PR}{4E^*} \right)^{\frac{1}{3}} \quad (2.20)$$

where R is the tip radius, and E^* is the contact modulus, as given in Equation (2.10). The elastic behavior relationship between force and contact area was used in lieu of the more traditionally used hardness relationship where

$$a = \sqrt{\frac{\xi P}{\pi H}} \quad (2.21)$$

where H is the hardness and ξ is a parameter to describe the level of plastic deformation in the system. First, the deformation is largely elastic in the experiments detailed in this paper, making it difficult to determine ξ correctly. Secondly, with a layered system where the contact radius to film thickness ratio (a/t) is large, the deformation is largely controlled by the Si substrate. This makes H hard to predict for the layered systems, despite H being well known for each individual layer independently, as will be discussed in Chapter 3. When using Equation (2.20), the polycrystalline aggregate Young's modulus and Poisson's ratio for stainless steel will be used for the tip values, and the polycrystalline aggregate Young's modulus and Poisson's ratio for Si will be used for the sample values.

2.4. Adhesion and Scratch Testing

To explore stiction of the material, adhesion tests were performed by using peak-force tapping mode on a Bruker Dimension FastScan AFM. A Bruker PFTuna Pt/Ir coated Si tip on a Si_3N_4 cantilever was used. Prior to testing, both the deflection sensitivity and cantilever stiffness were calibrated. A $2 \times 2 \mu\text{m}$ scan was taken of each sample, recording the height, adhesion, and dissipation channels. All images had 512 samples/line with a 0.501 Hz sampling rate. To avoid damaging the tip while scanning, a maximum load of 750 pN was set. To verify information in the images, force-

displacement curves were recorded from a 10x10 grid (100 total locations) on each sample. Five force-displacement curves were acquired at each sample location.

To evaluate the force-displacement plots, the adhesive force, the separation distance, and the work of adhesion were measured. The adhesive force was set as the largest tensile force during unloading. Note that for these experiments, compressive forces are positive, and tensile forces are negative. The separation distance was the difference in height between 0 N and the maximum adhesive force. The work of adhesion is the area under the unloading portion of the curve

The mechanical behavior was examined using a Hysitron TriboIndenter (Hysitron, Inc., Minneapolis, MN) with a diamond Berkovich indenter tip. A previous study examined the indentation hardness of the coating systems, and details of those investigations are given in [62]. To evaluate wear, scratch testing was also performed on the samples. The scratch testing performed a 2 μm long scratch with a constant force of 100 μN , with a loading and unloading rate of 50 $\mu\text{N/s}$. A 4x4 μm scan of the scratched area was performed immediately after each scratch test by using the indenter tip as a profilometer stylus. A setpoint of 2 μN was used during imaging, and tests were performed to ensure that the *in-situ* scanning setpoint did not cause alter the scratch profile. Three scratches were performed on each sample. Each scan had 256 samples/line and a scanning rate of 1 Hz.

The adhesive behavior was evaluated by using peak-force tapping mode on a Bruker Dimension FastScan AFM. A Bruker PFTuna Pt/Ir coated Si tip on a Si_3N_4 cantilever was used. Prior to testing, both the deflection sensitivity and cantilever

stiffness were calibrated. A $2 \times 2 \mu\text{m}$ scan was taken of each sample, recording the height, adhesion, and dissipation channels. A $2 \times 1 \mu\text{m}$ image was also taken of similar samples that had been aged approximately 6 months. All images had 512 samples/line with a 0.501 Hz sampling rate. To verify information in the images, force-displacement curves were recorded at several locations on each sample. Each location sampled had 5 force-displacement curves. In both the imaging and force-displacement ramping modes, a setpoint (maximum force) of 750 pN.

Chapter 3

Softening under Membrane Contact Stress due to Ultra-thin Ru Coatings on Au films

The contents of this chapter have been submitted to the journal Materials Science and Engineering A under the title Softening under “Membrane Contact Stresses due to Ultra-thin Ru Coatings”. The author asks that the journal article be cited in lieu of this thesis.

3.1. Introduction

The role of a single ultra-thin (< 50 nm) ductile coating on ductile thin films and its effects on the contact elastic stiffness and hardness of the coated films is of interest for micro- and nano-electromechanical systems (MEMS and NEMS, respectively). However, there are no predictive models or experimental results detailing the deformation response when the indentation depth is on the order of the coating thickness or larger, and the coating does not fracture. Models of a single, relative thick film on a substrate suggest that there should be minimal plastic hardening and elastic stiffening of the system response [37, 39, 40, 42, 63]. In such cases the mechanical properties should be dominated by the substrate when the indentation depth is a significant fraction of the film [37, 39, 40, 42, 63]. King’s general solution captures how the film, substrate, and indenter elastic properties, control the elastic response of the system

$$\frac{S_0}{S} = \frac{\frac{1-\nu_s^2}{E_s} + \frac{1-\nu_i^2}{E_i}}{\frac{1-\nu_f^2}{E_f} [1 - \exp(-\alpha \cdot t/a)] + \frac{1-\nu_s^2}{E_s} \exp(-\alpha \cdot t/a) + \frac{1-\nu_i^2}{E_i}} \quad (3.1)$$

where the subscripts “f”, “s”, and “i” refer to the film, substrate, and indenter, respectively, t refers to the film thickness, a refers to the contact radius, S/S_0 is the unloading stiffness normalized by the substrate stiffness, and α is term dependent on tip geometry and contact radius to film thickness ratio, a/t [39]. However, King’s model cannot be applied to the case of a blunt indenter tips on an ultra-thin coating because values of α for a/t greater than 4 were not determined [39]. The applicability of this general solution is further limited by the development of substantial bending stresses in the film. This transition in behavior occurs because as the ratio of contact radius to film thickness, a/t , increases, the elastically stiffer film begins to act as a membrane [40].

When the contact radius and contact depth are large in comparison to the film thickness the coating behaves as a membrane and should stiffen the mechanical response [43-45]. The stiffening is controlled by the coating thickness, t , the contact radius, a , the indentation depth, h_p , and the residual stress in the membrane layer. However, it is not clear if the trends can be extended to the case where the coatings are ultra-thin (<50 nm) or to cases where $h_p > t$ or $a \gg t$ [43-45, 64] because of the large deflections of the membrane [44]. In addition to the problem of geometric nonlinearities, the applicability of the models may be limited because they assume that the membrane has little or no ductility (i.e., a ceramic).

Although models of indentation processes can include plastic deformation, the validity of the results is dictated by the details of the constitutive response of the system

and how strains are transferred across the layers. In this work we will establish the primary factors that these models should include by establishing how an ultra-thin noble metal coating system (Ru and Pt coatings on Au thin films) behaves. The Au-Ru system was chosen due to its lack of solid solution solubility and absence of ordered intermetallics, ensuring a pure layered system [54]. In contrast, the Pt system was chosen because it has a significant solid solubility with Au [54].

3.2. Experimental Methods

The films and coatings were fabricated by sputter deposition on a (100) oriented Si wafer. The Si wafer was first coated with a 20 nm thick Cr adhesion layer from a 99.95% pure Cr target. On top of the Cr adhesion layer, a 350 nm thick Au film was deposited at 2 mTorr at room temperature from a 99.99% pure Au target at $\sim 2 \text{ \AA/s}$. Scanning probe microscopy (SPM) of the film surface show periodic surface features that are less than 100 nm in diameter, suggesting that the film is nanograined as seen in Figure 3.1a. SPM images were taken with a Bruker Dimension FastScan atomic force microscope (AFM) in peak force tapping mode to measure the surface height. The coating roughness is similar (within 0.5 nm) to the underlying Au film, so we assume that the reliability of comparisons across the coatings systems will be limited by the quality of the uncoated Au response.

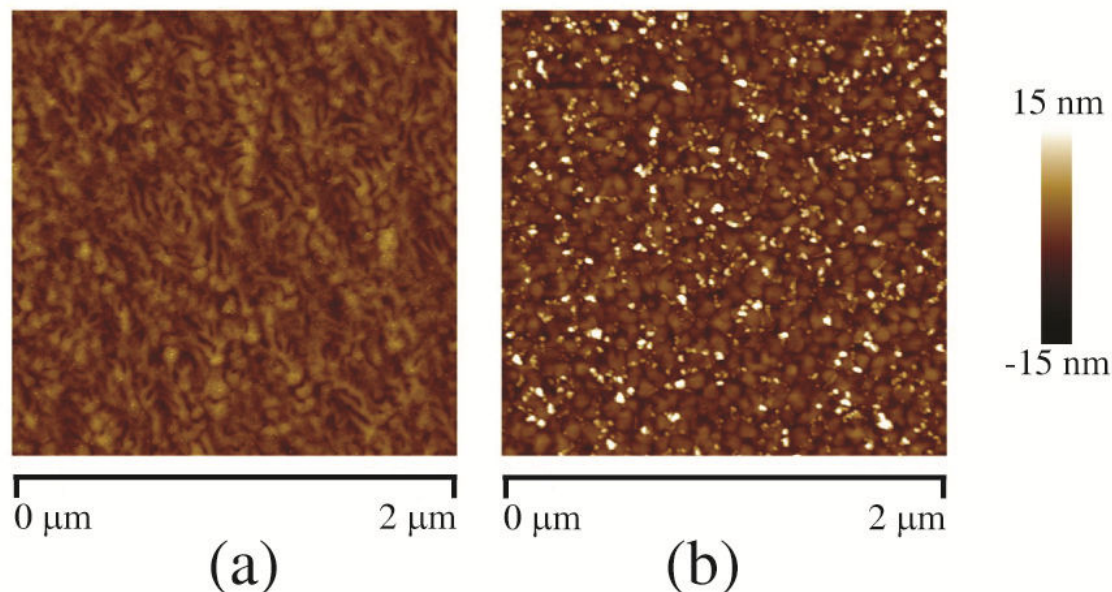


Figure 3.1: AFM image of a.) Au-only film showing ~ 100 nm features on surface and b.) Au film with 5 nm Ru coating with slightly larger surface roughness.

In order to further evaluate the grain size and orientation, 100 nm of Au was deposited on freshly cleaved rocksalt. The film was released from the rocksalt substrate by immersion in deionized water and was transferred to a transmission electron microscope (TEM) grid. A Phillips EM 420 TEM was used to evaluate the grain size and crystal structure of the film. The Au film showed small polycrystalline grains as seen in Figure 3.2 (5-30 nm), and a selected area diffraction pattern confirms the Au film is face-centered cubic (FCC). After deposition, wafer curvature measurements made using a Tencor FLX2330 revealed a small residual compressive stress (~ 80 MPa) in the Au film. After this initial analysis, the Au film and Si substrate were cleaved into several pieces. Each piece was then coated with an ultra-thin Ru layer of a different thickness. Sectioned pieces of films were sputtered at 2 mTorr with Ru coating thicknesses of 5, 10, 20, 50, and 100 nm. To examine the importance of residual stresses in the coating to the

mechanical response, a fourth sectioned piece of film was coated with 10 nm of Ru that was deposited at 5 mTorr to develop large compressive residual stresses [55]. To examine a material system that has similar crystal structure and lattice spacing as Au, 10, 50, and 100 nm thick Pt films were sputter deposited at 2 mTorr on separate sectioned Au films on Si substrates. Throughout this chapter, the Ru and Pt coatings sputtered at 2 mTorr onto the Au film will be referred to by the Ru or Pt coating thickness (i.e., 5 nm of Ru sputtered at 2 mTorr onto the 350 nm thick Au film will be referred to as the 5 nm Ru coating system). All of the Ru coatings were deposited from a 99.95% pure Ru target at $\sim 0.8 \text{ \AA/s}$ at room temperature, and all of the Pt coatings were deposited from a 99.99% pure Pt target at $\sim 0.8 \text{ \AA/s}$ at room temperature. Coating thickness was measured during deposition with a crystal monitor. All film/coating systems, including the Au-only film, were extremely smooth. AFM images were also taken of each film-coating system using a Veeco Dimension 3100 AFM. Each image had a $1.0 \text{ }\mu\text{m}$ scan length, 512 samples/line, and a 1.70 Hz scan rate. The images showed all coating-film systems had a root mean square (RMS) surface roughness less than 1.5 nm over a $1.0 \text{ by } 1.0 \text{ }\mu\text{m}$ scan area.

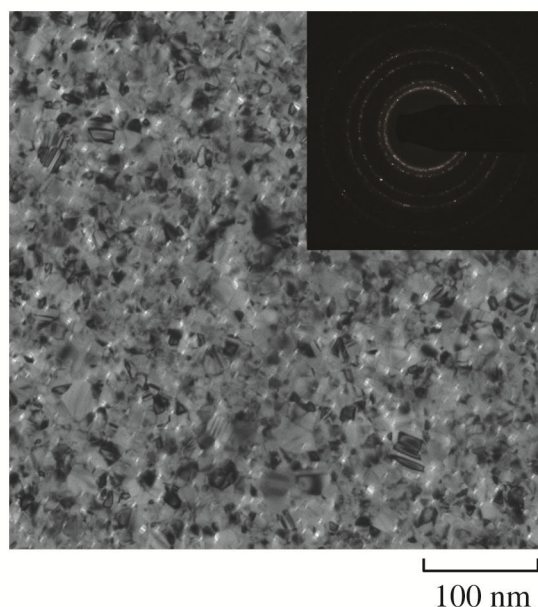


Figure 3.2: TEM image of 100 nm Au deposited on rocksalt showing small (5-30 nm) grains. Inset shows the associated selected area diffraction of the Au film.

Auger electron spectroscopy (AES) with a Physical Electronics 670 indicated that the Ru coatings were continuous on the surface of the Au film. A scan from 0 to 2800 eV of both the 5 and 10 nm Ru coatings showed no evidence of Au peaks, and only Ru, C, and O peaks were present. The absence of Au peaks is a strong indicator that even the 5 nm Ru coating is continuous on the Au surface. To determine if the ultra-thin coatings (<20 nm) were crystalline, 5 nm of Ru and 10 nm of Pt were deposited on TEM grids with 20 nm thick Si_3N_4 amorphous windows (from TEMwindows.com). Selected area diffraction (SAD) patterns of the Ru sample had diffuse rings that corresponded to the strongest diffracted hexagonal close packed (HCP) rings, associated with the (002), (110), (112), and (004) planes (Figure 3.3a). The Pt sample also had a diffraction ring pattern corresponding to those expected FCC materials (Figure 3.3b). TEM cross-sections

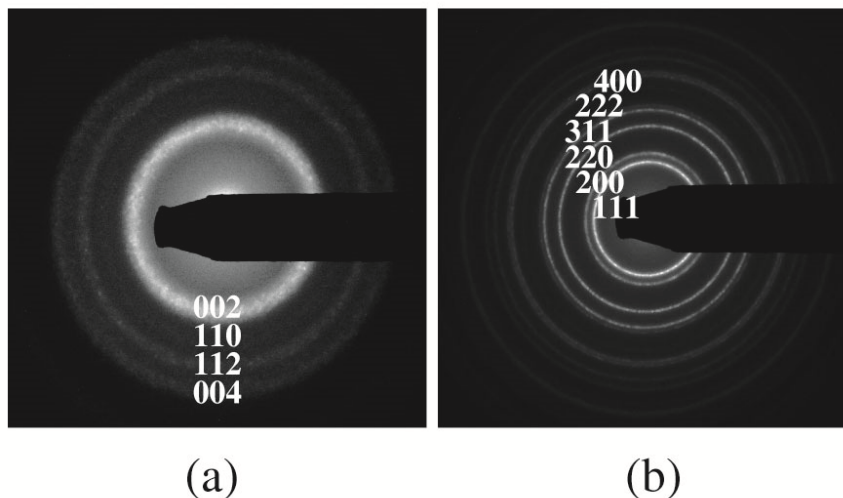


Figure 3.3: Selected area diffraction patterns of a.) 5 nm Ru coating and b.) 10 nm Pt coating on 20 nm thick amorphous Si_3N_4 windows. The Ru and Pt coatings, although thin, have crystalline diffraction patterns corresponding to HCP and FCC structures, respectively. The broad rings in the 5 nm Ru coating are likely due to very fine grain structure.

of a 5 nm Ru coating on the Au film also showed a continuous, conformal, polycrystalline coating (Figure 3.4). Further, although the surface roughness was slightly larger with the Ru coated samples, it was not an indication of island growth since the TEM cross-sections and AES show that even the thinnest Ru coatings are continuous. Thus, despite the ultra-thin nature of the coatings, the Ru and Pt layers were polycrystalline or nanocrystalline.

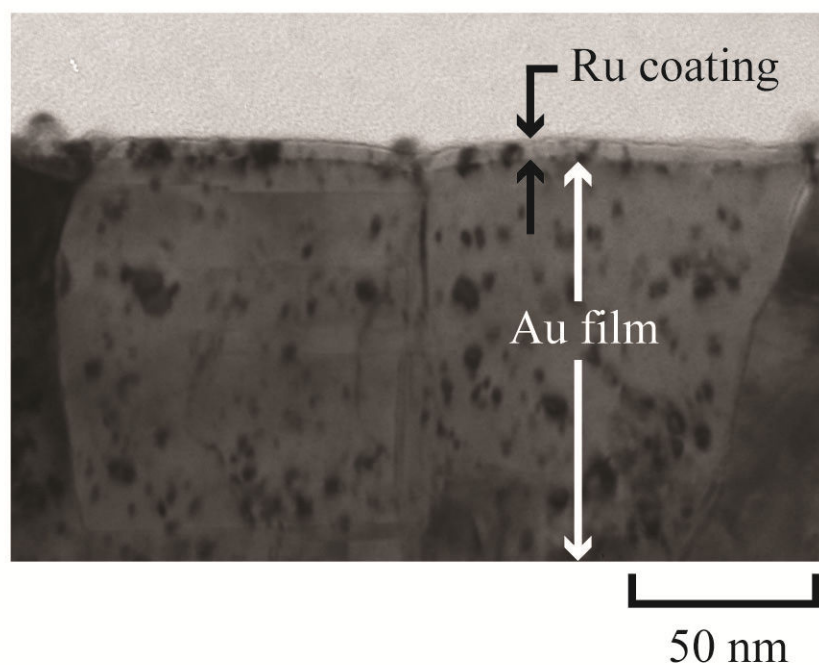


Figure 3.4: TEM image of Ru coated Au film cross-section.

The mechanical behavior was examined using a Hysitron TriboIndenter (Hysitron, Inc., Minneapolis, MN) with a conospherical, 500 nm radius diamond indenter tip. A force-controlled trapezoidal waveform was used (indents had a 100 $\mu\text{N/s}$ loading rate, a 10 s hold at a maximum force of 75, 300, or 600 μN , and a 100 $\mu\text{N/s}$ unloading rate). Ten indents were performed at each condition for each film. The 75 μN maximum indentation force produced indentation depths on the order of the Ru coating thickness. Although this indentation depth is very shallow, it is still approximately an order of magnitude larger than the surface roughness. The 300 and 600 μN maximum indentation forces were chosen to be approximately 10 and 20% of the Au film thickness. Before each indent, the drift rate was measured, and data were corrected assuming a constant drift rate. All drift rates were less than ± 0.1 nm/s, and the accumulated drift was less than 10% of the maximum indentation depth. Pre- and post-imaging of the indentation area

was performed with contact profilometry using the indenter tip as a stylus, with 1x1, 2x2 and 3x3 μm scan areas for the 75, 300, and 600 μN indents, respectively. Each scan had 256 samples/line and a sampling rate of 3 $\mu\text{m/s}$. The images were used to measure pile-up and verify that all indentation areas were free of debris and defects that could affect results. Traditional Oliver-Pharr analyses were performed on each indent per ISO 14577 [65-67] and in accordance with the methodology in reference [60] to measure the hardness, H , and plane strain elastic modulus, E_{ps} . The hardness is given by

$$H = \frac{P_{\text{max}}}{A_c} \quad (3.2)$$

where P_{max} is the maximum indentation force, and A_c is the projected contact area [59, 65-68]. The plane strain elastic modulus is given by

$$\frac{1}{E_{\text{ps}}} = \frac{1 - \nu_i^2}{E_i} - \frac{2}{S} \sqrt{\frac{A_c}{\pi}} = \frac{1 - \nu_s^2}{E_s} \quad (3.3)$$

where ν is the Poisson's ratio, E is Young's modulus, "i" and "s" refer to the indenter and sample, respectively, and $S=dP/dh$ is the initial unloading stiffness.

The contact area function of the indenter and machine compliance calibrations were also performed on a C1737F Corning down fusion drawn glass, and data were adjusted accordingly [65-67]. All Oliver-Pharr plastic indentation depths, h_p , were corrected to include pile-up heights, h_{pu} . In all cases, h_{pu} was greater than the surface roughness. One-way analysis of variation (ANOVA) tests were performed to statistically compare samples using Matlab built-in scripts "ANOVA1" and "MULTCOMPARE". All plots in this study include bars that represent the standard error associated with the 10 indents at the same condition. When error bars are not visible, the error is within the data

point. Trendlines shown on the plots are included to help visualize the data, and are not intended for data interpolation.

3.3. Results and Discussion

While we can argue that ultra-thin metal coatings should influence the earliest stages of deformation at contacts, it is not clear how effective they can be or if established modeling strategies can be used to predict their response. We will begin by establishing the baseline behavior of the Au film. Subsequent sections examine the effects of coating thickness and residual stress for noble coating systems that are insoluble and soluble in the underlying film (Ru and Pt, respectively).

3.3.1. Au Film Behavior

In order to understand the contribution of ultra-thin coatings to the deformation response, we must first examine the underlying Au film. By verifying the Au film elastic behavior matches that predicted from bulk polycrystalline aggregate elastic values, the phenomena noted when testing the coated systems can be confidently attributed to the coating, and not anomalous behavior of the underlying Au film. As expected, the elastic properties of the Au-only film (no coating) were very similar to those expected for bulk, polycrystalline aggregate Au (the Hashin-Shtrikman polycrystalline aggregate plane strain modulus is 99 GPa [69]). The standard error for 10 indents at the shallowest penetration depths was 2.8 GPa so the surface roughness (which should increase the

variability in the result, but not shift the hardness or plane strain modulus [32, 33]) is not a significant factor. At the shallowest contact depths (<5% of the total film thickness), the plane strain modulus for the Au film (no coating) was 91 GPa, less than 10% error (Figure 3.6). At deeper depths, the Si substrate can affect the measured elastic response. To remove the Si substrate and isolate the film-only properties, the King model in Equation (3.1) was applied. When the King model was applied to remove Si substrate effects at the deepest depths (largest contact radius), the King-model plane strain modulus was 93 GPa, approximately a 6% difference from the bulk polycrystalline aggregate model [40]. The plane strain modulus results suggested that the Au films were well behaved, ensuring that any interesting results in the coated films were due to the coatings and not from anomalous behavior of the underlying Au layer. With the baseline behavior of the Au-only films established, the influence of thin Ru coatings on the plastic and elastic deformation behavior of the composite were evaluated.

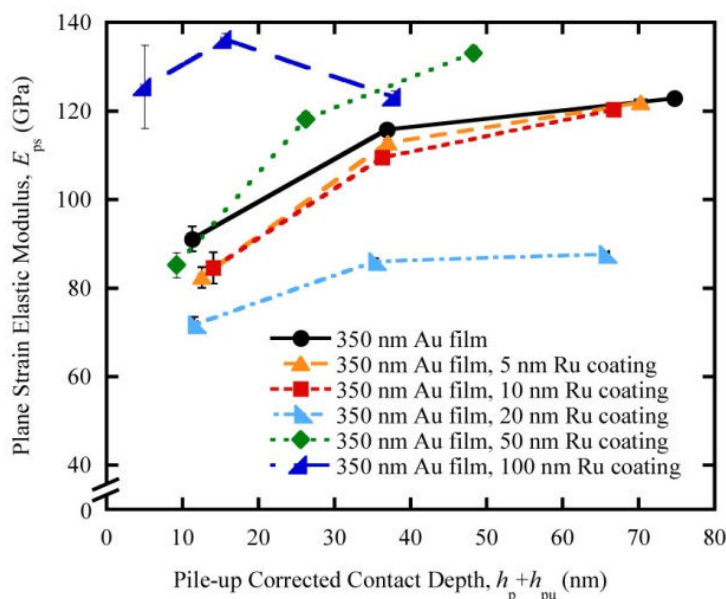


Figure 3.5: Plane strain elastic modulus vs. pile-up corrected contact depth. Data shown is for a 2mTorr, 350 nm thick Au-only film and 5, 10, and 20 nm thick Ru coatings sputtered at 2 mTorr on a 350 nm thick Au film sputtered at 2 mTorr. Lines are only shown to highlight trends and are not intended for interpolation.

3.3.2. Coating Thickness Effects on Deformation

Even though the single layers were exceptionally thin, when the 5, 10, and 20 nm thick Ru coatings were added to the Au film the hardness of the composite changed significantly. At the deepest depths, the hardness increased due to the Ru coatings. Additionally, as the coating thickness was increased, the hardness also increased (Figure 3.6). The largest increase in hardness occurred in the 20 nm thick Ru coating system, where the hardness was 3.26 ± 0.01 GPa, a 12% increase. In order to determine the statistical significance of this effect, an ANOVA test was run to compare the hardness of the different coating thicknesses (0, 5, 10, and 20 nm) at each contact depth. It is

interesting to note that the Ru coating still had a statistically significant effect on plasticity at the deepest depths (there were 3 degrees of freedom, df , a p-value, p , of 0.000, and an F-value, F , of 77.4), even though the indents were deeper than the Ru layer and significantly into the Au layer. Additionally, a multicomparison test found that the Au-only film was statistically different from each of the Ru coated films with a 95% confidence interval. This difference means that even at indentation depths that are up to 10 times the coating thicknesses, hardness is significantly affected. Force controlled indentation tests to 600 μN maximum force (where all other conditions the same as for the tests on the Au film and Ru coatings) on a Si (100) wafer had a hardness of ~ 11 GPa, which is much harder than the Au film. It is important to note that the increase in hardness is due to the Ru coating, and not an artifact of the Si substrate. Substrate effects are the strongest when the indentation depth is the largest fraction of the total film thickness. In the case of the Si substrate effects, the Au-only film should have the highest hardness, since it has the shallowest contact depth to film thickness ratio (the Ru coatings increase the total film thickness). Further, as the coating thickness is increased, the contact depth to film thickness ratio is decreased, and the hardening effects from the Si substrate should diminish. However, as the coating thickness increased, the hardness increased as well. Thus, the effect on hardness is not simply due to a larger Si substrate effect for the thinner Ru coatings.

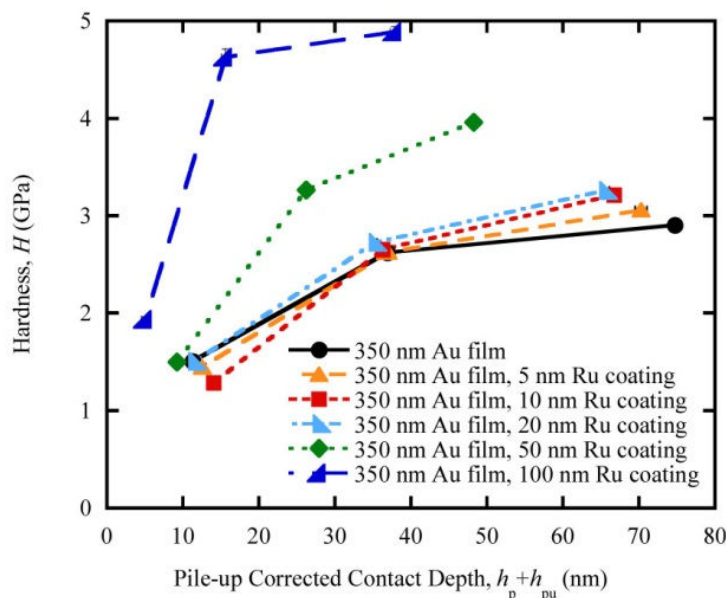


Figure 3.6: Hardness vs. pile-up corrected contact depth. Data shown is for a 2mTorr, 350 nm thick Au-only film and 5, 10, and 20 nm thick Ru coatings sputtered at 2 mTorr on a 350 nm thick Au film sputtered at 2 mTorr. Lines are only shown to highlight trends and are not intended for interpolation.

For a given coating thickness, hardness increased as contact depth increased. This finding was expected due to an increasing substrate effect at deeper depths (and contact depth to film thickness ratios) from the plastically harder Si wafer. While the thicker coatings exhibited increased hardness at the deepest contact depths, the coatings either had no effect or *reduced* the hardness at the shallowest depths (on the order of the coating thickness). At the shallowest depth, the Au-only film and the 20 nm thick Ru system coating had the highest hardness at 1.51 ± 0.03 GPa, while the 10 nm thick Ru coating system was the softest at 1.28 ± 0.02 GPa. At the deepest depths, one would expect the effect of the Ru coatings to be negligible due to indentation substrate theory, not statistically significant as this data shows. Further, since Ru films have been shown to have a much higher hardness than Au [70], one would expect any coating effect to

increase the hardness. Additionally, since there is a statistically significant effect at the deepest contact depths, one would expect a larger increase in hardness due to the Ru coatings at shallower depths where the substrate effects are less important.

Contradictorily, the hardness decreased due to Ru coatings at the shallowest indentation depths where the coating properties should have a significant effect. However, the contact radius to film thickness and contact depth to film thickness ratios are larger than the validity range for substrate theory. At indentation depths on the order of and much larger than the coating thickness, the ultra-thin coating had a statistically significant impact on the hardness of the system. Indentation membrane theory suggests that the hardness of an elastically stiffer membrane on a more compliant substrate should enhance the yielding of the system (yielding should start at an earlier applied load). The enhanced yielding is because the membrane increases the tensile stresses in the substrate [43]. Since the yield stress is directly related to the hardness due to the Tabor relationship, the tensile stresses induced in the substrate by the membrane should decrease the hardness of the system, as seen at the shallowest indentation depths. The increase in hardness with increasing Ru coating thickness at the deepest depths is not predicted by indentation membrane theory, and is interesting to note. Membrane theory for plastically hard, elastically stiff membranes on soft, compliant substrates usually assumes the membrane layer is a brittle ceramic that has negligible ductility. Previous studies examined indentation depths that were significantly larger than the membrane thickness and assumed fracture of the membrane, which reduced the membranes contribution to the deformation response [45]. However, this study shows that when the membrane can plastically deform, the hardness

significantly increases at indentation depths significantly deeper than the coating thickness.

The pile-up response (the material that is pushed above the surface of the sample being tested) is also different for Au-only film and the Ru coated systems, which further supports that there is a difference in the amount of plastic deformation due to the Ru coatings. *In-situ* contact profilometry images of the indentation area show that at the shallowest depths the amount of pile-up was minimal for both the Au-only film and the films with the Ru coating. Similarly, the differences between the Au-only film and Ru coatings were negligible (Figure 3.7). However, at the deepest depths the Au-only film had the largest amount of pile-up and was statistically different from the Ru coatings ($df=3$, $p=0.000$, $F=80.7$). A reduction in pile-up due to the presence of the Ru coatings is logical; according to indentation membrane theory, any plasticity occurring in the Ru layer should be due to bending and tensile stresses, and pile-up would not be expected under those loading conditions. Further, the difference in pile-up confirms the noted difference in hardness at the deepest depths is due to differences in yielding phenomena and is not an experimental artifact.

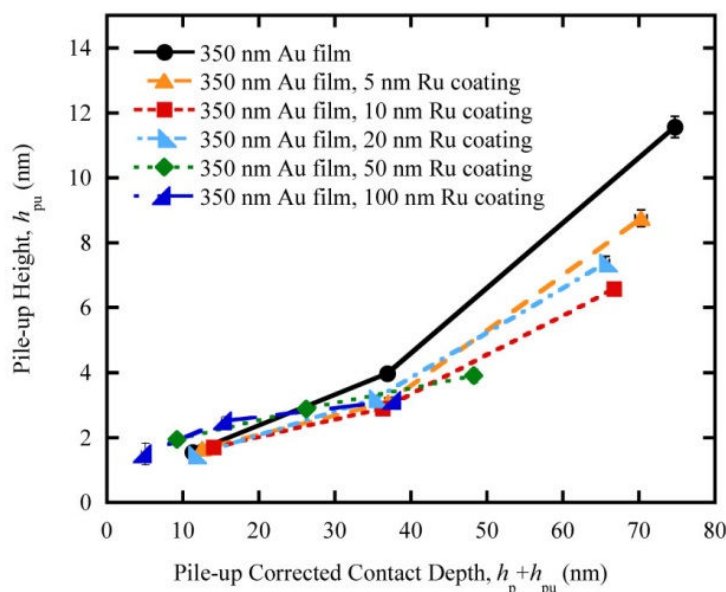


Figure 3.7: Pile-up height vs. pile-up corrected contact depth. Data shown is for a 2mTorr, 350 nm thick Au-only film and 5, 10, and 20 nm thick Ru coatings sputtered at 2 mTorr on a 350 nm thick Au film sputtered at 2 mTorr. Lines are only shown to highlight trends and are not intended for interpolation.

The importance of ultra-thin, ductile layers to the plastic deformation of the film surfaces is interesting, but we were particularly surprised by the effects of ultra-thin Ru layers on elastic deformation of the Au films. At the shallowest depths, the Au-only film had the highest plane strain modulus, and the modulus decreased significantly with increasing Ru coating thickness (Figure 3.5). This result was unexpected because the plane strain modulus of bulk, polycrystalline Ru is 492 GPa [69]. Substrate models predict that a more elastically stiff upper layer either has no effect on or increases the plane strain modulus of the composite system. Indentation membrane models also predict that the elastic-plastic loading behavior should be stiffened and the maximum indentation depth decreased in the membrane configuration [43, 45, 71]. However, membrane models have not examined the effect of a coating on the plain strain modulus. While the

unloading stiffness decreases due to the membrane, the displacement also decreases, so that it is unclear from the force-displacement curves what effect the coating has on the plane strain modulus [45]. Interestingly, E_{ps} of the Ru coated films were lower than any of the constituent layers. The effect was most severe for the 20 nm thick Ru coating system where the plane strain modulus was 72 ± 2 GPa, or 20% lower than the Au-only film. As the depth increased the other Ru coated films began to approach the Au-only film plane strain modulus. At the deepest depths, only the 20 nm thick Ru coating system was significantly different from the 0, 5, and 10 nm Ru coating-Au film systems (95% confidence interval), and its plane strain modulus was still 28% lower than the Au-only films. The (elastic-plastic) loading portions of the force-displacement ($P-h$) curves were very similar for all film and film/coating systems. However, the average slope of the (elastic) unloading portions of the $P-h$ curves for the 20 nm thick Ru coating system was lower than the other samples (39.4 ± 0.2 $\mu\text{N}/\text{nm}$ versus 56.9 ± 0.3 $\mu\text{N}/\text{nm}$ for the Au only film). A similar effect (i.e., a lower unloading stiffness for coated samples) was noted in experimental by McGurk and Page [45] for much thicker (≥ 350 nm) films. However, their coated samples also had a significant decrease in maximum depth (and therefore the contact depth) [45]. Since McGurk and Page do not report the plane strain modulus, it is unclear if the stiffness reduction that they observed was accompanied by a change in reduced modulus like our specimens. The enhanced effect on unloading stiffness for the 20 nm Ru coating may be due to a critical a/t or h/t ratio. It may also be due to the residual stress state in the coating and film being different for a 20 nm Ru coating than a 5 or 10 nm Ru coating. This study clarifies this question and demonstrates that an ultra-thin (Ru) coating can have a statistically significant effect at shallowest indentation

depths relative to the coating thickness. Moreover, the combined elastic response can more be compliant than either the underlying film (Au) or ultra-thin coating (Ru) on their own.

Two thicker Ru coatings were also examined: 50 and 100 nm. Like the thinner Ru coatings, the 50 nm Ru coating had a lower reduced modulus than the Au-only film at the shallowest indentation depth and a higher reduced modulus at the deeper indentation depths (Figure 3.5). While the thinner Ru coatings decreased the hardness at the shallowest indentation depth, the 50 nm Ru coating sample hardness at the shallowest indentation depth was the same as the Au-only film (1.5 GPa) (Figure 3.6). There was also significant hardening due to the (thicker) 50 nm Ru coating at deeper indentation depths. The 100 nm thick Ru coating had a different response. However, when the Ru coating was 100 nm thick the hardness was increased at all indentation depths in comparison to the Au-only film (Figure 3.6). Further, the plane strain elastic modulus *increased* at all indentation depths (Figure 3.5). It is interesting to note that as the indentation depth increases and becomes a larger fraction of the coating thickness, the plane strain modulus decreases. The reduction in the plane strain modulus is most likely due to the coating behaving more like a membrane as the deformation of the surface becomes more severe. It appears that the transition from contact stresses to membrane stresses appear around $h/t \approx 0.5$, which is consistent with the cutoff suggested by Vanimisetti and Narasimhan [43]. It is interesting that this cutoff can be applied even when the coating is ultra-thin and ductile.

There are a variety of phenomena that can influence the nanoindentation response of surfaces, and they must be carefully excluded as factors for our ultra-thin coated

specimens. For example, phase transformations can affect the hardness and plane strain modulus measurements [37]. However, phase transformations are unlikely because the P - h curve did not have discontinuities in the loading or unloading curve. Geometric effects such as pile-up around the indentation can also significantly influence hardness and reduced modulus measurements [26, 27]. We have accounted for pile-up in our study to eliminate this potential problem. The details of the surface geometry can also influence on hardness and plane strain modulus, but their impact should be negligible when indents are deep (relative to the size of the surface roughness). Because the difference in hardness between the 20 nm thick Ru coating and the Au film was largest at the deepest penetration depth, the interesting plastic and elastic deformation responses we observed cannot be attributed to the surface roughness of the system. The influence of “nanoscale” phenomena such as local residual stresses in the film are often more difficult to identify. If our processing conditions caused a local tensile residual stress, we would expect the loading curve to be much shallower due to the additional contraction as the distorted lattice released stored strain energy. We would also expect that this release would leave the unloading curve unaffected. The result would be a decrease in hardness due to the larger contact area under force-controlled loading conditions. The influence of a local tensile residuals stress on the plane strain modulus is less clear since both the unloading stiffness and contact area could increase. In contrast, a local compressive residual stress should have little effect on the elastic-plastic loading curve (perhaps only slightly increasing it). The resulting contact depth should be roughly the same and the hardness left unchanged. If large, local compressive residual stresses are relaxed by the loading process, a reduction in plane strain modulus could occur. Since the hardness, plane strain

modulus, and stiffness all decrease with increasing Ru coating thickness at the shallowest depths, a large, local compressive residual stress is a possible explanation for the effects of ultra-thin coatings that we have observed. Consistent with this hypothesis, the effect was less pronounced with increasing contact depth. It is known that the indentation stress field at an interface is affected by both the coating thickness and contact depth. This stress state will dictate both elastic behavior and the onset of yielding (which is directly correlated to hardness). As such, this work is important in understanding that ultra-thin coatings will affect the elastic behavior and yield point.

3.3.3. Tailoring of Mechanical Response through Residual Stress

Different residual stress states have been shown to affect the deformation behavior a homogeneous system [26, 27, 29]. Additionally, indentation membrane theory suggests that residual stresses should also affect the deformation behavior [43, 44]. According to Vanimisetti and Narasimhan, compressive residual stresses in the film cause increased tensile stresses in the substrate, and earlier onset of yielding than a film with no residual stress [43]. Different thickness coatings could lead to different residual stresses in the film. Experiments were performed to examine the role of surface residual stress and see if it correlates to the predicted membrane theory, even at contact depths equal to or much larger than the coating thickness. Two different sputtering pressures (2 mTorr and 5 mTorr) were used to prepare 10 nm Ru thick coatings. The 2 mTorr coating should have had higher compressive residual stresses than the 5 mTorr coating due to the more energetic impact of the sputtered atoms [55]. A larger compressive residual stress in

the top coating layer counterintuitively *decreases* the hardness, due to increased tensile stresses in the substrate [26, 27, 29, 43]. At the shallowest indentation depths, the 5 mTorr Ru coating (with lower compressive residual stresses) was 14% plastically softer than the 2 mTorr Ru coating, as predicted by the membrane theory. However, the 2 mTorr coating system (with larger suspected residual stresses) was 3% harder than the 5 mTorr coating (Figure 3.8) at the deepest depths. While the percent difference was small, a one-way ANOVA test found it to be statistically significant ($df=1$, $p=0.000$, $F=176.5$). This behavior at the deepest indentation depths may differ from membrane theory due to plastic deformation occurring in the membrane from the large tensile stresses. Previous studies and theories do not examine the case where the coating layer can have substantial amounts of plasticity, and do not extend to contact depths that are several times larger than the coating thickness. The statistically different mechanical response between the two sputtering pressures is an important finding because it demonstrates that not only do ultra-thin coatings have a significant effect on the mechanical response, but that their properties, such as residual stress, can be tailored to produce desired mechanical responses.

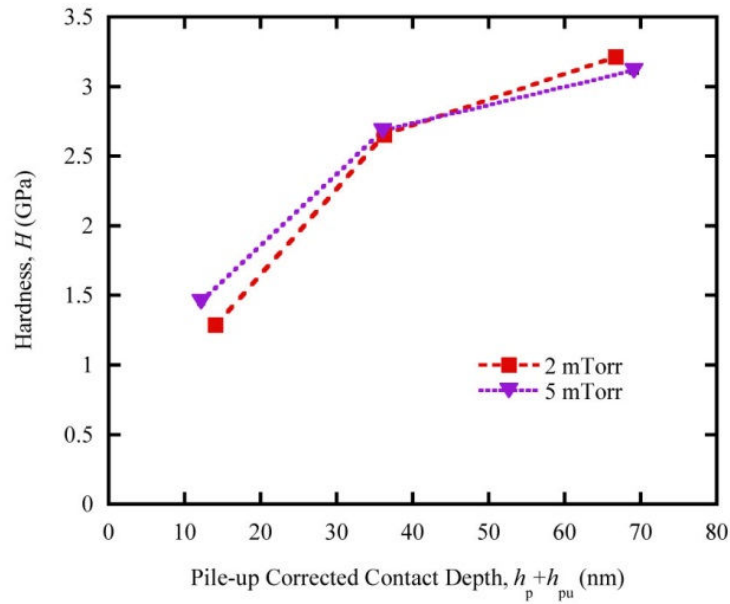


Figure 3.8: Hardness vs. pile-up corrected contact depth. Data is for 10 nm thick Ru coatings sputtered at 2 and 5 mTorr on a 350 nm thick Au film sputtered 2 mTorr. Lines are only shown to highlight trends and are not intended for interpolation.

Like the hardness response, the elastic deformation behavior is significantly affected by the different residual stress state in the Ru coating, again allowing for tailoring of deformation behavior by controlling the residual stress state of the material. While the trend in hardness due to coating thickness is similar to residual stress effects, the trends are not the same for the plane strain modulus. The residual stress effects on the plane strain modulus are much different than the coating thickness effect, again confirming that the deformation behavior in the Ru coating-Au film system is due to the membrane behavior and not experimental artifact. At the shallowest contact depth, which was on the order of the Ru coating thickness ($h_p \approx 10$ nm), the plane strain modulus of two conditions were statistically the same in a one-way ANOVA test ($df=1$, $p=0.958$,

$F=.0028$) (Figure 3.9). However, as depth increased, the difference in plane strain modulus between the two samples increased. At the deepest indentation depth, the plane strain modulus of the 2 mTorr sample (with suspected residual stresses) was 5% higher than that of the 5 mTorr sample. When comparing the results for different Ru coating thicknesses, the difference in the modulus was largely due to the unloading stiffness decreasing with increasing coating thickness. The unloading stiffness is the slope of the unloading curve at the start of unloading, while the plane strain modulus is a function of both the stiffness and the contact area. The difference in unloading stiffness between the Au-only film and the 20 nm Ru coating was largest at the deepest contact depth. However, the percent difference in stiffness between the 2 and 5 mTorr Ru coating samples was smallest at the deepest depths. Unlike the coating thickness trends, the changing stiffness did not account for the difference in the plane strain modulus at the different residual stress states. The difference in response between the different coating thicknesses and the different sputtering pressures verifies that the interesting deformation behavior noted in Figure 3.5 is due to the coating behaving as a membrane, and is not an experimental artifact. Additionally, since the elastic response changed based on residual stress state, the deformation behavior can be tailored by altering the thickness and the residual stress.

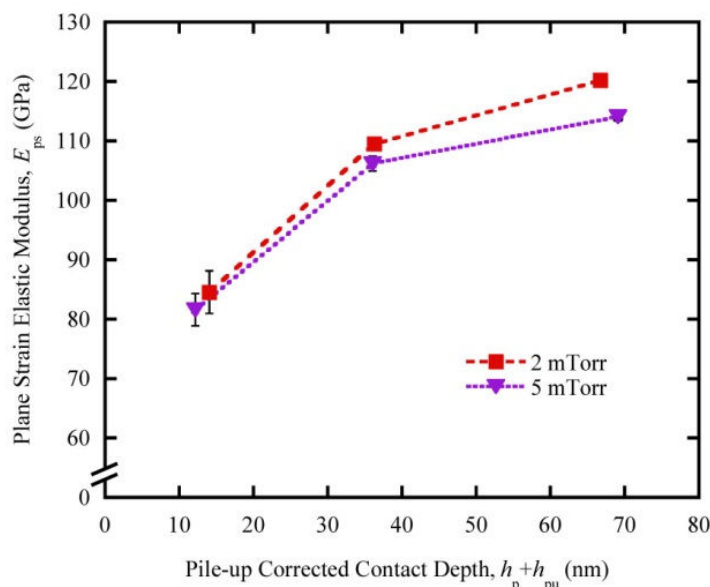


Figure 3.9: Plane strain elastic modulus vs. pile-up corrected contact depth. Data is for 10 nm thick Ru coatings sputtered at 2 and 5 mTorr on a 350 nm thick Au film sputtered 2 mTorr. Lines are only shown to highlight trends and are not intended for interpolation.

3.3.4. Corroboration of Results from Pt Coatings

Three different thicknesses of Pt coatings (10, 50, and 100 nm) were also examined to determine the influence of coating thickness on the contact deformation behavior of the underlying film. Although Pt less than half the elastic stiffness and hardness of Ru (for Pt, $E_{ps}=214$ GPa [69], $H\approx 6.6$ GPa [60]), the Pt is still plastically harder and elastically stiffer than the Au layer. The 50 and 100 nm thick Pt coatings had different deformation responses from their respective Ru coatings. The 50 nm Ru coating was both elastically stiffer and plastically harder than the 50 nm Pt coating, which might be expected based on the coating's bulk mechanical properties (Figure 3.10 and Figure 3.11). The 100 nm Ru coating was harder than the 100 nm Pt coating, again as expected

based on the mechanical properties for Ru and Pt. However, the 100 nm Pt coating was elastically stiffer than the 100 nm Ru coating (Figure 3.10). The increased plane strain modulus for the 100 nm Pt coating was unexpected because Ru is elastically stiffer than Pt. While it is unclear why the 100 nm Pt coating was elastically stiffer than the 100 nm Ru coating, it is important to note that the different material systems had a disparate response. The different response between the Pt and Ru coatings suggests that, for the thicker coatings, the mechanical properties of both the substrate and the coating are important for predicting the deformation response. Unlike the thicker coatings, the mechanical properties of the thinner coatings were not as important as the thicknesses of the coatings. When examining the 10 nm thick Pt coating, its reduced modulus and hardness behavior was very similar to the 10 nm thick Ru coating. At the two shallowest indentation depths, both the hardness and the reduced modulus for the Pt coating were statistically indistinguishable from the Ru coating (Figure 3.10 and Figure 3.11). This response suggests that when the indentation depths are deeper than the coating thickness, the coating thickness and underlying substrate properties are the most important parameter in controlling the deformation response.

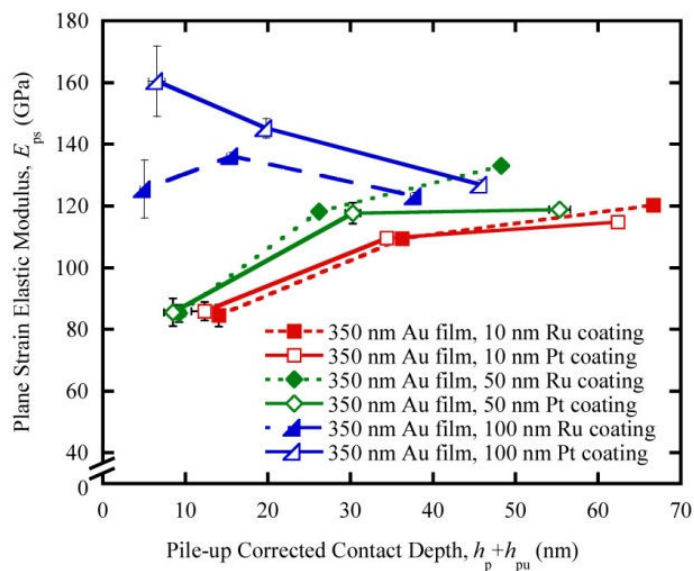


Figure 3.10: Plane strain modulus vs. pile-up corrected contact depth for 10, 50, and 100 nm thick Ru and Pt coatings deposited at 2 mTorr on a 350 nm thick Au film sputtered at 2 mTorr.

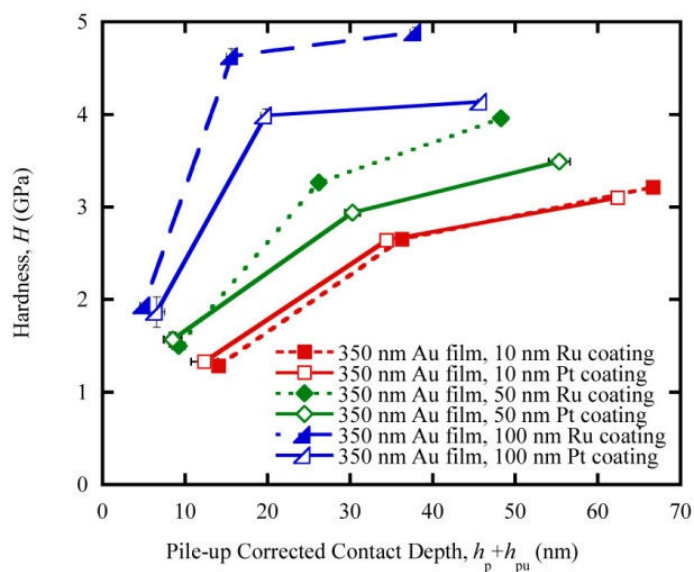


Figure 3.11: Hardness vs. pile-up corrected contact depth for 10, 50, and 100 nm thick Ru and Pt coatings deposited at 2 mTorr on a 350 nm thick Au film sputtered at 2 mTorr.

3.4. Conclusions

By adding an ultra-thin Ru coating to the Au film (even if the coating ≤ 20 nm), both the elastic and plastic properties were statistically significantly affected. The Ru layer served to increase the hardness of the material system at the deepest depths. However, at shallow penetration depths the trend inverted and the film-coating system response was plastically softer for thicker Ru coating systems. This softening at shallow depths is predicted in indentation membrane theory, and the deeper indentation depths may be due to plasticity occurring in the coating layer and changing the substrate stress state. In contrast, the elastic response of the different thickness Ru coating systems converged to the same hardness at the deepest contact depths, and the plane strain elastic moduli diverged for increasing depths under different residual stress. The Ru coating also had lower stiffnesses and reduced moduli than the Au-only film for films ≤ 20 nm. For 50 and 100 nm thicker films where the indentation depth was a smaller fraction of the film thickness, the hardness and reduced modulus was increased over the Au-only film. This difference from the thinner films is most likely due to decreasing membrane effects linked to decreasing h/t and a/t ratios. Also in agreement with indentation membrane theory, coatings with larger suspected residual stress (2 mTorr vs 5 mTorr sputtering pressure) had a decrease in hardness at the shallowest indentation depths, due to increasing tensile stresses in the Au substrate. Further, since the deformation behavior changed with residual stress state in the coating, we have confirmed that the mechanical response can be tailored by altering the stress state and the coating thickness to achieve a desired response.

Finally, the results for thinner Ru coatings were corroborated by tests on a 10 nm thick Pt coating on an Au film. At the shallowest indentation depths, the 10 nm Ru and Pt coatings were statistically indistinguishable. For the thicker coatings (50 and 100 nm), the Ru and Pt coatings had different mechanical responses from each other and the Au-only film. This response suggests that at ultra-thin coating thicknesses where the contact depth and radius are equal to or larger than the thickness, the response is dominated by the membrane stresses and the coating thickness. As the coating thickness becomes sufficiently thick so that $h/t < 0.5$, the membrane effect decreases, and the mechanical properties of the coating become more important in the overall deformation. This study shows that ultra-thin coatings have a meaningful effect on the mechanical response of a film system under contact loading. Additionally, by controlling properties of the ultra-thin coatings, such as residual stress and coating thickness, the mechanical response can be tailored to achieve a desired response.

Chapter 4

Reconciling Deformation, Contamination, and Geometry Contributions to the Resistance of Ohmic Contact Switches

The contents of this chapter have been submitted to the journal IEEE Transactions on Components, Packaging, and Manufacturing Technology under the title “Reconciling Deformation, Contamination, and Geometry Contributions to the Resistance of Ohmic Contact Switches”. The author asks that the journal article be cited in lieu of this thesis.

4.1. Introduction

Much effort has been put into evaluating contact resistance of materials used in radio frequency microelectromechanical systems or nanoelectromechanical systems (RF MEMS or NEMS) to ensure low power consumption. However, experimental results have greatly diverged from the predicted Holm’s law equation for a fully elastic contact, where

$$R_c = \frac{\rho}{4} \left(\frac{4E^*}{3PR} \right)^{\frac{1}{3}} \quad (4.1)$$

where R_c is the contact, or spreading, resistance, ρ is the average resistivity of the material, P is the force, R is the tip radius, and E^* is the contact plane strain modulus. E^* is given by

$$\frac{1}{E^*} = \frac{1 - \nu_i^2}{E_i} + \frac{1 - \nu_s^2}{E_s} \quad (4.2)$$

where E is the Young's modulus and ν is the Poisson's ratio, and the subscripts "i" and "s" refer to the tip and sample properties [6]. In fact, the measured resistances are several times, and often orders of magnitude, larger than the predicted spreading resistance in Holm's equation [3, 49, 53]. In some cases, the measure resistance was as high as 10Ω , while the predicted resistances for the contact geometry should be less than 0.05Ω [3, 49]. Further, experimental results show a surprising lack of dependence on contact force. Holm's equation predicts that the resistance should be proportional to the inverse of the contact radius [6]. Since the contact radius is proportional to the square root of the contact force, the contact resistance should also be proportional to the inverse square root of the contact force. However, some previous studies report contact resistances that have no, or extremely low, dependences on force [3, 49, 53, 72-78]. While the higher contact resistances and lack of dependence on force have been explained by various researchers as tunneling through adventitious carbon layers that quickly accumulate at the surface of metallic films [3, 10], ballistic transport through nanocontacts caused by surface roughness [49], or incorrect modeling of the contact area [2], we believe that the large contribution from thin film sheet resistance is responsible for high resistance values with a lack of force dependence. We will provide a simple model that describes the relative contributions to the total measured resistance, and will show that the model accurately describes experimental data. We will further show the difficulty in extracting contact resistances from the total resistance measurements due to the relative effects of sheet resistance and contact resistance, and suggest ideal testing parameters to extract contact resistances.

4.2. Methods

A 350 nm thick Au film was sputter deposited on a 20 nm Cr adhesion layer on a (100) oriented Si wafer with a native oxide layer. The film was deposited with an operating pressure of 2 mTorr and a 1.0 Å/s sputter rate to create a very smooth surface, with root mean square surface roughness, S_{RMS} , less than 1.5 nm as determined from an analysis of 1.0 x 1.0 μm atomic force microscope (AFM) scans with 512 points/line. To determine the film's microstructure, 100 nm thick films were deposited on freshly cleaved rocksalt with the same sputtering conditions. The rocksalt was then dissolved in deionized water, and the films were scooped onto a transmission electron microscope (TEM) grid. A Philips EM 420 transmission electron microscope showed that the Au film had extremely small, randomly oriented grains (5-30 nm). Wafer curvature measurements made with a Tencor FLX2330 showed that the film had a small compressive residual stress (~80 MPa). Four probe resistivity measurements performed with a Signatone probe and a Keithley 2400 Sourcemeater measured the resistivity of the Au film as 6.7 μΩ·cm. The high measured resistivity is most likely due to the small grain structure and small defects at the grain boundaries.

To perform contact resistance measurements, electrically coupled indentation tests with a 1" diameter stainless steel ball bearing tip were performed (Figure 4.1). The stainless steel tip was polished to reduce surface roughness, with the final defects less than 0.3 μm. An Instron 5848 Microtester was used to actuate the stainless steel tip into the sample and measure crosshead displacement, and a commercially available Honeywell 31 Mid 1000 g full scale load cell was used to measure force throughout the

test. A trapezoidal waveform in force control was used for the mechanical loading of the sample. The tests were loaded at a rate of 0.05 N/s to a maximum force of 0.5 N, and then unloaded at 0.05 N/s. Every 0.1 N, a Keithley 2400 SourceMeter swept current from -1 to 1 mA in 100 μ A steps with a 10 μ A alternating current applied to the linear staircase [61]. Voltage was measured at each current step using a Keithley 2182a Nanovoltmeter. A four-wire configuration was used to minimize any contribution to the measured resistance from the electrical leads. The resistance, R , was calculated as the least squares fit to the linear slope of the plot of voltage, V , versus current, I , for each electrical sweep. All the plots were linear (ohmic). The differential resistance, dR , was also calculated for three point windows, where

$$dR = \frac{\Delta V}{\Delta I} = \frac{V_1 + 2V_2 + V_3}{4\Delta I} \quad (4.3)$$

where ΔV and ΔI are the change in voltage and current, respectively. The change in current is the applied alternating current to the modified linear staircase. V_i are the voltages at the first, second, and third current steps. The differential conductance was then averaged for each force step. The resistances measured through the linear slope and the differential conduction methods were in very good agreement (less than 0.1% difference). Ten tests spaced 0.5 mm apart were performed on the Au film, and R found from the linear slope fit was then averaged and the standard error calculated for each sample at a given force.

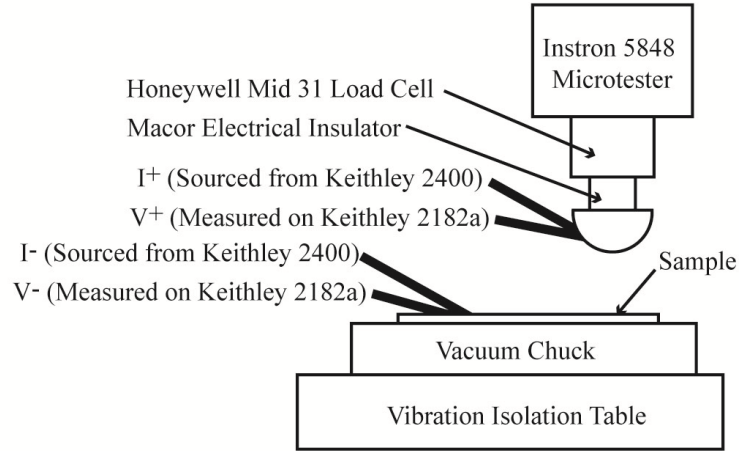


Figure 4.1: Schematic of experimental test setup.

After the indentation tests, the indentation area was examined using an optical microscope at 100 X magnification. No residual indents were found, suggesting that the indent was largely elastic. Due to the complexity of determining the hardness for a material that has limited, if any, plastic deformation, and has significant membrane effects, the Oliver-Pharr elastic solution was instead used. Assuming an ideal tip radius (a reasonable assumption from optical profilometry examination of the tip radius), the contact force, P , can be related to the contact area, a , by

$$P = \frac{4E^*a^3}{3R} \quad (4.4)$$

where E^* is the contact reduced modulus, and a function of both the tip and sample Young's modulus and Poisson's ratio [59]. Based on indentation membrane theory, which describes contact mechanics when the contact radius is larger than the film thickness, the reduced modulus used in the above equation should be that of the Si substrate, and not the Au layer [43-45, 62]. In this study, we used the contact reduced modulus of 95.2 GPa for Si contacting a stainless steel tip. If the Au reduced modulus

with a stainless steel tip (67.7 GPa) were used instead, the contact radii would be 12% larger.

4.3. Results

When we examined the resistance as a function of contact force, we saw a lack of dependence on force (Figure 4.2). A least squares approach was used to fit the data to a simple power law of the form $R=m \cdot P^q$, where m is the slope, and q is the power law exponent. The power law exponent, is only -0.05. This value is much lower than the power law exponent of -1/3 predicted from Holm's law (Equation (4.1)). Using resistivity measured from four-probe measurements ($6.7 \mu\Omega \cdot \text{cm}$), and E^* of 95.2 GPa, the predicted contact resistances from Holm's law would be expected to be in the $\mu\Omega$ to $\text{m}\Omega$ range for forces between 0.05 and 0.5 N and a tip radius of 25.4 μm (Figure 4.2). Instead, the predicted values are several orders of magnitude smaller than the actual measured resistances (0.5-0.6 Ω). The discrepancy between the measured and predicted contact resistances is true for our samples and for those in the literature, which report contact resistances from 0.2 to 1.5 Ω [3, 49, 53, 72-78] (note that the predicted value varies depending on contact force and hardness of the contact material, but all predicted values are in the $10 \mu\Omega$ to $100 \text{m}\Omega$ range). We do not believe that the high contact resistances can be explained by ballistic transport through a small number of asperity contact points. In fact, if this were the case, there could only be a single asperity that was 400 nm in size to explain the abnormally high contact resistances we measured. This size is several orders of magnitude smaller than the mechanically predicted contact radius of 17 μm .

While the contact area for actual devices may be hard to predict due to surface roughness and small contact forces, indentation tests with a sphere on a flat have shown that projected contact area is a good measure of the actual contact area based on correct calculations of plane strain moduli and hardness values [60]. Thus, the large measured resistances cannot be explained simply by an overestimation of the contact area.

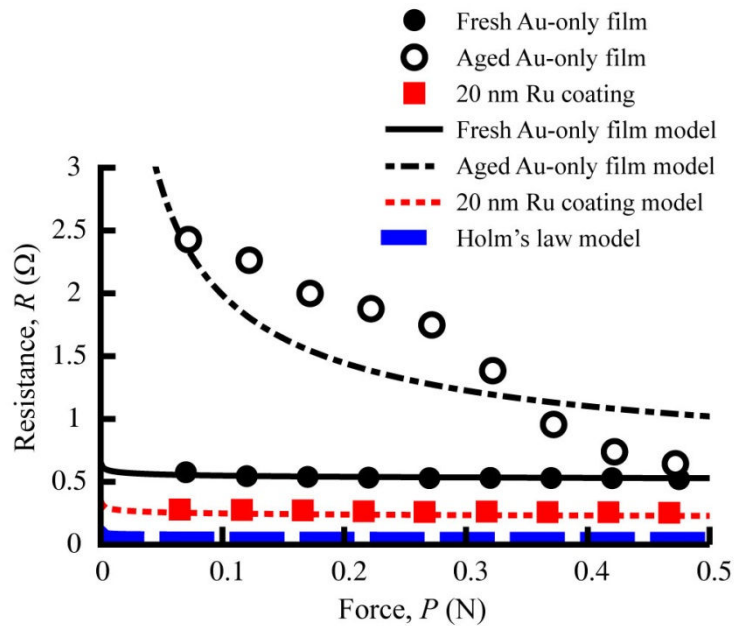


Figure 4.2: Measured and modeled resistances versus force.

We instead posit that the measured resistance is a sum of the contact resistance, contamination resistance, and voltage drops through the conducting tip and sample. Further, due to the thin film nature of the sample, the resistance in the sample is a significant fraction of the total resistance. A simplified model of the total resistance, R , can be written as

$$R = R_c + R_{\text{contamination}} + R_{\text{sample}} + R_{\text{tip}} \quad (4.5a)$$

$$R = \frac{\rho_{\text{tip}} + \rho_{\text{sample}}}{4a} + \frac{\rho_{\text{c,cont}}}{\pi a^2} + \frac{\rho_{\text{sample}}}{2\pi t} \ln\left(\frac{s_2 s_3}{s_4 a}\right) + \frac{\rho_{\text{tip}}}{2\pi} \left(\frac{1}{d_1} - \frac{1}{d_2} - \frac{1}{d_3} + \frac{1}{a}\right) \quad (\text{b})$$

$$R \propto C_0 P^{-\frac{1}{3}} + C_1 P^{-\frac{2}{3}} - C_2 \ln(P) \quad (\text{c})$$

where R_c is the contact (or spreading) resistance, $R_{\text{contamination}}$ is the resistance due to surface contamination, R_{sample} is the resistance in the sample, R_{tip} is the resistance in the tip, and C_0 , C_1 , and C_2 are constants. When we look at the definitions for the above terms, ρ_{tip} and ρ_{sample} are the resistivities of the tip and sample, respectively, $\rho_{\text{c,cont}}$ is the specific contact resistance for the contamination layer, t_{sample} and t_{tip} are the film thickness of the tip and sample, respectively, a is the contact radius, P is the applied force, s_i are the spacings between the probes on the sample, and d_i are the spacings between the probes on the tip. We acknowledge that there will be thermal effects as well for higher currents that are not accounted for in this model. However, for voltage biases up to 10 mV across the contact, the contact temperature should only be $\sim 6^\circ\text{C}$ above room temperature and well below the softening temperature [7, 50], and so thermal effects can be safely ignored for this discussion. To model the total resistance, we used the measured Au film resistivity from the four-point probe measurement ($6.7 \mu\Omega\cdot\text{cm}$) for ρ_{sample} . The plane strain modulus was calculated from literature elastic stiffness values (s_{ij}) for bulk silicon (141.9 GPa) [69]. For modeling purposes, we assumed values for ρ_{tip} of $720 \Omega\text{nm}$ (for bulk stainless steel [79]) and $\rho_{\text{c,cont}}$ of $0 \Omega\text{nm}^2$ (and assumed that initial contamination is negligible). Coarse measurements of probe/tip spacing helped to set the probe spacing parameters s_1 , s_2 , and s_3 to 15, 45, and 35 mm respectively, and d_1 , d_2 , and d_3 to 2, 4, and 4 mm, respectively. The model predicted in Equations (4.5a) fit the experimental data very well.

It should be noted that a correction factor of 0.325Ω was added to the predicted resistance from Equations (4.5a) to account for small delaminated areas of the Au film between the indents and the electrical probes from previous tests at larger forces. While the delamination was far enough away from the tested areas to not mechanically affect the test, it is very likely that the delamination increased the resistance. This resistance increase should be a linear offset to the force dependence of the data. When a constant of $R_0=0.325 \Omega$ was added to the resistance predicted from Equations (4.5a) to account for the delamination, the response effectively described the resistance versus contact radius response (Figure 4.2). Later, we will also show a layered system without delamination that fit the model in Equations (4.5a), without needing a correction factor.

The Au film mentioned above was also tested six days after the initial test, when both tip and sample had accumulated contamination. The tip was left installed on the equipment and was exposed to laboratory air, while the Au film was stored in a Fluoroware container. Due to the increased contamination on both the tip and Au film, the contact resistance increased, and the dependence on force also increased, as predicted when $\rho_{c, cont}$ increases with increasing thickness (Figure 4.2). The increased dependence on force further suggests that a tunneling mechanism caused by a contamination layer at the metallic film surface is not likely the cause of the large resistances. A contamination layer is also not the likely cause of the lack of their dependence on force in our prior measurements on fresh surfaces, because the dependence on force actually increases as the contamination layer increases. Again, $R_0=0.325 \Omega$ was added to the predicted resistance to account for the delamination, since the repeated tests were performed on the same film. The variation in the aged Au sample from the aged model has two likely

explanations. The first is that the contamination layer may fracture under loading, allowing for metal-metal contact in some areas, thus decreasing the measured resistance once the force becomes sufficient for fracture [80]. The second explanation is that the contamination layer may be compressed underneath the indenter tip, decreasing its thickness and resulting in a reduced resistance through the layer. Still, it is clear that with the addition of a contamination layer, the measured resistance has an increased dependence on force, as predicted from the model in Equations (4.5a).

Tests were also performed on 20 nm thick Ru coating deposited on the 350 nm Au film. The Ru layer was sputtered at a rate of 1.5 Å/s from a 99.95% pure Ru target at 2 mTorr operating pressure. The Ru coating was found to be continuous through Auger electron spectroscopy (AES) performed with a Physical Electronics 670. Both a survey scan from 50 to 2750 eV, and a finer scan from 1900 to 2400 eV, showed only Ru, C, and O peaks, with no evidence of surface Au peaks. AFM images of the surface using the Bruker AFM imaging parameters detailed above show that the surface roughness was not significantly increased by the presence of the Ru coating. Further details of the AES and AFM analysis can be found in [62]. Since the Ru-coated film did not have delaminated areas, the correction factor, R_0 , was set to 0.

When we examine the contact resistance versus force, we see a lack of dependence, like the Au tip on the Au film (Figure 4.2). Interestingly, the Ru-coated Au film contacted with a stainless steel tip actually has a *lower* contact resistance than the stainless steel tip on the Au film. If the measured resistance was dominated by the contact resistance, we would anticipate that the Ru coating should have a higher resistance because the interface between the Ru and Au layers should increase scattering of

electrons and therefore the resistance. However, since the measured resistance is dominated by the sheet resistance, a slight change in the probe placement actually decreases the measured resistance for the Ru-coated Au film. Again, the sheet resistance model accurately describes the measured resistance (Figure 4.2).

Unfortunately, when we attempted to fit the experimental results for three test sets described above to determine the coefficients independent of known parameters, instead of assuming them, we found that the parameters were not single-valued. The hardest parameter to effectively fit was the $P^{-1/3}$ term, which is the contact resistance term. When the relative contributions to the total resistance was examined, we can see that the contact resistance is most likely in the noise of the measured resistance when the tip radius is large and the probes are placed a significant distance away (Figure 4.2). Thus, trying to determine the contact resistance from measurements like those in this paper and in the literature [3, 49, 53, 72-78] is exceedingly difficult, if not impossible. Even when the films are as thick as 5 nm, the contact resistance will be several orders of magnitude smaller than the total measured resistance. Instead of comparing contact resistances, tests with a large contact radius and large probe spacing compare the relative sheet resistances of the different material systems.

The models in Equations (4.5a) provide a good fit to the experimental data when the contact resistance is a small function of the total measured resistance. However, it is important to note that we have used a simplified model for the constriction resistance, where film thickness effects on the constriction resistance have been ignored. An improved model for R_c can be found in works of Zhang, Lau, and Gilgenbach [52], of Timset [51], and Norberg, Dejanovic and Hesselbom [81]. These models account for the

thin film nature of the contact resistance, where R_c is represented as a complex polynomial function of the logarithm of contact radius to film thickness (a/t) ratio. However, these models are limited to a/t ratios of 100 for symmetric contacts and 10 for asymmetric contacts, and have not been developed to extend to a/t ratios that are seen in the experiment performed in this paper or those that occur in RF MEMS switches. Despite the restriction on the a/t ratios, if we extrapolate the advanced constriction resistance model in Zhang et al., to that from Holm's law for a symmetric contact ($\rho_1=\rho_2$), the Zhang model predicts contact resistances that are almost a factor of two larger than those predicted by Holm's law. It is important to note that despite the significant improvement of the film thickness constrictions resistance models, the increase in contact resistances over Holm's law predicted by the Zhang model is not enough to explain the large measured contact resistance without the inclusion of the sheet resistance.

In order to improve the deconvolution of the contact resistance from the total measured response, probe spacing needs to be minimized. Even in the case where the probes are placed 55 μm away from the center of the contact (and 2 μm away from the edge of the contact at a maximum force of 0.5 N), the total resistance will still be significantly affected by the sheet resistance through the film and the bulk resistance through the tip, and the spreading resistance will be a small fraction of the total resistance (Figure 4.3). Because the sheet resistance is small in this instance (due to the small s_i spacing), the contact resistance is a larger fraction of the total measured resistance. However, it is very difficult to place the probes this close to the contact in actual tests due to the large profile of a blunt indenter radius. While the contact resistance may be deconvoluted from the measured response when the probe spacing is small, it is

important to note that the existence of sheet resistance through the film will change the shape of the measured resistance versus force (or contact radius) plot, so that the data no longer fit Holm's law.

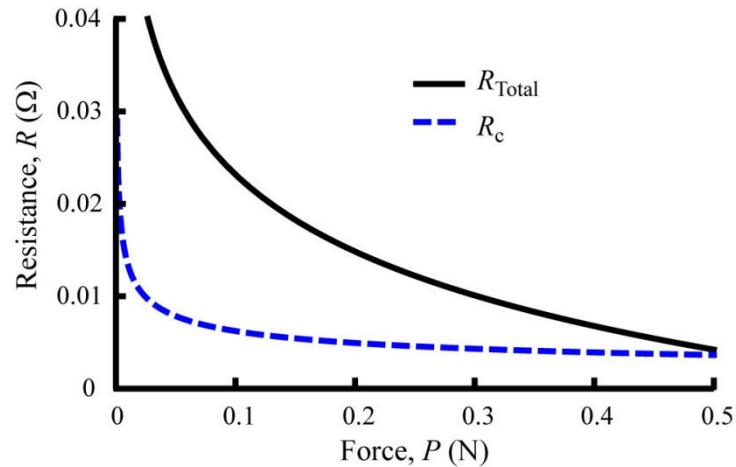


Figure 4.3: Total resistance and constriction resistance versus force when probes are placed $55 \mu\text{m}$ away from the center of the contact ($2 \mu\text{m}$ away from the edge of the contact at 0.5 N).

Another way to maximize the contact resistance contribution is to decrease the tip radius (and thus the contact radius), which increases the contact resistance. Increasing the contact resistance helps to deconvolute it from the total measured resistance, and enables comparisons of different material systems. This comparison is more important for optimization of nanoelectromechanical systems (NEMS) applications, where the contact resistance is a larger contributor to power consumption (because the contact radii are small). By increasing the contact resistance without increasing the other parameters, the relative contribution of the contact resistance can be increased. For example, when the tip radius is decreased to 30 nm (as in the case of a conductive AFM tip), the relative

contribution from the contact resistance is increased, as shown in Figure 4.4. In this scenario, we have used the Zhang model to predict the contact resistance, since we are well within acceptable a/t ratios. We have also decreased the spacing between the electrical probes and the contact area. All other parameters are kept the same. Both of the strategies, decreasing probe spacing and decreasing tip radius, help with fitting the contact resistance parameters.

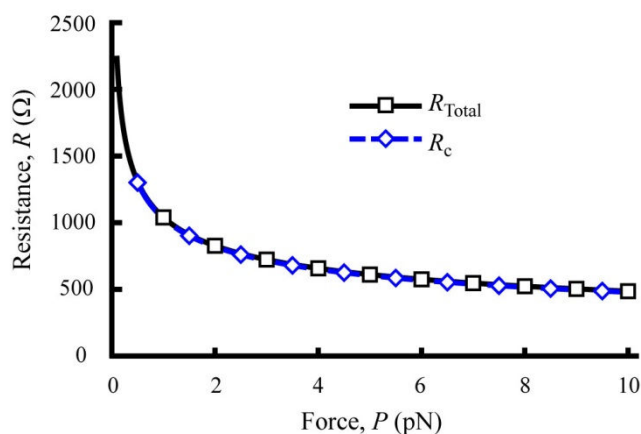


Figure 4.4: Relative contributions to the total contact resistance as a function of force for a modeled nano-scale contact (such as a conductive AFM tip). Points are added help identify the lines, and do not represent experimental points.

4.4. Conclusions

In summary, we have noted that the traditional method for prediction of measured contact resistances [3, 49, 53, 72-78] is flawed, because the previous studies do not account for the thin film sheet resistance, which can be large for thin films. The sheet resistance contribution explains the high contact resistances with low or no dependence on force that are noted in the literature and these experiments. To maximize the

contribution from the contact resistance, a four wire configuration should be used with the probes placed as close to the contact as possible, and the tip radius should be minimized. By following the above recommendations, the contact resistance can more effectively be analyzed in a sample and comparisons can be made between samples. This examination shows that to minimize power consumption in RF MEMS and NEMS, the transmission line between the contact areas and the source and drain should be as short as possible. To reduce power consumption, the sheet resistance of the materials used in devices should be minimized. Further, since the constriction resistance is a very small fraction of the power consumption in the devices, effort will be better spent on maximizing surface stability (i.e. minimizing adhesion and reducing arcing). Finally, because of the small contact radius, it is much more important to control constriction resistance for NEMS devices than MEMS.

Chapter 5

Impact of Ultra-thin Coatings on Stiction and Friction

Two of the failure mechanisms for RF MEMS ohmic contact switches are due to stiction and friction of the device. Au, one of the most frequently used material systems for the switches, has a low hardness, which increases damage due to wear [3, 82]. It has been noted that although Au is one of the best conductors, it is one of the worst materials in terms of stiction and reliability [7, 82]. However, the materials that have the best wear properties, such as Ru and Pt, have lower conduction. We believe there is a solution with layered materials, where the majority of the conduction is occurring in an underlying Au layer that has a low resistivity, while the top layer is harder to limit wear damage. In this chapter, we will present wear studies evaluating ultra-thin Ru and Pt coatings on Au films for their improvement in damage accumulation.

Because RF MEMS ohmic contact switches have a very small restoring force ($< 100 \mu\text{N}$), large adhesive forces can be a significant problem, and can cause the switch to fail closed. Various studies have examined the adhesive forces for a variety of material systems (Au, Ru, Pt, Rh, and Ni) [3, 7, 48]. However, the nature of the separation at the contact interface has not been examined for material systems other than Au. The type of separation is important because it has been linked to switch lifetimes [48]. Specifically, switches that underwent separation with material transfer and/or necking of the contact had the lowest lifecycles (10,000-70,000 cycles), followed by film delamination from the Si substrate (200,000-500,000), and separation at the original interface ($>10^6$ cycles) [48].

However, material transfer, necking and delamination during separation occur more frequently than separation along the original interface [48]. Fortini et al. used molecular dynamics (MD) simulations to explore contact separation in Au/Au and Ru/Ru contacts [17]. They found that the simulated Ru contacts had more brittle separation than the simulated Au contacts [17]. Since brittle separation is desired for device longevity, the MD study by Fortini et al. suggest that Ru contacts should be preferred to Au contacts for RF MEMS ohmic contact switches. However, MD simulations are limited by bonding assumptions and separation rates, and may not accurately describe actual separation. Further, Broué et al. have shown that asymmetric contact can have reduced adhesive forces, but have not examined the nature of the contact separation. To explore the nature of the contact separation, atomic force microscopy (AFM) was used to measure the adhesive force and degree of ductility in the contact separation for Au-only films and Au films with either ultra-thin Ru or Pt coatings.

Wear, or removal of surface material due to frictional forces, can also cause failure of ohmic contact switches [82]. Archard lists the wear rate, W , or removal of material per unit of sliding area as

$$W = \frac{KP}{3a} \quad (5.1)$$

where P is the force, a is the contact radius, and K is a constant based on the contact material [83]. The indentation hardness, H , can be described as

$$H = \frac{P}{\pi a^2} \quad (5.2)$$

Simple substitution in Equations (5.1) and (5.2) details the volume of material removed from frictional forces, V , as

$$V = \frac{KaP}{3H} \quad (5.3)$$

Because the volume of material removed is inversely proportional to the hardness, harder materials should have less material removed in frictional contacts. This relationship would suggest that harder materials, such as Ru or Pt, should have improved resistance to material removal over softer materials such as Au. Despite the increase of hardness in the top layer for ultra-thin coatings, it is unclear how ultra-thin hard coatings on a soft substrate will affect the amount of material removed during frictional contact, since the hardness can be lower than either the coating or the substrate due to membrane stresses in the coating, as demonstrated in Section 3 [62]. Through scratch testing, the wear behavior for ultra-thin Ru and Pt coatings can be examined. This study will compare the scratch testing results to those found in nanoindentation to explore deformation mechanisms. Additionally, ductility reduction in contact separation is explored through asymmetric contacts.

5.1. Methods

The films and coatings were fabricated by sputter deposition (100) oriented Si wafers. The Si wafers were first coated with a 20 nm thick Cr adhesion layer from a 99.95% pure Cr target. On top of the Cr adhesion layer, a 350 nm thick Au film was deposited at 2 mTorr at room temperature from a 99.99% pure Au target at $\sim 2 \text{ \AA/s}$. After deposition, wafer curvature measurements made using a Tencor FLX2330 revealed a small residual compressive stress ($\sim 80 \text{ MPa}$) in the Au film. One of the pieces was then coated with a 10 nm ultra-thin Ru, and another with a 10 nm ultra-thin Pt layer. One

piece was left uncoated after the Au deposition (Au-only film). Both the Ru and Pt coatings on sectioned pieces of films were sputtered at 2 mTorr. All of the Ru coatings were deposited from a 99.95% pure Ru target at ~ 1.5 Å/s at room temperature, and all of the Pt coatings were deposited from a 99.99% pure Pt target at ~ 1.5 Å/s at room temperature. Coating thickness was measured during deposition with a crystal monitor. All three material systems (Au-only, Ru coating, and Pt coating) were extremely smooth, with a root mean square (RMS) surface roughness less than 2 nm over a 2.0 by 2.0 μm scan area. As detailed in [62], AFM and TEM analysis of the film surfaces suggest small (5-30 nm) nanocrystalline grain structure in both the Au film and Ru and Pt coatings. AES and TEM cross-sections indicated that the Ru coating was continuous on the surface of the Au film [62].

The adhesive behavior was evaluated by using peak-force tapping mode on a Bruker Dimension FastScan AFM. A Bruker PFTuna Pt/Ir coated Si tip on a Si_3N_4 cantilever was used. Prior to testing, both the deflection sensitivity and cantilever stiffness were calibrated. A 2x2 μm scan was taken of each sample, recording the height, adhesion, and dissipation channels. All images had 512 samples/line with a 0.501 Hz sampling rate. To verify information in the images, force-displacement curves were recorded at several locations on each sample. Each location sampled had 5 force-displacement curves. A setpoint (maximum force) of 750 pN was used.

The mechanical behavior was examined using a Hysitron TriboIndenter (Hysitron, Inc., Minneapolis, MN) with a diamond Berkovich indenter tip. A previous study examine the indentation hardness of the coating systems, and details of those investigations are given in [62]. To evaluate wear, scratch testing was also performed on

the samples. The scratch testing performed a 2 μm long scratch with a constant force of 100 μN , with a loading and unloading rate of 50 $\mu\text{N/s}$. A 4x4 μm scan of the scratched area was performed immediately after each scratch test by using the indenter tip as a profilometer stylus. A setpoint of 2 μN was used during imaging, and tests were performed to ensure that the *in-situ* scanning setpoint did not cause alter the scratch profile. Three scratches were performed on each sample. Each scan had 256 samples/line and a scanning rate of 1 Hz.

5.2. Results

To examine the wear behavior of the ultra-thin coated Au films, the stiction behavior is first examined for the 10 nm Ru and Pt coatings and compared to the Au-only film. Then, the wear differences between the coated samples and the Au-only film are evaluated through scratch testing.

5.2.1. Stiction Behavior

For the Au-only sample, the average adhesive (or pull-off) force using a Pt/Ir AFM cantilever was 1.03 ± 0.14 nN (Figure 5.1). The Au-only sample had a significantly lower adhesion force than either the Ru or Pt coated samples (Figure 5.1). The Ru coating adhesive force was 5.05 ± 0.11 nN, and the Pt coating adhesive force was 5.26 ± 0.31 nN. The Au adhesive force is expected to be lower than either the Ru or Pt coated samples

due to predictions from the Derjaguin-Müller-Toporov (DMT) predicted adhesive force, F_{ad} ,

$$F_{ad} = 2\pi a W_{ad} \quad (5.4)$$

where a is the contact radius and W_{ad} is the work of adhesion (different from the wear parameter W) [46]. The work of adhesion is calculated from surface and interfacial energies, γ , so that

$$W_{ad} = \gamma_{1m} + \gamma_{2m} + \gamma_{12} \quad (5.5)$$

where the subscripts 1 and 2 refer to each contact material, and m refers to the medium (in this situation, air) [46]. The surface energy of Au is 1.3 J/m^2 , while the surface energies for Ru and Pt are 4.3 J/m^2 and 2.2 J/m^2 , respectively [84, 85]. However, the exact predicted adhesion force is difficult to predict because the exact composition of the tip is unknown. Additionally, the adhesive forces are difficult to measure accurately for several reasons, including build-up of contamination on the surfaces, uncertainty in the contact radius and geometry, and the empirical modeling of the adhesion forces through the DMT method [46, 47]. Despite these complexities, but we can still expect the Au film to have lower adhesion forces than either Ru or Pt. While those factors can negatively affect quantitative adhesive force analysis, comparisons between material systems can still be successfully made.

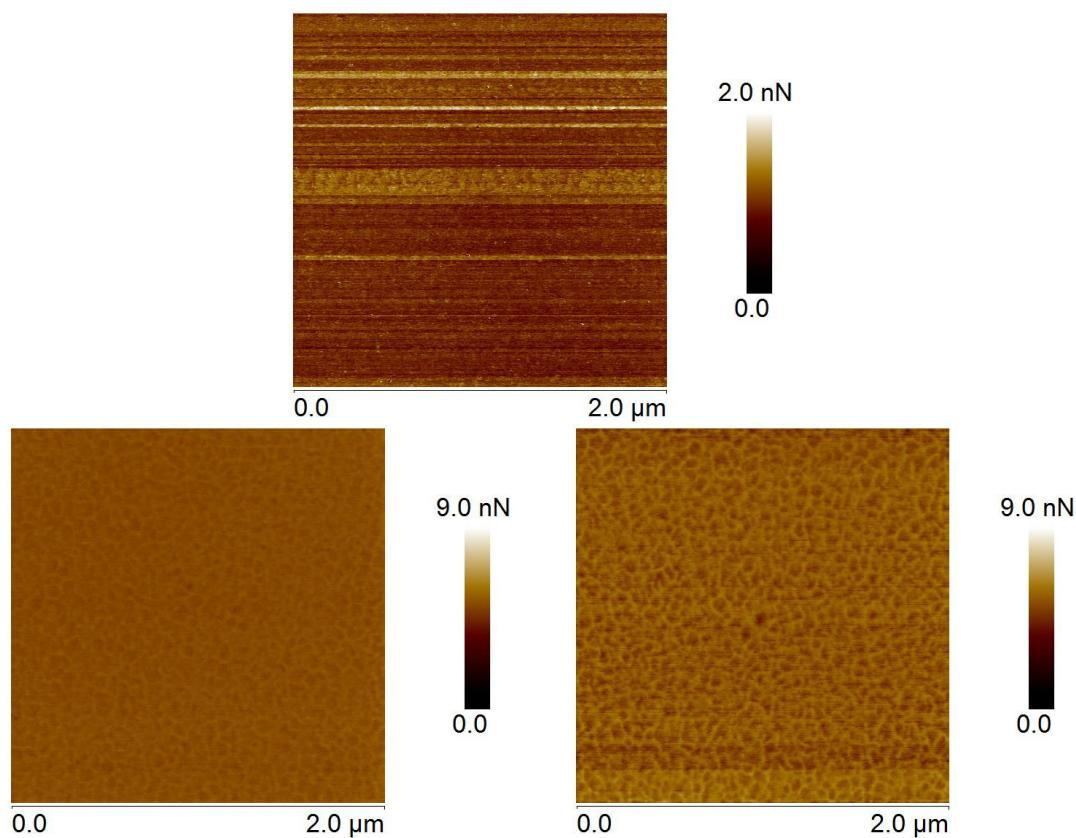


Figure 5.1: Adhesive force obtained through scanning mode for a) Au-only film, b) Ru coating, and c) Pt coating. The colorbar for the Au-only sample is different to better show the contrast in the original image.

The adhesive forces in the force-displacement plots are slightly different than those obtained through the scanning mode (Figure 5.2). Specifically, the Au sample had much higher adhesion forces in the force-displacement plots than in the scanning mode. This may be due to cyclic contact of the surface; Patton and Zabinski noted that the adhesion increased with cyclic testing [3]. It may also be due to the larger forces applied during the force-displacement ramping. The force-displacement plots can also detail the separation height necessary to break contact. Generally, material transfer and necking of the contact area can be linked to larger retraction separation values, although the separation can be complicated by contamination layers [17]. In this experimental study, unlike the MD

simulation by Fortini et al., the Ru contact had significantly larger separation heights and work of adhesion than the Au contact. The Ru contact exhibited the largest separation heights and work of adhesion, followed by the Pt sample. The Au sample had the lowest separation heights and work of adhesion.

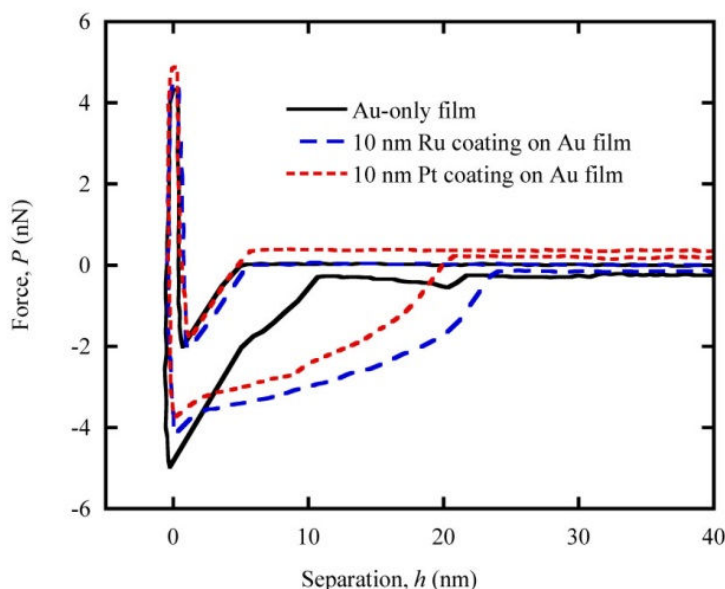


Figure 5.2: Representative force-displacement plot for a Pt/Ir AFM tip in contact with Au-only film.

The force-displacement plots also suggest there are differences in contamination levels between the different surfaces. It is well known that Au surfaces easily absorb carbonaceous contamination layers [8], while Pt is a well-known reducer of NO_x . The surfaces will have different reactivities with different contamination compounds. The Au-only film shows low levels of contamination, as demonstrated by the sharp slope of the initial retraction and the limited amount of data points between the maximum adhesive force and full separation (where $P=0$), suggesting that separation was a quick process.

Comparatively, the Ru and Pt coated films show much shallower retraction curves with more data points in the force-separation plot, suggesting there are larger amounts of contamination present on those surfaces.

Interestingly, the imaging mode for the Au-only film shows large amounts of streaking, which is often linked to surface contact problems caused by contamination debris. These streaks are not present on the Ru or Pt coated films. Since the imaging is performed before, and in the same location as, the ramping mode, it is possible that the imaging process effectively “wipes” the contamination from the surface during the imaging of the Au-only film. Then, when the force-displacement ramps are being conducted on the Au-only film, there is a clean metallic surface at the contact area. Since the Ru and Pt coated films do not show any streaking in the imaging mode, the contamination might not have been wiped away, leading to large amounts of contamination during the ramping. However, this study shows that simple adhesion studies of ohmic contact materials performed in laboratory air will not effectively predict the behavior of contacts when packaged. To mitigate contamination issues and simulate packaged contact behavior, contamination layers need to be controlled.

When examining the hardness and plane strain modulus behavior, the AFM mechanical response differs from the results found during nanoindentation testing [62]. The Hertzian contact analysis of nanoindentation testing showed that the force-displacement response of the Ru and Pt coated samples was statistically different from the Au-only behavior. Specifically, the unloading stiffness was significantly reduced due to the presence of the Ru or Pt coating [62]. However, when the force-displacement curves for the AFM peak-force tapping were examined, there is no significant differences

between the unloading curves. Since the AFM tests have a maximum displacement of approximately 2 nm and the coating thickness is 10 nm, the AFM tests should be better described by indentation substrate models (as opposed to indentation membrane models). Substrate models use a weighted function of tip, substrate, and coating properties. One such model is given by King, so that

$$\frac{S}{S_0} = \frac{\frac{1 - \nu_s^2}{E_s} + \frac{1 - \nu_i^2}{E_i}}{\frac{1 - \nu_c^2}{E_c} \left(1 - e^{-\frac{\alpha t}{a}}\right) + \frac{1 - \nu_s^2}{E_s} e^{-\frac{\alpha t}{a}} + \frac{1 - \nu_i^2}{E_i}} \quad (5.6)$$

where E is the Young's modulus, ν is the Poisson's ratio, the subscripts "c", "s", and "i" refer to the coating, substrate, and tip properties, a is the contact radius, t is the coating thickness, α is a parameter based on tip geometry and a/t ratios, and S_0 is a normalizing parameter given by

$$S_0 = \beta E^* \sqrt{A_c} \quad (5.7)$$

where the β term is a geometric correction factor, and is equal to 1.129 for a circular punch [39]. From Equation (5.6), you can see that as the indentation depth decreases (and t/a increases), the relative contribution from the coating increases. At approximately 20% of the coating thickness, the contribution from the coating should be significant.

Additionally, the plane strain elastic modulus, E_{ps} or $E/(1-\nu^2)$, is 492 GPa for Ru, 210 GPa for Pt, and 99 GPa for Au [69]. Based on the substrate model, there should be significant increases in the unloading stiffness due to the presence of a Ru or Pt coating on an Au substrate under Hertzian contact stresses.

However, when adhesive forces are present, the Hertzian contact analysis is no longer appropriate. The Hertzian contact stresses predict the plane strain modulus as

$$E_{ps} = \frac{RP}{a^3} \quad (5.8)$$

where R is the tip radius, P is the force, and a is the contact radius [46]. The Derjaguin-Müller-Toporov (DMT) model describes the case where there are significant adhesive forces. In the DMT model, the plane strain modulus is given as

$$E_{ps} = \frac{R}{a^3} (P + 2\pi RW) \quad (5.9)$$

where W is the work of adhesion, and the other constants are the same as in Equation (5.8) [46]. While the adhesive forces are much smaller than the maximum force during nanoindentation, they are a much larger contribution to the AFM force-displacement response. For the same force and contact radius, larger work of adhesion should increase the plane strain modulus. Since the tip radius is not well known for the AFM tip, the plane strain modulus is not calculated. Still, relative comparisons can still be made between the different material systems. Since the force-displacement response was the same during loading for the Ru and Pt coatings as the Au-only sample, the material with the largest work of adhesion should have the largest plane strain modulus. The Ru sample has the largest work of adhesion (Figure 5.2), and it should also have the largest plane strain modulus (492 GPa). The Au sample has the lowest work of adhesion, and it should also have the smallest plane strain modulus (99 GPa).

The increased stiffness of the coated samples is predicted by the weighted substrate model given by King [39]. This situation is in contrast to the nanoindentation tests detailed in [62]. In [62], the indentation depth was on the order of the coating thickness, and is better described by membrane models. When the indentation depth was on the order of the coating thickness, the stiffness of the contact was actually decreased

by the presence of the Ru or Pt coating in nanoindentation tests. Thus, as the contact depth to coating thickness changes, a transition from substrate to membrane model occurs. A stiff coating (with a large E_{ps}) increases the contact stiffness at shallow depths, and then decreases it at depths on the order of the coating thickness. By changing the coating thickness to contact depth ratio, the total stiffness of the response can significantly altered.

5.2.2. Wear Behavior

To evaluate the wear of contacts under frictional loading, scratch testing was also performed on the Au-only film and the Ru and Pt coatings. To determine the amount of wear, the scratch depth was measured from *in-situ* profilometry images of the scratch (Figure 5.3). The Au film had the deepest scratch depth, and the largest volume of material removed, as can be seen in Table 1. In addition to the different scratch depths, the Au film and Pt and Ru coatings had different amounts of piled-up material around the scratch, indicating different amounts of plasticity (Figure 5.3 and Table 5.1). The Au had the most material piled-up around the scratch, which is consistent with previously noted pile-up around traditional indents [62]. Despite a previous study showing that the hardness actually decreased at shallow indentation depths due to Ru and Pt coatings, this study shows that when the coatings are also subject to frictional forces, there is increased wear resistance. This finding has very important implications for ohmic contact switches. The ultra-thin coatings allow the contact area to remain relatively unaffected under normal loading, which will keep the contact resistance low. This is in contrast to

monolithic Pt or Ru films, which significantly increased the hardness and decreased contact area [70]. However, the coatings provide increased resistance to wear, which should increase the lifetimes of the devices they are used in.

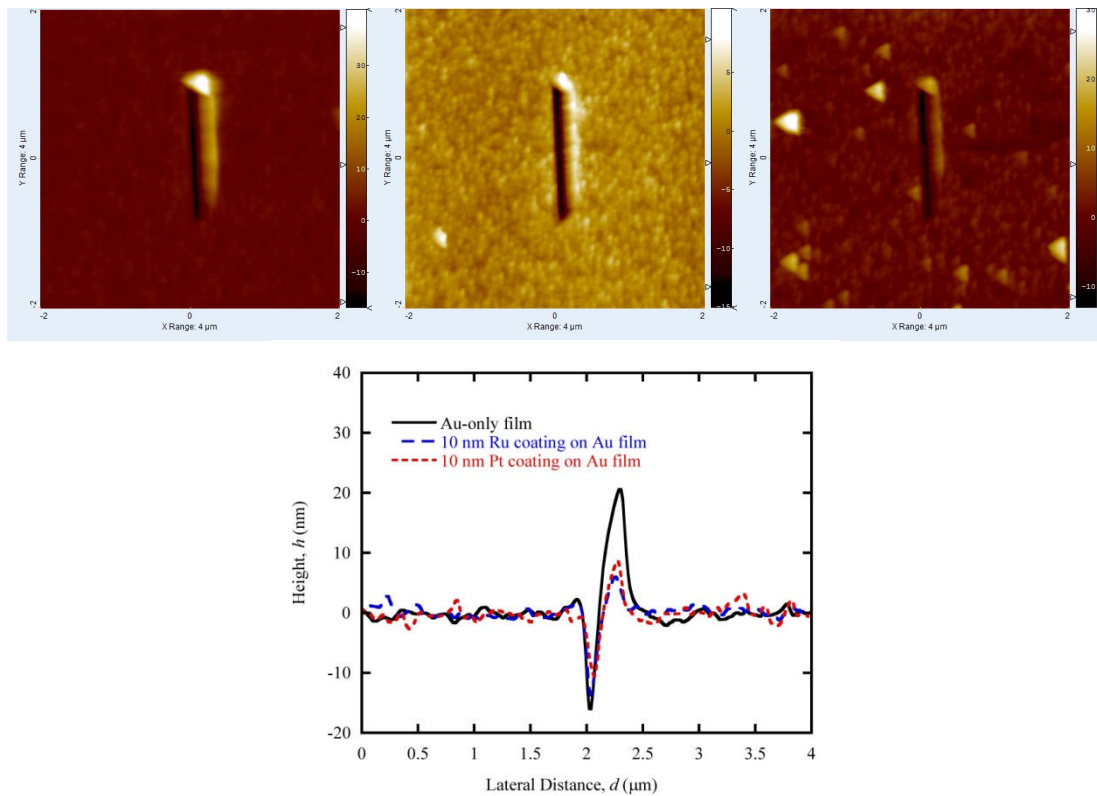


Figure 5.3: Scratch test in-situ scans of a) Au-only films, b) 10 nm Ru coating, and c) 10 nm Pt coating. Average cross-section profiles of each material system are shown in d).

Table 5.1: Scratch characteristics.

Material	Scratch Depth (nm)	Pile-up Height (nm)
Au film	15	21
10 nm Ru coating on Au film	14	7
10 nm Pt coating on Au film	12	12

5.3. Conclusions

Asymmetric metallic contacts were evaluated for adhesive forces and unloading stiffness. The Ru and Pt coatings showed larger amounts of contamination in force-separation plots, while the Au-only film demonstrated evidence of wiping the contamination layer away during the imaging mode and had contacts with limited contamination in the force-separation plots. The unloading stiffness for the Ru and Pt coating was the same as for the Au-only film. However, because the Ru and Pt samples had higher work of adhesion, the coated samples had larger predicted plane strain moduli than the Au sample, in contrast to the nanoindentation testing. Thus, when the contact depth was kept sufficiently small, the contact stiffness increased as predicted by substrate models. When the contact depth was on the order of the coating thickness, the contact stiffness actually decreased [62]. Scratch studies of ultra-thin hard coatings (Ru and Pt) on Au films show that the presence of the hard coating increase wear resistance. Because a previous study also showed that the contact area was largely unaffected by the coating [62], the contact resistance should not be negatively affected by the coating layer. This study suggests that ultra-thin coatings would be an improved material system in ohmic contact switches by increasing life limits while keeping the power consumption low.

Chapter 6

Conclusions

Ultra-thin Ru and Pt coatings on were evaluated both mechanically and electrically to determine their applicability for RF MEMS ohmic contact switches. Additionally, fundamental studies were made into how ultra-thin coatings behave under contact stresses. Implications of contact resistance measurements on thin films were explored. Finally, experiments were performed to determine stiction and friction behavior of the coated material systems.

6.1. Summary of Findings

When an ultra-thin Ru or Pt coating was added to an Au film, the elastic and plastic behavior were statistically significantly affected due to the coating behaving as a membrane on an elastic-plastic half-space. When the indentation depth was much larger than the coating thickness, the hardness was increased. At indentation depths on the order of the coating thickness, the hardness was actually decreased, despite the increased hardness of the coating. The decreased hardness is predicted by indentation membrane models, which state that the membrane increases the tensile stress in the substrate, causing yielding to occur at lower stresses. Further, by decreasing the compressive residual stress, the hardness was actually increased at indentation depths on the order of

the coating thickness. However, when the indentation depth was much larger than the coating thickness, the hardness was increased.

The elastic behavior was also affected by the presence of the ultra-thin coating. For indentation depths on the order of the coating thickness, the unloading stiffness and plane strain modulus decreased. At indentation depths much larger than the coating thickness, the plane strain moduli converged to the Au-only value. When the residual stress was decreased in the coating, the plane strain modulus increased at depths much greater than the coating thickness, but had no effect at depths on the order of the coating thickness. For 50 and 100 nm thicker films where the indentation depth was a smaller fraction of the film thickness, the hardness and reduced modulus was increased over the Au-only film. The Ru and Pt coated films had distinctly different plane strain moduli and hardness values.

Decreasing h/t and a/t ratios for the thicker (50 and 100 nm) films caused decreasing membrane effects. Instead, the thicker films start to approach substrate models, where the total system response is predicted by a weighted function of the tip, substrate, and coating properties. This study notes that the transition occurs around $h/t=0.5$. The residual stress effects on hardness were also in agreement with indentation membrane modeling. The membrane models predict that decreasing the compressive stress in the coating decreases the tensile stresses in the substrate. By decreasing the tensile stresses in the substrate, the measured hardness increases. Since the deformation behavior changed with residual stress state in the coating, we have confirmed that the mechanical response can be tailored by altering the stress state and the coating thickness

to achieve a desired response. Additionally, the ultra-thin coatings have a meaningful effect on the mechanical response of a film system under contact loading.

When indentation tests were performed at a lower force scale using an AFM, the contact response was better described by substrate models. With the AFM testing, the adhesion force was measured, and the relative adhesive forces corresponded to their individual surface energies. Unlike the nanoindentation testing at larger forces and contact areas, the unloading stiffness for the Ru and Pt coating was the same as for the Au-only film. However, the adhesive forces must be considered when modeling the contact stresses. Because the Ru and Pt samples had higher work of adhesion, the coated samples had larger predicted plane strain moduli than the Au sample, in contrast to the nanoindentation testing. When the contact depth was kept sufficiently small, the plane strain modulus increased as predicted by substrate models. Scratch studies of ultra-thin Ru and Pt coatings on Au films show that the presence of the hard coating reduced the volume of material removed and increased wear resistance.

When evaluating the contact resistance of the ultra-thin coatings, we discovered that the traditional method for prediction of measured contact resistances is flawed [3, 49, 53, 72-78]. The traditional method assumes that the contact resistance is significantly larger than the resistance through the sample, but the resistance in the sample can be relatively large for the thin films using in ohmic contact switches. Because the sheet resistances in the film are large and do not vary with force, the high contact resistances with low or no dependence on force that are noted in the literature can be easily explained. To maximize the contribution from the contact resistance, a four wire configuration should be used with the probes placed as close to the contact as possible.

However, even when the probes are placed at the edge of the expanding contact area, the total resistance-force behavior deviates significantly from Holm's law due to the sheet resistance contribution. This deviation from Holm's law will be more pronounced for MEMS devices than NEMS devices, because the contact resistance is smaller for larger radii. Because the contact resistance is larger for smaller radii, decreasing the contact radius will help to isolate the contact resistance from the sheet resistance. If the probe spacing and tip radius are minimized, the contact resistance can more effectively be analyzed in a sample and comparisons can be made between samples. Additionally, to minimize power consumption in RF MEMS and NEMS, the transmission line between the contact areas and the source and drain should be as short as possible. Further, since the constriction resistance is a very small fraction of the power consumption in the devices, more effort should be put on maximizing surface stability (i.e., minimizing adhesion and reducing arcing) and increasing reliability. Finally, due to the small contact radius, it will be much more important to control constriction resistance for NEMS devices than MEMS.

Because the contact resistance is a small fraction of the total resistance in an RF MEMS ohmic contact switch, improvements will address the large power consumption in the transmission lines. While material systems such as Ru and Pt have been evaluated for improved device reliability [7, 12], the higher resistivity of those materials will significantly increase the sheet resistance and power consumption of the devices. By adding an ultra-thin Ru or Pt coating, most of the conduction can occur in the underlying Au layer, while the surface can be improved with the hard coating. Contact resistance measurements on the layered system show no change in the measured resistance due to

the sheet resistance being largely unaffected by the coating layer. Nanoindentation studies show that the contact area can actually be increased due to the hard coating under certain loading conditions. Further, scratch testing showed improved wear properties for the ultra-thin coated samples. In summation, ultra-thin Ru and Pt coatings on Au films are improved material systems for RF MEMS ohmic contact switches because of the lack of increased power consumption and the improvement of the wear properties.

6.2. Future Work

There are several areas where this work can be continued and further investigated. The first set of tests would involve continuing to evaluate the electrical behavior. The second suggested experiments involve further evaluation of surface adhesive forces and wear characteristics.

A suggested further electrical test would be to perform contact resistance measurements using a conductive AFM to verify its concurrence with the measured resistance model. Conductive AFM tests should also demonstrate that the relative contact resistance contribution is larger for smaller radii tips, and will be more important for NEMS than for MEMS devices.

Full scale electrical testing of devices of Ru and Pt coated Au films is also suggested for future work. The full scale testing should evaluate the total power consumption for layered systems. Additionally, it would dictate whether the addition of an ultra-thin layer of Ru or Pt significantly increases the power consumption, or has a minimal effect on the power consumption as suggested by our current testing. Full scale

device testing also provides information about the cyclic loading behavior and the failure mechanisms of layered systems.

It would also be interesting to independently evaluate the wear behavior using techniques such as nano-scale scratch and wear testing. Tests detailed in Chapter 5 of this thesis showed that at 100 μN of scratch force, the resistance to deformation was similar to the deepest indentation tests for the layered systems. It would be enlightening to evaluate other forces and scratch distances. Additionally, the indentation tests were performed with a conospherical tip, while the scratch testing was performed with a Berkovich tip. However, the asymmetric pileup during scratch testing created due to the Berkovich tip complicated analysis of the surface resistance to lateral forces. Scratch testing with a conospherical tip is recommended for further testing.

As noted in Chapter 5, the varying amounts of contamination on the surfaces during adhesion testing could have affected the mechanical testing. Since the thin films can be largely affected by very thin contamination layers, it is extremely difficult to control the environment and surface of the material prior to testing. Alternately, if the adhesion testing is performed where the surface is submerged under an organic solvent, thereby controlling the contamination layer at the surface, further comparative adhesion studies can be performed.

The electrical, wear, and adhesion testing is important to furthering understanding of the performance of ohmic contact switches. The tests will evaluate the viability of ultra-thin Ru and Pt coatings on Au films for incorporation in RF MEMS ohmic contact switches. The tests will also evaluate fundamental layered system behavior that can be used to predict which layered systems would have the best performance in devices.

References

- [1] G.M. Rebeiz, J.B. Muldavin, *IEEE Microwave Magazine* 2 (2001) 59.
- [2] S. Majumder, N.E. McGruer, G.G. Adams, P.M. Zavracky, R.H. Morrison, J. Krim, *Sens. Actuators A* 93 (2001) 19.
- [3] S.T. Patton, J.S. Zabinski, *Tribol. Lett.* 18 (2005) 215.
- [4] S.T. Patton, J.S. Zabinski, *Reliability, Packaging, Testing, and Characterization of MEMS/MOEMS V*, San Jose, CA, 2006, SPIE 6111 (Jan. 25-26) p. 61110.
- [5] S.G. Tan, E.P. McErlean, J.S. Hong, Z. Cui, L. Wang, R.B. Greed, D.C. Voyce, *13th European Gallium Arsenide and other Compound Semiconductors Application Symposium*, Paris, France, 2005, IEEE (Oct. 3-4) p. 505.
- [6] R. Holm, *Electric contacts; theory and application*, Springer-Verlag, New York, 1967.
- [7] A. Broue, J. Dhennin, P. Charvet, P. Pons, N.B. Jemaa, P. Heeb, F. Coccetti, R. Plana, *2010 Proceedings of the 56th IEEE Holm Conference on Electrical Contacts*, Piscataway, NJ, USA, 2010, IEEE p. 10 pp.
- [8] S.T. Patton, K.C. Eapen, J.S. Zabinski, *Tribol. Int.* 34 (2001) 481.
- [9] N.E. McGruer, G.G. Adams, L. Chen, Z.J. Guo, Y. Du, *19th IEEE International Conference on Micro Electro Mechanical Systems*, Istanbul, Turkey, 2006, IEEE 2006 (Jan. 22-26) p. 230.
- [10] B.D. Jensen, L.L.W. Chow, H. Kuangwei, K. Saitou, J.L. Volakis, K. Kurabayashi, *J. Microelectromech. Sys.* 14 (2005) 935.
- [11] R.A. Coutu Jr., J.R. Reid, R. Cortez, R.E. Strawser, P.E. Kladitis, *IEEE Transactions on Components and Packaging Technologies* 29 (2006) 341.
- [12] H. Lee, R.A. Coutu, S. Mall, K.D. Leddy, *Journal of Micromechanics and Microengineering* 16 (2006) 557.
- [13] T. Bannuru, W.L. Brown, S. Narksitipan, R.P. Vinci, *J. Appl. Phys.* 103 (2008) 083522.
- [14] Z. Yang, D.J. Lichtenwalner, A.S. Morris Iii, J. Krim, A.I. Kingon, *J. Microelectromech. Sys.* 18 (2009) 287.
- [15] H. Ibach, H. Lüth, *Solid-State Physics: An Introduction to Principles of Materials Science*, Springer Berlin Heidelberg, 2009, p. 241.
- [16] V. Mulloni, R. Bartali, S. Colpo, F. Giacomozzi, N. Laidani, B. Margesin, *Mater. Sci. Eng. B* 163 (2009) 199.
- [17] A. Fortini, M.I. Mendeleev, S. Buldyrev, D. Srolovitz, *J. Appl. Phys.* 104 (2008).
- [18] R.A. Coutu Jr., P.E. Kladitis, K.D. Leedy, R.L. Crane, *J. Micromech. Microeng.* 14 (2004) 1157.
- [19] H.C. Angus, *British Journal of Applied Physics* 13 (1962) 58.
- [20] A. Tonck, F. Houze, L. Boyer, J.L. Loubet, J.M. Georges, *J. Phys., Condens. Matter* 3 (1991) 5195.
- [21] M. Ohba, K. Kuzukawa, K. Sakairi, *34th IEEE Holm Conference on Electrical Contacts*, San Francisco, CA, USA, 1988, IEEE (Sept. 26-29) p. 311.
- [22] J.W. Tringe, T.A. Uhlman, A.C. Oliver, J.E. Houston, *J. Appl. Phys.* 93 (2003) 4661.

- [23] F.W. Delrio, K.L. Steffens, C. Jaye, D.A. Fischer, R.F. Cook, *Langmuir* 26 1688.
- [24] T. Yamashita, T. Itoh, T. Suga, *Sensors and Actuators: A Physical* 172 (2011) 455.
- [25] T. Yamashita, T. Itoh, T. Suga, Piscataway, NJ, USA, 2009, IEEE p. 794.
- [26] T.Y. Tsui, W.C. Oliver, G.M. Pharr, *Journal of Materials Research* 11 (1996) 752.
- [27] A. Bolshakov, W.C. Oliver, G.M. Pharr, *Journal of Materials Research* 11 (1996) 760.
- [28] K.O. Kese, Z.C. Li, B. Bergman, *Journal of Materials Research* 19 (2004) 3109.
- [29] J.G. Swadener, B. Taljat, G.M. Pharr, *J. Mater. Res.* 16 (2001) 2091.
- [30] S. Suresh, A.E. Giannakopoulos, *Acta Materialia* 46 (1998) 5755.
- [31] J.-Y. Kim, J.-J. Lee, Y.-H. Lee, J.-I. Jang, D. Kwon, *Journal of Materials Research* 21 (2006) 2975.
- [32] C. Walter, T. Antretter, R. Daniel, C. Mitterer, *Surface and Coatings Technology* 202 (2007) 1103.
- [33] M.S. Bobji, K. Shivakumar, H. Alehossein, V. Venkateshwarlu, S.K. Biswas, *International Journal of Rock Mechanics and Mining Sciences* 36 (1999) 399.
- [34] J. Mencik, M.V. Swain, Boston, MA, USA, 1995, Materials Research Society, Pittsburgh, PA, USA 356 p. 729.
- [35] M.V. Swain, J. Mencik, *Thin Solid Films* 253 (1994) 204.
- [36] S. Hyun, O. Kraft, R.P. Vinci, *Acta Materialia* 52 (2004) 4199.
- [37] A.C. Fischer-Cripps (Ed.), *Nanoindentation*, Springer-Verlag, New York, 2004.
- [38] M.F. Doerner, W.D. Nix, *Journal of Materials Research* 1 (1986) 601.
- [39] R.B. King, *Int. J. Sol. Struct.* 23 (1987) 1657.
- [40] R.B. King, T.C. O'Sullivan, *Int. J. Sol. Struct.* 23 (1987) 581.
- [41] H. Gao, C.-H. Chiu, J. Lee, *International Journal of Solids and Structures* 29 (1992) 2471.
- [42] S.M. Han, R. Saha, W.D. Nix, *Acta Materialia* 54 (2006) 1571.
- [43] S.K. Vanimisetti, R. Narasimhan, *Int. J. Sol. Struct.* 43 (2006) 6180.
- [44] P.M. Ramsey, H.W. Chandler, T.F. Page, *Surf. Coat. Technol.* 49 (1991) 504.
- [45] M.R. McGurk, T.F. Page, *Surface and Coatings Technology* 92 (1997) 87.
- [46] H.-J. Butt, B. Cappella, M. Kappl, *Surface Science Reports* 59 (2005) 1.
- [47] J. Drelich, G.W. Tormoen, E.R. Beach, *Journal of Colloid and Interface Science* 280 (2004) 484.
- [48] K.W. Gilbert, S. Mall, K.D. Leedy, *Journal of Adhesion Science & Technology* 24 (2010) 2597.
- [49] R.A. Coutu Jr., J.W. McBride, L.A. Starman, 55th IEEE Holm Conference on Electrical Contacts, HOLM 2009, Vancouver, BC, Canada, 2009, IEEE (Sept 14-16) p. 295.
- [50] P.G. Slade, *Electrical Contacts: Principles and Applications*, Taylor & Francis, 1999.
- [51] R.S. Timsit, *IEEE Transactions on Components and Packaging Technologies* 33 (2010) 636.
- [52] P. Zhang, Y.Y. Lau, R.M. Gilgenbach, *J. Appl. Phys.* 109 (2011).
- [53] D. Hyman, M. Mehregany, *IEEE Transactions on Components and Packaging Technologies* 22 (1999) 357.

- [54] T.B. Massalski, H. Okamoto, P.R. Subramanian, L. Kacprzak (Eds.), Binary alloy phase diagrams, ASM International, 1990.
- [55] M. Ohring, Materials Science of Thin Films: Deposition and Structure, Academic Press, San Diego, CA, 2002.
- [56] C.L. Hedberg (Ed.), Handbook of Auger Electron Spectroscopy: A Book of Reference Data for Identification and Interpretation in Auger Electron Spectroscopy, Physical Electronics, Eden Prairie, Minnesota, 1995.
- [57] Y. Jaluria, Computer methods for engineering, Taylor & Francis, Washington, DC, 1996.
- [58] Corning, 2004.
- [59] W.C. Oliver, G.M. Pharr, Journal of Materials Research 19 (2004) 3.
- [60] A.L. Romasco, L.H. Friedman, L. Fang, R.A. Meirum, T.E. Clark, R.G. Polcawich, J.S. Pulskamp, M. Dubey, C.L. Muhlstein, Thin Solid Films 518 (2010) 3866.
- [61] A. Daire, Keithley Instruments, Inc., 2005.
- [62] A.L. Romasco-Tremper, S.E. Mohney, K.L. Andre, J. Lin, C.L. Muhlstein, Mater. Sci. Eng. A (submitted).
- [63] R. Saha, W.D. Nix, Acta Mater. 50 (2002) 23.
- [64] C. Gamonpilas, E.P. Busso, Mater. Sci. Eng. A 380 (2004) 52.
- [65] ISO, Metallic materials -- Instrumented indentation test for hardness and materials parameters -- Part 1: Test method, 2002.
- [66] ISO, Metallic materials -- Instrumented indentation test for hardness and materials parameters -- Part 2: Verification and calibration of testing machines, 2002.
- [67] ISO, Metallic materials -- Instrumented indentation test for hardness and materials parameters -- Part 4: Test method for metallic and non-metallic coatings, 2007.
- [68] W.C. Oliver, G.M. Pharr, J. Mater. Res. 7 (1992) 1564.
- [69] G. Simmons, H. Wang, Single Crystal Elastic Constants and Calculated Aggregate Properties: A Handbook, The M.I.T. Press, Cambridge, MA, 1971.
- [70] H. Lee, R.A. Coutu, S. Mall, K.D. Leedy, J. Micromech. Microeng. 16 (2006) 557.
- [71] J.H. Kim, A. Gouldstone, J. Mater. Res. 23 (2008) 2212.
- [72] P.D. Grant, R.R. Mansour, M.W. Denhoff, Canadian Journal of Electrical and Computer Engineering 27 (2002) 33.
- [73] D.J. Dickrell III, M.T. Dugger, Chicago, IL, United states, 2005, Institute of Electrical and Electronics Engineers Inc. 2005 p. 255.
- [74] D.J. Dickrell III, M.T. Dugger, IEEE Transactions on Components and Packaging Technologies 30 (2007) 75.
- [75] B.L. Pruitt, T.W. Kenny, Sens. Actuators A A104 (2003) 68.
- [76] K. Kataoka, S. Kawamura, T. Itoh, T. Suga, K. Ishikawa, H. Honma, Fifteenth IEEE International Conference on Micro Electro Mechanical Systems, Piscataway, NJ, USA, 2002, IEEE p. 364.
- [77] E.M. Yunus, J.W. McBride, S.M. Spearing, IEEE Transactions on Components and Packaging Technologies 32 (2009) 650.
- [78] A. Broue, J. Dhennin, C. Segueineau, X. Lafontan, C. Dieppedale, J.M. Desmarres, P. Pons, R. Plana, 2009 IEEE International Reliability Physics Symposium (IRPS), Piscataway, NJ, USA, 2009, IEEE p. 869.

- [79] S.D. Washko, G. Aggen, ASM Handbook, vol. 1, ASM International, 1990, p. 841.
- [80] D.J. Dickrell III, M.T. Dugger, Washington, D.C., United states, 2005, American Society of Mechanical Engineers p. 807.
- [81] G. Norberg, S. Dejanovic, H. Hesselbom, IEEE Transactions on Components and Packaging Technologies 29 (2006) 371.
- [82] H.F. Dadgour, M.M. Hussain, A. Cassell, N. Singh, K. Banerjee, Reliability Physics Symposium (IRPS), 2011 IEEE International (10-14 April 2011) p. 3D.3.1.
- [83] J.F. Archard, J. Appl. Phys. 24 (1953) 981.
- [84] R.J. Needs, M. Mansfield, J. Phys., Condens. Matter 1 (1989) 7555.
- [85] M.Y. Chou, J.R. Chelikowsky, Physical Review B 35 (1987) 2124.

VITA

Amber Leigh (Romasco) Tremper

Education:

Ph.D. in Materials Science and Engineering at Pennsylvania State University

M.S. in Materials Science and Engineering at Pennsylvania State University

Thesis: Time dependent deformation of thin film platinum during nanoindentation testing

B.S. in Engineering Science at Pennsylvania State University

Minor: Engineering Mechanics

Scholarships and Awards Received:

- University Graduate Fellowship (2006 – 2007)
- 3M Graduate Fellowship (2006 – 2009)
- Anne C. Wilson Award (2006 – 2007)

Publications:

Romasco, A.L., L.H. Friedman, L. Fang, R.A. Meiom, T.E. Clark, R.G. Polcawich, J.S. Pulskamp, M. Dubey, C.L. Muhlstein. (2010). "Deformation behavior of nanograined platinum films." *Thin Solid Films* **518**(14): 3866-74.

Romasco, A.L., L.H. Friedman, L. Fang, R.A. Meiom, T.C. Clark, R. Polcawich, J. Pulskamp, M. Dubey, C.L. Muhlstein. (2010). "Practical implications of instrument displacement drift during force-controlled nanoindentation." *Journal of Testing and Evaluation* **38**(2): JTE102177 (8 pp.).

Fang, L., C.L. Muhlstein, J.G. Collins, A.L. Romasco, L.H. Friedman. (2008). "Continuous electrical in situ contact area measurement during instrumented indentation." *Journal of Materials Research* **23**(9): 2480-2485.

Lei, F., C.L. Muhlstein, A.L. Romasco, J.G. Collins, L.H. Friedman. (2009). "Augmented instrumented indentation using nonlinear electrical contact current-voltage curves." *Journal of Materials Research* **24**(5): 1820-32.

Meiom, R.A., D.H. Alsem, A.L. Romasco, T. Clark, R.G. Polcawich, J.S. Pulskamp, M. Dubey, R.O. Ritchie, C.L. Muhlstein. (2011). "Fatigue-induced grain coarsening in nanocrystalline platinum films." *Acta Materialia* **59**(3): 1141-1149.

A.L. Romasco-Tremper, S.E. Mohny, K.L. Andre, J. Lin, C.L. Muhlstein. (2012). "Softening under Membrane Contact Stress due to Ultra-thin Ru Coatings on Au films." *Materials Science and Engineering A* (submitted).

A.L. Romasco-Tremper, C.L. Muhlstein, S.E. Mohny. (2012). "Reconciling Deformation, Contamination, and Geometry Contributions to the Resistance of Ohmic Contact Switches." *IEEE Transactions on Components, Packaging, and Manufacturing Technology* (submitted).